

The role of molecular chaperones in *Escherichia coli* cells subjected to gold nanoparticles induced stress

Lutendo Michael Mathomu

Student No: 11511156

submitted in fulfilment of the requirements for the degree of
Doctor of Philosophy in the subject of Biochemistry

at

The University of Venda

Promoter: Prof Addmore Shonhai

Co-Promoter: Dr Tawanda Zininga

Submitted on May 2021


Abstract

Colloidal suspensions of gold particles of nanometre (nm) sizes are termed gold nanoparticles (AuNPs). Although stable, AuNPs have been reported to be toxic to *E. coli* cells by collapsing the bacterial cell membranes and promoting protein misfolding. An understanding of biodistribution in drug delivery and the effects AuNPs have on the function and structure of proteins such as heat shock proteins is important. Heat shock proteins facilitate protein folding and are particularly important during cellular stress. At high concentrations, AuNPs are thought to promote protein aggregation. Heat shock proteins are thought to alleviate cell stress induced by AuNPs. This study explored the role of heat shock proteins in conferring cytoprotection to *E. coli* against the effects of AuNPs. Citrate-AuNPs were synthesized and their integrity was validated at 520 nm by ultraviolet-visible-near infrared spectroscopy (UV-Vis-NIR). Crystallinity was confirmed by X-Ray diffraction (XRD), while dynamic light scattering (DLS) estimated the size distribution at ~13 nm. Furthermore, transmission electron microscopy (TEM) and scanning electron microscope (SEM) revealed the spherical shape and crystal lattice surface morphology of citrate-AuNPs respectively. A complementation assay was conducted using cells deficient of DnaK function (*E. coli* Δ *dnaK52*). *E. coli* Δ *dnaK52* was transformed with a recombinant *dnaK* before examining both DnaK deficient and transformed cells using TEM. *E. coli* O157:H7 was exposed to citrate-AuNPs (0 – 50 μ g/ml) and allowed to grow at 37 °C before protein expression was analysed using electrophoresis followed by LC-MS analysis. This led to the identification of highly expressed proteins such as DnaK, GAPDH, ClpX, DnaJ, and GroEL. Subsequent co-affinity assay revealed possible interaction protein partners of DnaK. These were identified as ClpB, HtpG, GroEL, DnaJ, and SurA proteins. Furthermore, circular dichroism and fluorescence spectroscopy established that recombinant DnaK is stable at citrate-AuNPs concentrations less than 10 μ g/ml and the protein was unstable at concentrations beyond 10 μ g/ml citrate-AuNPs. In addition, the ATPase activity of recombinant DnaK increased in the presence of citrate-AuNPs at 2.5 μ g/ml. The ability of DnaK to suppress aggregation of MDH in vitro was abrogated by the presence of >10 μ g/ml citrate-AuNPs. The findings suggest that at low concentrations (<10 μ g/ml) citrate-AuNPs seem to stabilize proteins and similarly at elevated concentrations (>10 μ g/ml), citrate-AuNPs destabilizes protein conformation and function. Altogether the findings suggest that DnaK in cooperation with its network partners is implicated in *E. coli* cytoprotection against citrate-AuNPs toxicity.

Keywords: Gold nanoparticles; cytotoxicity; cell stress; molecular chaperones; DnaK; interaction partners.

Declarations

I, Lutendo Michael Mathomu hereby declare that the thesis for the Doctor of Philosophy in Biochemistry degree at the University of Venda, hereby submitted by me, has not previously been submitted for any degree at this or any other university, and that it is my work in design and execution and that all reference materials contained herein have been duly acknowledged.

Signature (Candidate):  _____

Date: 09/05/2021 _____

Dedication

This work is dedicated to my loving and supportive family, my wife Rirhandzu, my son Maseo and my daughter Asa.

Preface

This thesis is comprised of five chapters. The outlines for each chapter are provided below.

Chapter 1: This is a general introduction encompassing all the background to the suggested broad aim and specific objectives. It also highlights the problem statement and spells out the study hypothesis.

Chapter 2: This chapter reports the synthesis and physical characterization of citrate-AuNPs used in cellular, biochemical and biophysical assays.

Chapter 3: This chapter reports on an investigation of the effects of citrate-AuNPs on *E. coli* cells. It also reports on the exploration of the effect of recombinant DnaK in *E. coli* cells exposed to citrate-AuNPs by assessing the proteomic expression levels. This chapter also explores the possible interaction partners of DnaK under citrate-AuNPs stress.

Chapter 4: This chapter involves the biophysical and functional characterization of recombinant DnaK in the presence of toxic levels of citrate-AuNPs.

Chapter 5: This chapter encompasses the concluding remarks and future perspectives from the whole study.

Acknowledgements

Allow me to extend my sincere gratitude to the promoters of the study, Prof. Addmore Shonhai (University of Venda) and Dr. Tawanda Zininga (Stellenbosch University) for their continuing intellectual guidance and patience. I would also like to express my gratitude to my mentor Professor Gregory Blatch of the University of Notre Dame, Australia for the kindest support and motivation. I am sincerely grateful to Prof Neerish Revaprasadu and his nanotechnology group at the University of Zululand for technical support when most needed. Dr Stanley Makumire (University of Cape Town) for re-introducing me to the laboratory and continuously proofreading my documents without fail, I thank you. To all my lab mates, I thank you for keeping it real and entertaining always. I am extremely grateful to my family for their support and encouragement.

Finally, I would like to extend gratitude to the following institutions for funding this project;

- The Department of Science and Innovation through the University Capacity Development Programme and New generation of academics programme
- The National Research Foundation (NRF) of South Africa for partly funding the project
- The University of Venda Research and Publication Committee (RPC) for partly funding the project.

Table of Contents

Abstract	i
Declarations	ii
Dedication	iii
Preface	iv
Acknowledgements	v
List of figures	xi
CHAPTER 1	1
1. Introduction and Literature Review	1
1.1. Nanotechnology and Nanobiotechnology	1
1.2. Nanoparticles	2
1.2.1. Liquid crystals nanoparticles	3
1.2.2. Nanotubes	4
1.2.3. Liposomes	4
1.2.4. Quantum dots	5
1.2.5. Superparamagnetic nanoparticles	6
1.2.6. Dendrimers	7
1.3. Coating and functionalization of nanoparticles	7
1.4. Gold nanoparticles	9
1.4.1. Gold nanoparticles	9
1.4.2. Synthesis and characterization of gold nanoparticles	9
1.4.3. Toxicity of gold nanoparticles	11
1.4.4. Interaction of bacterial cells with gold nanoparticles	11
1.4.5. Heat shock proteins as molecular chaperones	12
1.5. E. coli heat shock proteins	13
1.5.1. Heat shock protein 40	14
1.5.2. Heat shock protein 60/10	15
1.5.3. Heat shock protein 70	17
1.5.3.1. DnaK chaperone cycle	18
1.5.3.2. Nucleotide exchange factors of Hsp70	19
1.5.2.4. Hsp90 family	19
1.5.2.5. Hsp100 family	20
1.6. Problem Statement, Hypothesis, Aim, and Objectives	21

1.6.2.	Problem Statement.....	21
1.6.3.	Hypothesis.....	22
1.6.4.	Study Aim	22
1.6.5.	Study Objectives	22
CHAPTER 2.....		24
2.	Synthesis and Characterization of Citrate-Capped Gold Nanoparticles.....	24
2.1.	INTRODUCTION.....	24
2.1.1.	Specific Objectives	25
2.2.	EXPERIMENTAL PROCEDURES	25
2.2.1.	Materials.....	25
2.2.2.	Synthesis of spherical gold nanoparticles	25
2.3.	RESULTS.....	29
2.3.1.	Sodium citrate salt reduces Au ³⁺ ions to Au ⁰ in the synthesis of gold nanoparticles	29
2.3.2.	Fourier Transform Infrared Spectroscopy (FTIR) detects possible dangling functional groups between citrate species and AuNPs.....	30
2.3.3.	XRD pattern confirms highly oriented crystallinity rate of citrate-AuNPs.....	32
2.3.4.	Scanning electron microscopy (SEM) and transmission electron microscopy (TEM) based determination of the morphology and size of the synthesized citrate-AuNPs	33
2.3.5.	Use of particle size analyzer zetasizer to determine the size and surface charge of synthesized citrate-AuNPs.....	34
2.4.	DISCUSSION.....	36
CHAPTER 3.....		39
3.1.	INTRODUCTION.....	39
3.1.1.	Specific Objectives	40
3.2.	EXPERIMENTAL PROCEDURES	41
3.2.1.	Materials.....	41
3.2.2.	Expression and evaluation of E. coli O157:H7 proteomic constituents in the presence of citrate-AuNPs cell stressors.....	41
3.2.3.	Identification of the interaction partners of DnaK associated with citrate-AuNPs induced cell stress	42
3.2.5.	Determination of soluble proteomic constituents of E. coli ΔdnaK52 exposed to citrate-AuNPs stress inducers	43
3.2.6.	Assessment of the role of DnaK in E. coli cells exposed to citrate-AuNPs	44
3.2.7.	Identification of the interaction partners of E. coli DnaK.....	45
3.3.	RESULTS.....	47

3.3.1.	Expression of proteomic constituents of E. coli O157:H7 subjected to citrate-AuNPs induced stress	47
3.3.2.	Assessment of the bacterial/AuNPs interaction	51
3.3.3.	The DnaK interactome identified in silver-stained SDS-PAGE.....	52
3.4.	DISCUSSION	57
CHAPTER 4.....		60
4.	Biophysical and Biochemical Characterization of Recombinant DnaK subjected to citrate-AuNPs.....	60
4.1.	INTRODUCTION.....	60
4.1.1.	Specific Objectives	61
4.2.	EXPERIMENTAL PROCEDURES	61
4.2.1.	Materials.....	61
4.2.2.	Expression and purification of DnaK and DnaJ from E. coli XL1 Blue strain...	62
4.2.3.	Investigation of the effect of citrate-AuNPs on ATPase activity of recombinant DnaK aided by co-chaperone DnaJ in vitro	62
4.2.4.	Investigation of the effect of citrate-AuNPs on the ability of DnaK aided by co-chaperone DnaJ to suppress aggregation of MDH enzyme in vitro	63
4.2.5.	Investigation of the effect of citrate-AuNPs on the secondary and tertiary structure of DnaK by circular dichroism spectroscopy and fluorescence spectroscopy	63
4.3.	RESULTS.....	65
4.3.1.	Citrate-AuNPs regulate the ATPase activity of recombinant DnaK aided by its co-chaperone DnaJ in vitro.....	65
4.3.2.	Citrate-AuNPs influences the ability of DnaK and co-chaperone DnaJ to suppress aggregation of MDH enzyme in vitro.....	68
4.3.3.	Citrate-AuNPs do not affect the secondary and tertiary structure of DnaK	70
4.4.	DISCUSSION	75
CHAPTER 5.....		77
5.	CONCLUDING REMARKS AND FUTURE PERSPECTIVES.....	77
5.1.	CONCLUDING REMARKS	77
5.2.	FUTURE PERSPECTIVE.....	79
6.	REFERENCE LIST.....	80
7.	APPENDICES	95
7.1.	APPENDICES A.....	95
7.2.	APPENDICES B.....	96
7.3.	APPENDICES C.....	96
7.4.	APPENDICES D.....	104

List of symbols and abbreviations

Å	Angstrom	α	Alpha
M	Molar	β	Beta
λ	Wavelength	θ	Theta
Δ	Change	mg	milligram
N		μ	Micro-
kV	Kilovolts	mins	Minutes
UV	Ultraviolet radiation	Vis	Visible light radiation
NPs	Nanoparticles	NBD	Nucleotide Binding Domain
NEF	Nucleotide Exchange Factor	SPR	Surface Plasmon Resonance
SBD	Substrate Binding Domain	SurA	Survival protein A
CNTs	Carbon nanotubes	CRR	Cysteine Rich Region
Cys	Cysteine	Clp	Caseinolytic protease
Cbp	Curved DNA binding protein A	Chi	Chitosan
CD	Circular Dichroism	Cit	Citrate
AuNPs	Gold nanoparticles	AuNC	Gold nanocubes
AuNR	Gold nanorods	AuNO	Gold nanooctahedron
AuNS	Gold Nanosphere	AuDA	Malonic Gold nanoparticle
PPI	Protein Interaction	PDB	Protein Database
pI	Isoelectric point	PCP	Protein-correlation-profiling
ATP	Adenosine Triphosphate	ADP	Adenosine diphosphate
OD	Optical density	BSA	Bovine Albumin Serum
DnaJ	40 kDa heat shock protein	DLS	Dynamic light scattering
HRP	Horseradish peroxidase	Hsl	Hormone-sensitive lipase
HAuCl₄	Chlorauric acid	Htp	High-temperature protein
Hsp	Heat shock protein	QDs	Quantum dots
DnaK	70 kDa heat shock protein	DTT	Dithiothreitol
RMSD	Root-mean-square deviation	GroEL/ES	Chaperonins
Grp	Bacterial NEF	GAPDH	Glyceraldehyde 3-phosphate dehydrogenase
RpoH	RNA polymerase	NIR	Near-infrared
MDH	Malate dehydrogenase	ATR-FTIR	Attenuated total reflectance-FTIR
FDR	False discovery rate	XRD	X-Ray diffraction
LFQ	Label-free quantification	SILAC	Stable isotope labeling of amino acids in cell culture

TSBYE	Tryptone soy yeast extract	IPTG	Isopropyl β -d-1-thiogalactopyranoside
LTQ	Linear Trap Quadrupole	LC-MS	Liquid chromatography–mass spectrometry
TEM	Transmission electron microscopy	SEM	Scanning electron microscopy
TBS	Tris base saline	TYR	Tyrosine
TRP	Tryptophan	2YT	Double yeast tryptone media
NTS	Normalized total spectrum		

List of figures

Figure 1.1. The structure of liquid crystals is highly ordered with surfactant molecules in the hydrophilic region and the tails immersed in the hydrophobic region	3
Figure 1.2. Schematic indication of carbon nanotubes (CNT) forming multiple fullerenes molecular structures	4
Figure 1.3. Schematic representation of a laminar liposome with drug trapped in a central hydrophobic region with DNA material covered within a hydrophilic layer	5
Figure 1.4. Changes in optical properties of nanocrystals quantum dots (QDs) are caused by an increase or decrease in the size of QDs (Adapted from Samadi-Maybodi, 2021).	6
Figure 1.8. Schematic illustration of the binding of hydroxyl and free carboxylate groups of citrate on the Au surface.	11
Figure 1.10.	15
Figure 1.11. A representation of the structure of the GroEL. (A) A chain from the double ring indicating apical domain (SBD) in blue, intermediate domain (Hinge region) in magenta and equatorial domain (NBD) in yellow. (B) A double ring functional complex of GroEL indicating a hollow opening. Adapted from Kelley et al (2015).	16
Figure 1.12. A representation of the structural motifs of E. coli DnaK.	17
Figure 1.13. A representative model for the functional cycle of DnaK.	18
Figure 2.1. Schematic representation of the general synthetic procedure of citrate-capped gold nanoparticles.	26
Figure 2.2. The synthesis of citrate-coated gold nanoparticles (citrate-AuNPs) was validated.	30
Figure 2.3. ATR-FTIR spectrum of synthesized citrate-AuNPs indicated different functional groups.	31
Figure 2.4. XRD diffractogram determined the basic crystalline nature of citrate-AuNPs.	32
Figure 2.5. SEM image showing surface features of citrate-AuNPs including particle agglomeration due to concentration and drying.	33
Figure 2.6. TEM image showing features of citrate-AuNPs dispersed in ultrapure water before analysis.	34
Figure 2.7. Size distribution analysis of the citrate-AuNPs dispersed in ultra-pure water was performed between the minimum and maximum concentration recommended for samples	35
Figure 2.8. Zeta potential analysis of citrate capped AuNPs dispersed in ultra-pure water.	36
Figure 3.1. E. coli O157:H7 growth curve in the presence of citrate-AuNPs.	48
Figure 3.2. Protein expression profiles of E. coli O157:H7 cells subjected to varying concentrations of citrate-AuNPs on 10 % SDS PAGE indicated non-toxicity and stable proteome expression.	49
Figure 3.3. TEM images of E. coli Δ dnaK52 cells subjected to lower and higher-order citrate-AuNPs concentrations.	52
Figure 3.4. The interactome of DnaK was recovered under various concentrations of citrate-AuNPs.	54
Figure 4.1 Citrate-AuNPs regulate ATPase activity of recombinant DnaK.	66
Figure 4.2 The combination with DnaJ and 2.5 μ g/ml citrate	68
Figure 4.3. Citrate-AuNPs increases the efficiency of DnaK and DnaJ chaperone functional association in vitro.	69

Figure 4.4. Lower order citrate-AuNPs enhances the stability of the secondary structure of DnaK at higher temperatures than normal functional levels.----- 71

Figure 4.5. Citrate-AuNPs do not perturb the secondary structure of DnaK.----- 72

Figure 4.6. Citrate-AuNPs have no effect on the tertiary structure of DnaK. The stability of DnaK in the presence of citrate-AuNPs was not affected either at lower order or higher order of AuNPs concentration.----- 74

List of output(s)

L.M., Mathomu, T., Zininga, A., Shonhai. Investigation of the effects of citrate-gold nanoparticles on the structural features of *E. coli* DnaK chaperone system. Oral Presentation of the 10th Anniversary of the Biotechnology and Biochemistry Research Unit, Rhodes University, Makhanda, 2018

CHAPTER 1

1. Introduction and Literature Review

1.1. Nanotechnology and Nanobiotechnology

Nanotechnology is coined from a combination of two words, the Greek numerical prefix “*nano*” which refers to a billionth, and the term “*technology*” referring to the applied science as a craft. It is generally considered to be a study of materials at a size below 0.1 μm (Ahmed *et al.*, 2016). Multi-disciplinary fields emerging from nanotechnology include material science and nanobiotechnology. Nanobiotechnology is a field converged from the two existing but distant spheres of engineering and molecular biology, simply from nanotechnology and biology. The potential of nanoparticles (NPs) to solve biological problems contributed to the emergence of the field of nanobiotechnology (Rodríguez-Limas *et al.*, 2013). Developments in nanobiotechnology have seen an emergence of useful applications in reproductive healthcare, drug delivery, imaging, diagnosis, and pollution remediation. Nanobiotechnology and its applications have the potential to improve the quality of life in that some nanoparticles (NPs) are currently used in cosmetics (Jha *et al.*, 2014), as antimicrobial agents in water filtration (Planchon *et al.*, 2017), as semiconductors in electronics (Ceballos-Alcantarilla *et al.*, 2017) and catalysis (Amendola *et al.*, 2020). Although there are toxicity concerns to humans and animals from certain NPs, some have the potential to provide opportunities for the development of new materials towards more reliable and more sensitive analytical and medical systems (Umamaheswari *et al.*, 2018; Vale *et al.*, 2019).

It is important to understand the interaction and impact of nano-scaled materials with biological entities to make up for the benefits and limitations (Pajerski, *et al.*, 2019). Some nanomaterials may be considered safe in “confinement” i.e when not exposed or reacting with entities in the biological realm. However, upon exposure to humans and animals by inhalation, oral ingestion, or dermal contact the same particles may cause cytotoxicity (Yang *et al.*, 2017; Arafa *et al.*, 2020). Several studies were undertaken to establish the impact of nanomaterials on biological entities including DNA and proteins (Rim *et al.*, 2013; Li *et al.*, 2017). Detrimental effects of AuNPs on

biological entities include cell membrane damage caused by NPs to biological materials (Makumire *et al.*, 2015). Some NPs are toxic while others are not. Hence NPs now attract attention in disease diagnosis and other medical fields such as drug discovery and therapy.

1.2. Nanoparticles

NPs are materials at the nanoscale. Due to their small size, NPs are classified together with nanometer (nm) engineered particles and not with the by-product particles of processes such as welding fumes (Li *et al.*, 2018). NPs possess a large surface area to volume ratio which makes them highly chemically reactive. Due to their small size, NPs can penetrate human and animal cells via cellular junctions and channels (Wang *et al.*, 2017). They are also able to enter microbial cells (Luo *et al.*, 2016). Their size, chemical composition, surface structure, solubility, shape, and aggregation properties determine the physicochemical properties of NPs (Arora *et al.*, 2012; Li *et al.*, 2018). NPs such as zinc oxide and silver nanoparticles have also been found to possess antimicrobial properties against certain bacterial strains (Adur *et al.*, 2018) and while being reportedly inert against other strains (Chakraborty and Biswas, 2020).

The increasing utilization of NPs in electronic and medical manufacturing demands an assessment of the risks associated with human exposure to the NPs particularly cytotoxicity (Cui *et al.*, 2012; Arafa *et al.*, 2020) and genotoxicity (Rim *et al.*, 2013; Makumire *et al.*, 2014). Cytotoxicity and genotoxicity of specific NPs depend on factors such as concentration, dispersion, and surface functionalization (Cui *et al.*, 2012; Gagner *et al.*, 2012; Rim *et al.*, 2013). Apart from these factors, NPs could still release metallic ions into cells to cause notable physiological damage (Rim *et al.*, 2013; Bajaj *et al.*, 2018).

Classification of nanomaterials is based on the Hall–Petch relation (Naik *et al.*, 2019). Hall-Petch relation describes the dependence of the modifying stress on the grain size in a polycrystalline material of the nanoparticle (Andrievski and Glezer, 2009). Glezer (2011) argued that nanomaterials are being classified incorrectly due to the extended anomalies detected in any class of nanomaterial in comparison to other nanomaterials.

In a bid to eliminate the contradictions, a general structural classification of types of nanomaterials was proposed based on the method of formation, shape, and size. Examples include liquid crystals, dendrimers, carbon nanotubes and quantum dots, magnetic and liposomes amongst others.

1.2.1. Liquid crystals nanoparticles

Liquid crystals are materials that are highly ordered with the propensity to self-assemble (Fig. 1.1; Fang *et al.*, 2014). Classification of liquid crystals is based on their surface plasmon resonance (SPR) (Umamaheswari *et al.*, 2018). The other property is a range of colors from brown, orange, red, and purple in an aqueous solution which makes it easy to distinguish liquid crystal. An absorption peak is generally observed when the nanomaterial agglomerates and grows from 1 – 100 nm or beyond. This could also be attributed to the difference in nanomaterial sizes (Priyadarshini and Pradhan 2017). Liquid crystalline NPs have recently been the easiest to synthesize and most common to manipulate and use (Umamaheswari *et al.*, 2018; Muniba *et al.*, 2020). Several pharmaceuticals and cosmetics are made from liquid organic crystalline materials which are designed to mimic naturally occurring molecules such as proteins and lipids (Fang *et al.*, 2014). Liquid crystalline nano-materials including gold nanoparticles are regarded as a safe and specific vehicle of drug delivery. These are the types of nanoparticles known to target an area of the body where tissues are inflamed and are capable of detecting tumors (Ayala-Orozco *et al.*, 2014).

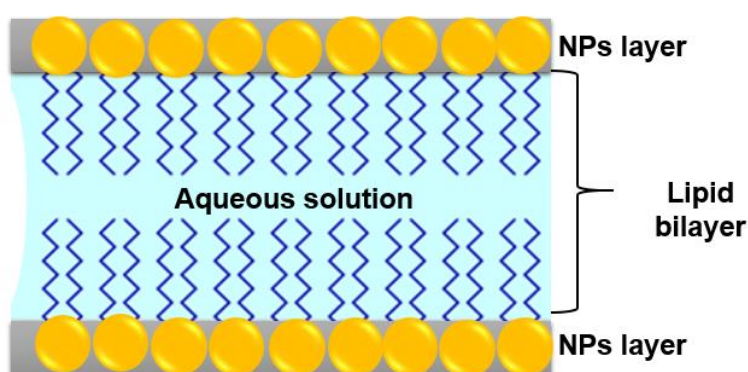


Figure 1.1. The structure of liquid crystals is highly ordered with surfactant molecules in the hydrophilic region and the tails immersed in the hydrophobic region (Adapted from Fang *et al.*, 2014).

1.2.2. Nanotubes

Nanotubes are a form of tubular fullerenes made exclusively of a specific element (Fig. 1.2). Fullerenes are molecular structures like that of graphite, which is composed of stacked sheets of graphene linked by hexagonal or pentagonal rings (Martin, 2019). Gold nano-rings make gold nanotubes by simple staking of rings while silver nanotubes emanate from the coating of longitudinal material such as silica (Park *et al.*, 2004). The most novel of nanotubes is carbon nanotubes (CNTs) and due to their novel properties, they have been studied and applied in various technological fields. Material sciences and electronics have and continue to study, fabricate and apply CNTs (Wang *et al.*, 2014; Alim *et al.*, 2018).

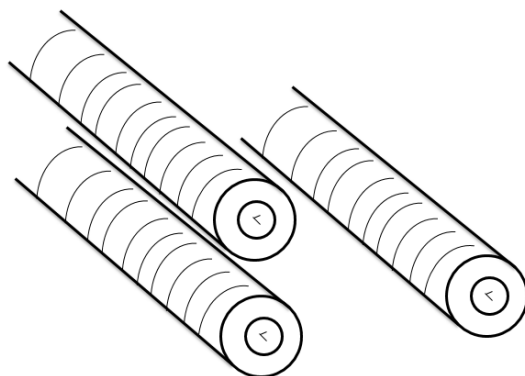


Figure 1.2. Schematic indication of carbon nanotubes (CNT) forming multiple fullerenes molecular structures (Adapted from Alim *et al.*, 2018).

1.2.3. Liposomes

Liposomes are supramolecular assemblies of lipid vesicles polymer nanocontainers (Fig. 1.3) used largely as a medium for the transportation of drugs in biological body systems (Blom *et al.*, 2017). In general, liposomes had been reported to be useful in biophysics and biochemistry as an efficient model system in understanding the properties of cell membrane and channels; understanding protein function, trafficking and signaling, and understanding drug and gene delivery (Maleki *et al.*, 2016, Blom *et al.*, 2017). Liposomes degrade within cells once delivery has been successful, a property that makes them compatible with biological-based applications (Ngweniform *et al.*, 2009; Yoshizaki *et al.*, 2017; Blom *et al.*, 2017). Although liposomes were the first synthesized nanoparticles aimed at drug delivery, they were met with a major

limitation due to the tendency to agglomerate in aqueous environments, releasing contents earlier than targeted. A search for a replacement led to a “green synthesis”, a much safer methodology yielding liposome-stabilized AuNPs which involved a simple, rapid, and controlled reaction (Singh *et al.*, 2018). The method involved ascorbic acid as a reducing agent together with a mixture of liposome-based vesicles and H_{AuCl}₄ (Genc *et al.*, 2011).

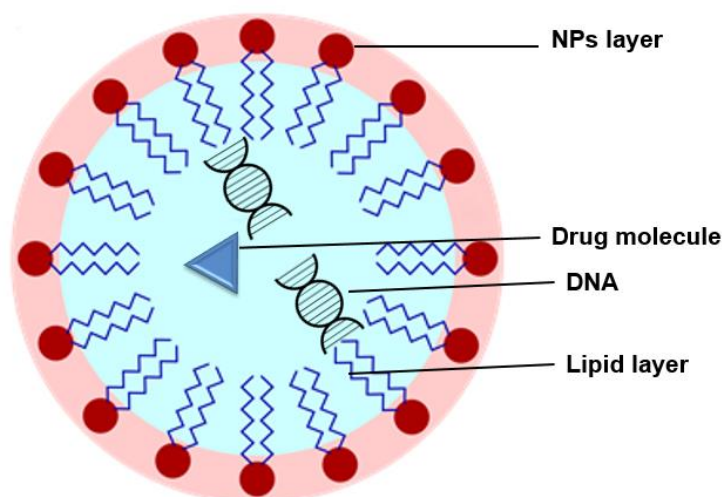


Figure 1.3. Schematic representation of a lamellar liposome with drug trapped in a central hydrophobic region and DNA material embedded within a hydrophilic layer to reduce contact with the drug molecule. Trapped materials are easily transferred to parts of the human body. (Adapted from Blom *et al.*, 2017).

1.2.4. Quantum dots

Quantum dots (QDs) are super small semiconductor nanoparticles with a size range from 1 – 10 nm. QDs unique properties include greater photostability, brightness, size-dependent optical properties, and high extinction coefficient (Wang *et al.*, 2017). QDs can emit light in all colors of the spectrum depending on their size. In their size analysis, the size of quantum dots decreases as the spectrum gets closer to the blue-end (~250 nm) and increases as it proceeds to the red end (Fig. 1.4; Adapted from Samadi-Maybodi, 2021). QDs have unique properties such that they can even be tuned beyond visible light, infra-red, or the ultra-violet spectrum (Appendix A-1) and could confine conduction band electrons, valence band holes, or excitons in all three spatial directions (Murray *et al.*, 2000). QDs are of great value in biotechnology since traditional dyes are limited with properties such as superior photoluminescence important in imaging and biosensing (Park *et al.*, 2019; Xue *et al.*, 2020).

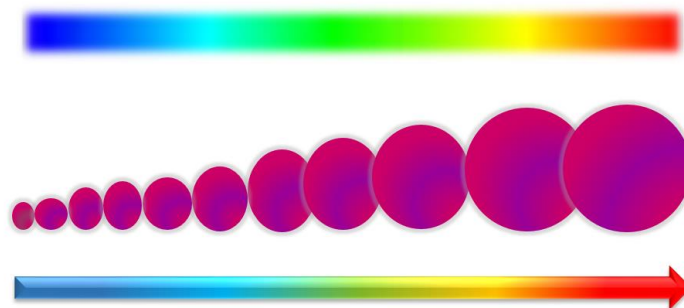


Figure 1.4. Changes in optical properties of nanocrystals quantum dots (QDs) are caused by an increase or decrease in the size of QDs (Adapted from Samadi-Maybodi, 2021).

1.2.5. Superparamagnetic nanoparticles

Superparamagnetic nanoparticles are an important category of nanoparticles with a metal oxide core coated by either inorganic or organic materials (Fig. 1.5; Arora *et al.*, 2012). This category has an important unique property in that their magnetization is induced and as such, they are attracted to a magnetic field without retaining residual magnetism. This property makes them unique and attractive for most applications compared to the rest of the nanoparticles. They have been used in the past in applications such as drug delivery systems and magnetically assisted transfection of cells (Schubert *et al.*, 2019).

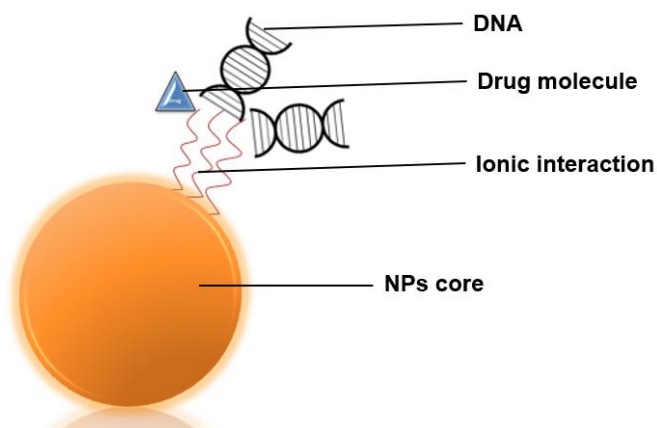


Figure 1.5. Schematic demonstration of potential super magnetic nanoparticles attached to a drug molecule and genetic material through ionic bonds (Adapted from Arora *et al.*, 2012).

1.2.6. Dendrimers

Dendrimers are branched structures with uniform sizes, radial symmetry and assume a circular shape in solution (Fig. 1.6; Nemanashi *et al.*, 2018). Dendrimers are built layer-by-layer from core to periphery by repetitive covalent bond-forming reactions. The density of the dendrimers increased for every layer formed in each step because of the geometric growth at each branching point (Chahal *et al.*, 2016). Functionalization of dendrimers is achieved by choosing the final reagent to enable the attachment of molecules with different active surface groups (Phillips, 2004). Dendrimers were an invaluable tool in nanomedicine due to an ability to attach to several biological molecules including fluorescent dyes, enzyme identification tags, and other molecules because of the many molecular “primers” present on their branched surfaces (Chahal *et al.*, 2016).

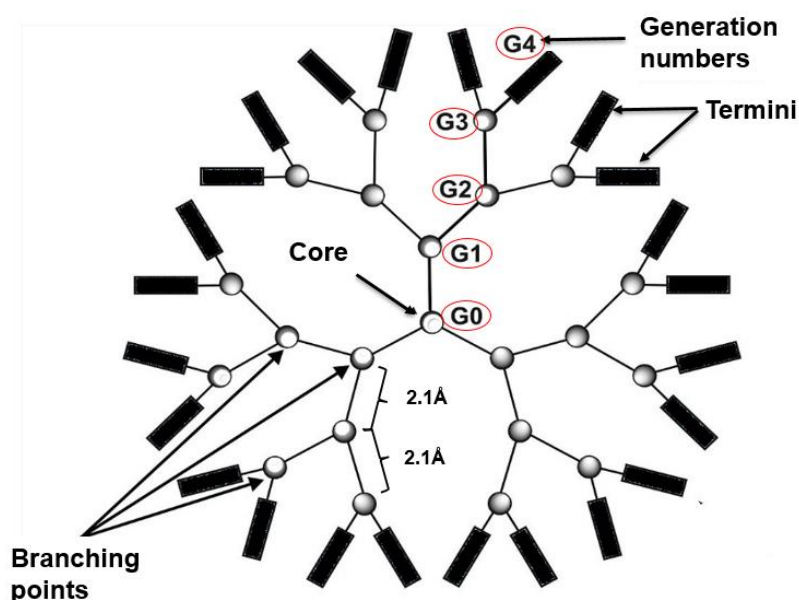


Figure 1.6. Schematic representation of the formation of five generations branched dendrimer. The initial or first-generation is a core (G-0) of the formed cluster to fifth-generation (G-4) termini which carries functionality on the surface of the dendrimer. Distances between generations are predetermined in the synthesis of the dendrimer (Adapted from Nemanashi *et al.*, 2018).

1.3. Coating and functionalization of nanoparticles

NPs are comprised of a core material and a surface modifier. The surface modifier also referred to as a “capping” or “coating” agent transforms the physicochemical

properties of the core or naked NP (De Jong, 2008). The surface properties of NPs play a role in conferring cytotoxicity or cytoprotection. NPs surfaces can be coated with different materials (Table 1.1). Surface coating of NPs and functional groups (Fig. 1.7) play an important role in determining the characteristics of the NP-protein interface. The more capping agent (also a reducing salt) used to coat the NP core, the smaller the NPs synthesized. This phenomenon in gold nanoparticle synthesis was first discovered in a reducing agent gold nanoparticles synthesis method by Turkevich in 1957 which was later refined by Frens in the 1970s (Zabetakis *et al.*, 2012).

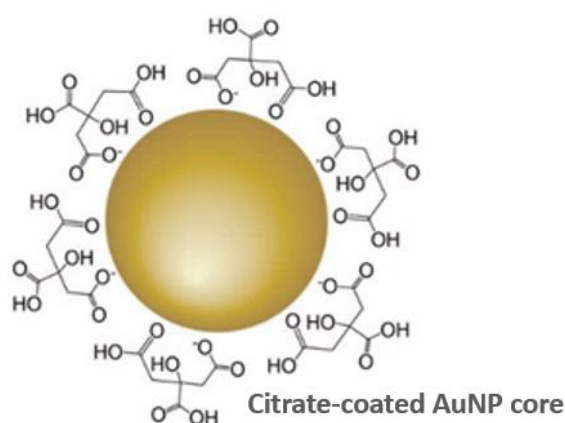


Figure 1.7. Schematic representation of NP core coated with citrate ions (Adapted from Park and Shumaker-Parry, 2014; Lopes-Rodriguez *et al.*, 2020).

Table 1.1. Different surface coatings of nanoparticles

	Surface Coatings	Acronym	Functionalization/ Application	Reference Source
1	Polyvinyl Pyrrolidone (PVP)	PVP	Enhances van der Waal attractions	Park and Shumaker-Parry, 2014
2	Cysteine	Cys	Biosensing and biolabeling	Priyam <i>et al.</i> , 2004; Luthuli <i>et al.</i> , 2013
3	Chitosan	Chi	Enhances interactions with serum components	Regiel-Futyra <i>et al.</i> , 2015; Boyles <i>et al.</i> , 2015
4	Bovine serum albumin (BSA)	BSA	Enhances hydrophobic contacts	Klein <i>et al.</i> , 2016
5	Citrate	Cit	Particle stabilization	Lopes-Rodriguez <i>et al.</i> , 2020

1.4. Gold nanoparticles

1.4.1. Gold nanoparticles

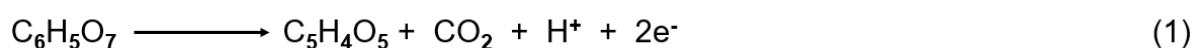
There were no modern means of analyzing the size of AuNPs such as transmission electron microscopy (TEM) in 1857 when gold nanoparticles were first discovered (Link and El-Sayed, 2000). Hence, gold nanoparticles (AuNPs) were recognized by the ruby red color of colloidal gold which emanates from either nucleation or agglomeration of gold atoms. AuNPs are in the range ≤ 100 nm and display unique optical, electrical and molecular recognition properties. The properties and applications of AuNPs depend upon their shape and size (Gobin *et al.*, 2007; Cui *et al.*, 2012). The synthesis of AuNPs of different shapes such as nanospheres (AuNS) (Martin, 2019) and other geometries such as rod-shaped referred to as nanorods (AuNR) (Gagner *et al.*, 2012), nanocubes (AuNC) (Muniba *et al.*, 2018) and nanooctahedra (AuNO) (Lopes-Rodriguez *et al.*, 2020) has since been reported. In the visible region, AuNPs possess a high extinction co-efficient making it an ideal color reporting agent for signaling molecular recognition events such as confirming interaction with proteins (Espinosa *et al.*, 2016). The color of AuNPs depends on their sizes (Lopes-Rodriguez *et al.*, 2020). The absorption spectrum of the ruby red citrate-AuNPs was reported at 519 nm peak from the absorption analysis of citrate-AuNPs which is known to range between 510 – 530 nm (Makumire *et al.*, 2015).

1.4.2. Synthesis and characterization of gold nanoparticles

Reducing gold salts with a capping and stabilizing agent has been the basis of the synthesis of AuNPs. Gold salts such as chloroauric acid are commonly used (Makumire *et al.*, 2015; Lopes-Rodriguez *et al.*, 2020). Basic methods of synthesis are widely available, they include amongst other methods such as citrate synthesis which uses trisodium citrate as a reducing and capping agent to the core material (Fig. 1.8; Bajaj *et al.*, 2020). Modifications to the surface of the AuNPs include varying factors such as temperature and salt concentration which then result in AuNPs of different shapes and sizes. The combination of high temperature and citrate salt concentration results in a narrow range of diameters of the particles largely by limiting the growth of nanoparticles during the heating in synthesis (Liu *et al.*, 2020). Synthesis of citrate-

AuNPs is a multiple-step process that begins with the oxidation of citrate yielding dicarboxy acetone before reduction of chloroauric acid. Chemical reaction steps that lead to the formation of citrate-AuNPs from tri-sodium citrate and chloroauric acid may occur in series and parallel (Reactions 1 - 6). The initial oxidation of citrate yielding dicarboxy acetone may play an important role since dicarboxy acetone is further converted into acetone at high temperatures in side reactions, and acetone further reduces auric salt. Reaction 4 indicates the overall stoichiometry of the reduction reaction. The stoichiometric ratio of citrate to gold required for complete conversion of auric chloride should be higher than 1.5 (Fig. 1.8; Park and Shumaker-Parry, 2014). Although further oxidation in side reactions may result in nucleation, further formation of gold particles with hanging citrate ions is expected (Fig. 1.8; Bajaj *et al.*, 2020).

(A) oxidation of citrate yielding dicarboxy acetone:



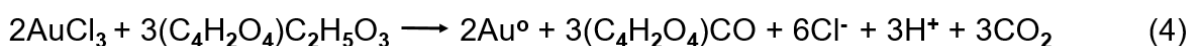
(B) Reduction of auric salt to aurous salt in solution:



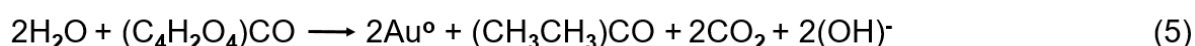
(C) Disproportionation of aurous species to gold atoms and nucleation:



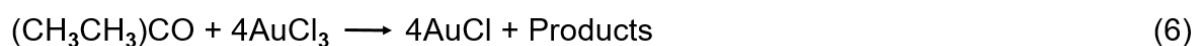
(D) Growth by disproportionation on the particle surface and coagulation:



(E) Further oxidation resulting in dicarboxy acetone:



(F) Further nucleation and product formation



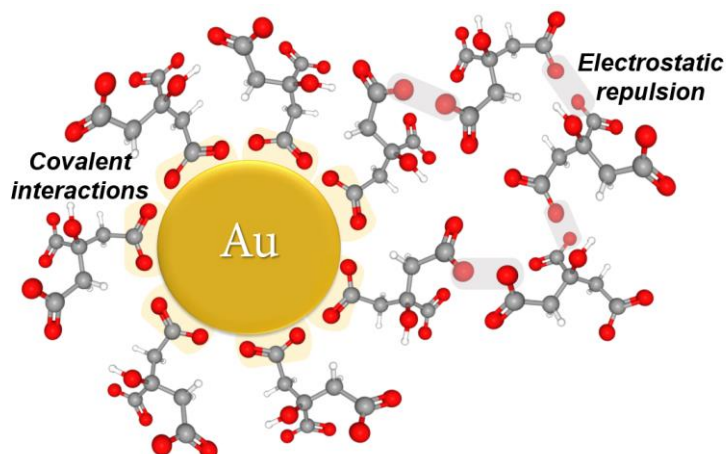


Figure 1.8. Schematic illustration of the binding of hydroxyl and free carboxylate groups of citrate on the Au surface. Hanging citrate ions could have an impact on the binding of biological and chemical entities on the citrate-AuNPs. Orange: Representative of the gold surface, Red: Oxygen, Grey: Carbon, Clear: Hydrogen (Adapted from Park and Shumaker-Parry, 2014; Bajaj *et al.*, 2020).

1.4.3. Toxicity of gold nanoparticles

There have been reports of administration of NPs into animals and humans either orally or intravenously (Cheng, 2018). Regardless of the utility value of such administered NPs, there are serious concerns about the effect of NPs during biodistribution and circulation in the blood stream, their pharmacokinetics, and excretion from the cell or organism. The major concern remains the possibility of toxicity to the organism at the sub-cellular level (Klapper *et al.*, 2014) to which the NPs administered are conjugated. There is consistency in the study of Makumire *et al* (2015) and another by Chatterjee *et al* (2011) which respectively reported cell damage and elongation to *E. coli* cells. In addition to the coating agent, NPs surface charge plays an important role during uptake by cells (Pajerski, *et al.*, 2019). Positively charged NPs gain more affinity towards the negatively charged residues of the biological material (Freese *et al.*, 2012). At a cellular level, membrane damage, cytoplasmic disruption, filamentation, and DNA damage are amongst some of the defects accounted for by the presence of NPs (Makumire *et al.*, 2015).

1.4.4. Interaction of bacterial cells with gold nanoparticles

Size and surface chemistry of NPs are the two factors regulating bacteria-NPs interaction, while surface features of the cell membrane equally dominate the bacteria-

NPs interactions (Pajerski, *et al.*, 2019). Lipopolysaccharides dominate the *E. coli* cell surface and are likely to determine the initial physical interaction between *E. coli* cells and the capping material of AuNPs (Pajerski, *et al.*, 2019). Zinc peroxide, titanium dioxide (Raliyah and Tarafdar, 2013; Makumire *et al.*, 2014), citrate-AuNPs (Luthuli *et al.*, 2013; Makumire *et al.*, 2015), iron oxide (Chatterjee *et al.*, 2011; Darwish *et al.*, 2015) and silver NPs (Ahmed *et al.*, 2016) are examples of NPs which have been observed to impact on *E. coli* growth and proteomic function through membrane disruption in response to stress and protein aggregation (Raliyah and Tarafdar, 2013; Makumire *et al.*, 2014; 2015). *E. coli* responds by expressing molecular chaperones to adapt and survive. Molecular chaperones are proteins that facilitate the proper folding of other proteins necessary for their proper functioning within cells (Kim *et al.*, 2013, Bukau *et al.*, 2006). Makumire *et al.* (2015) observed that citrate-AuNPs are taken up by *E. coli* cells. In their observation of the interaction of *E. coli* cells and citrate-AuNPs, citrate-AuNPs did not appear to be toxic to *E. coli* cells. However, when citrate-AuNPs interacted with *E. coli* cells deficient of molecular chaperone DnaK (Bukau and Walker, 1990), cell wall damage was observed indicating cytotoxicity to compromised cells (Fig. 1.2). *E. coli* cells have been reported to lack the ability to adsorb citrate ions across their membrane. Therefore, citrate in their monodispersed form have been expelled and excluded from adsorbing to *E. coli* cells (Zhou *et al.*, 2015). However, citrate-AuNPs enter the *E. coli* cytosol in the presence of aggregated forms leading to citrate-AuNPs unpredictable reactivity which then leads to cellular damage and subsequent cell death. Aggregated citrate-AuNPs damage the cell membrane when they forcibly encounter a negatively charged cell wall (Zhou *et al.*, 2015; Makumire *et al.*, 2015).

1.4.5. Heat shock proteins as molecular chaperones

Molecular chaperones are described as molecules or a group of proteins that assist in proteostasis (Fernández *et al.* (2016). Molecular chaperones prevent protein misfolding and aggregation by way of covering hydrophobic surfaces exposed by proteins in their nascent state (Bukau *et al.*, 2006; Hartl and Hayer-Hartl, 2009). Heat shock proteins (Hsps) functioning as molecular chaperones are the key components

responsible for protein folding, assembly, translocation, and degradation under stress conditions and in many normal cellular processes. Hsps play an indispensable role as molecular chaperones in the quality control of proteins against potential invaders (Kityk *et al.*, 2012). *E. coli* cells subjected to a variety of stresses increase the synthesis of heat shock proteins. The response is a universal phenomenon occurring in the entire range from bacterial to human cells. In *E. coli*, heat shock protein synthesis increases following changes in temperature shifts from 25 °C to 42 °C and even higher (Bukau and Walker, 1989).

1.5. *E. coli* heat shock proteins

A group of molecular chaperones referred to as heat shock proteins is expressed when exposed to a variety of stress within the cells and are classified by their degree of homology or molecular masses (Park & Seo, 2015) (Table 4.1).

Table 1.4. Heat shock protein families

Protein Family	Monomer Size/ kDa	Chaperone	Function	References
Hsp100	80 – 100	ClpB	Unfoldases / disaggregase with cleavage activity	Avellaneda <i>et al.</i> , 2020
Hsp90	82 – 96	HtpG	Involved in cell survival and cell signaling pathways	Moran-Luengo <i>et al.</i> , 2018
Hsp70	70	DnaK	ATP dependent folding of nascent peptides	Bukau and Walker, 1989
Hsp60	58- 65	GroEL	ATP dependent assembly of protein complexes to their native state (foldase)	Bukau <i>et al.</i> , 2006
Hsp40	40	DnaJ	Bind and stabilize nascent proteins for refolding (holdase)	Mayer <i>et al.</i> , 2005; Kampinga and Graig, 2010

Table legend: Htp- High-temperature protein; DnaJ- Phage lambda replication protein J; DnaK- Phage lambda replication protein K; ATP- Adenosine triphosphate; Grp- glucose-regulated protein; Hsp- heat-shock protein; GroEL- Large subunit and phage head E grown protein; Clp- Caseinolytic protease.

1.5.1. Heat shock protein 40

E. coli DnaJ, also called Hsp40 or J-proteins have recently been named J-domain containing proteins (JDPs) (Kampinga *et al.*, 2018). JDPs are involved in a diversity of cellular processes as the co-chaperone partners of DnaK (Zzaman *et al.*, 2004) to bind, stabilize non-native proteins while stimulating the hydrolysis of Hsp70-bound ATP in the process of refolding (Kampinga *et al.*, 2018). *E. coli* JDPs can be classified structurally based on the presence of three typical domains: a J-domain with or without a conserved tripeptide of HIS, PRO, and ASP (HPD) motif; the glycine–phenylalanine (GF) rich region and cysteine-rich region or domain (CRR) (Fig. 1.9 A; Njunge *et al.*, 2013). With reference to eukaryotic systems, three types of JDPs are known as recently revised based on the presence and absence of structural features of bacterial DnaJ. Type I and type II or class A and class B JPDs are composed of a J-domain at the N-terminus as in bacterial DnaJ. Type III or class C has the J-domain appearing anywhere in the protein. Type I JPDs possess a glycine/phenylalanine (G/F) region following the J-domain and CRR (Fig. 1.9; Kampinga and Graig, 2010). Type II DnaJ contain the J-domain (with HPD motif) and the GF region but lacks the CRR (Fig. 1.9; Kampinga and Graig, 2010). Type III is composed of the J-domain with the HPD motif but lacks both the G/F rich region and the CRR (Fig. 1.3). Type IV contains the J domain with variable position and lacks the G/F rich region and the CRR (Fig. 1.9; Craig and Marszalek 2017).

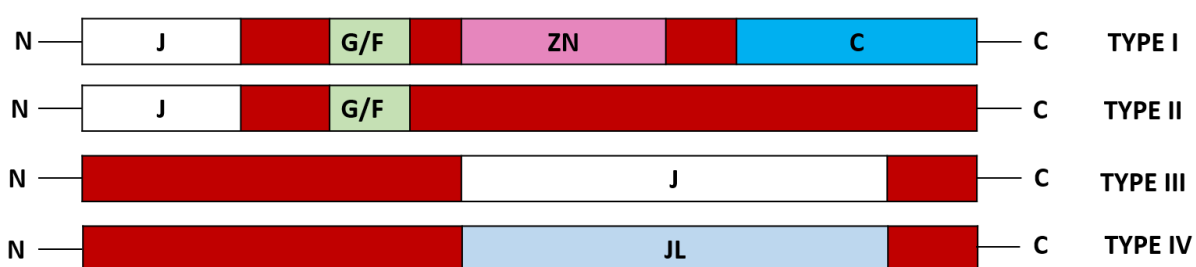


Figure 1. 9: Three types of J-domains. The Hsp40s are grouped into four groups using the classification system proposed by Sahi *et al.*, (2013) and revised by Kampinga *et al.*, (2018). The Hsp40 domains are J-domain, HPD - His, Pro, and Asp motif; GF rich - glycine–phenylalanine-rich region; cysteine-rich domain (CRR) and C-terminal region, Adapted from Kampinga *et al.*, 2018.

The J-domain defines the family of DnaJ/Hsp40 proteins and functions independent of other domains to regulate DnaK ATPase activity. The C-terminus of DnaJ binds

misfolded proteins (Fig. 1.10 A). Although the functions of the G/F region are yet to be fully established, it has been earlier proposed that the G/F region may be important for interactions with DnaK. The Cys-repeats zinc finger motif region also functions in protein folding but without a role in binding stability of polypeptides (Cyr, 2008; Perales-Calvo *et al.*, 2010).

Although limited to a certain extent in these processes, type I and type II JPDs function as a typical molecular chaperone in coordination with other heat shock proteins such as DnaK and GrpE (Hartl and Hayer-Hartl, 2009). The ATP-dependant chaperone activity of DnaK is based on its ability to bind short hydrophobic segments of polypeptides which is regulated by DnaJ (Zzaman *et al.*, 2004). *E. coli* DnaJ promotes the binding of DnaK to multiple sites on the peptide in the presence of ATP (Kampinga *et al.*, 2018).

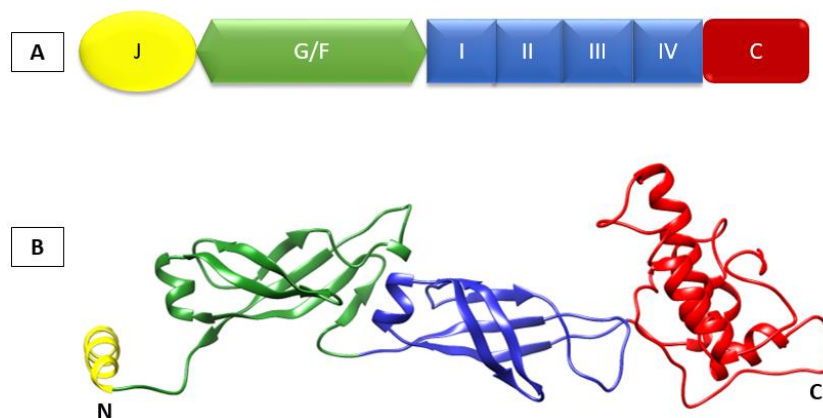


Figure 1.10. A representation of a structural motifs of *E. coli* DnaJ. (A) A representative diagram of the domains of *E. coli* DnaJ (RSCB PDB: 3QOU) where J indicates the J-domain, G/F indicates the Glycine-Phenyl-rich region, and cysteine repeats are indicated by the four zinc-finger-like motifs labeled I, II, III, and IV. **(B)** A 3D ribbon representation of the *E. coli* DnaJ with an indication of the C- and the N- terminus (Adapted from Lo *et al.*, 2003).

1.5.2. Heat shock protein 60/10

Heat shock protein 60 also called GroEL is a double-ring cylinder. GroEL consists of two heptameric rings of ~57 kDa subunits (cis and trans rings) stacked back-to-back each consisting of seven rings (Hartl *et al.*, 2011). GroEL partners with a cofactor

called GroES which is a heptameric ring of about ~10 kDa subunits that cover the ends of the GroEL cylinder like a lid. Together with other chaperones, the chaperonin GroEL and GroES are involved in the mediation of protein folding (Hartl *et al.*, 2011). GroEL has three domains which are an equatorial domain, an apical domain, and an intermediate hinge domain (Fig. 1.10). The equatorial domain which is also nucleotide-binding domain includes the ATP/ADP binding site and forms the inter-subunit connection between the cis and trans rings of GroEL; the apical domain which is a substrate binding domain forms a ring that has a flexible opening to bind the nascent polypeptides. GroEL-GroES chaperonin forms part of the chaperone system in *E. coli* proteome which functions as an isolated nano-cavity for proteostasis (Hartl and Hayer-Hartl, 2009). GroES binds to the apical domain of GroEL to form the GroEL-GroES complex. The intermediate domain forms a flexible hinge to connect the other two domains, the equatorial and apical domains (Bukau *et al.*, 2006).

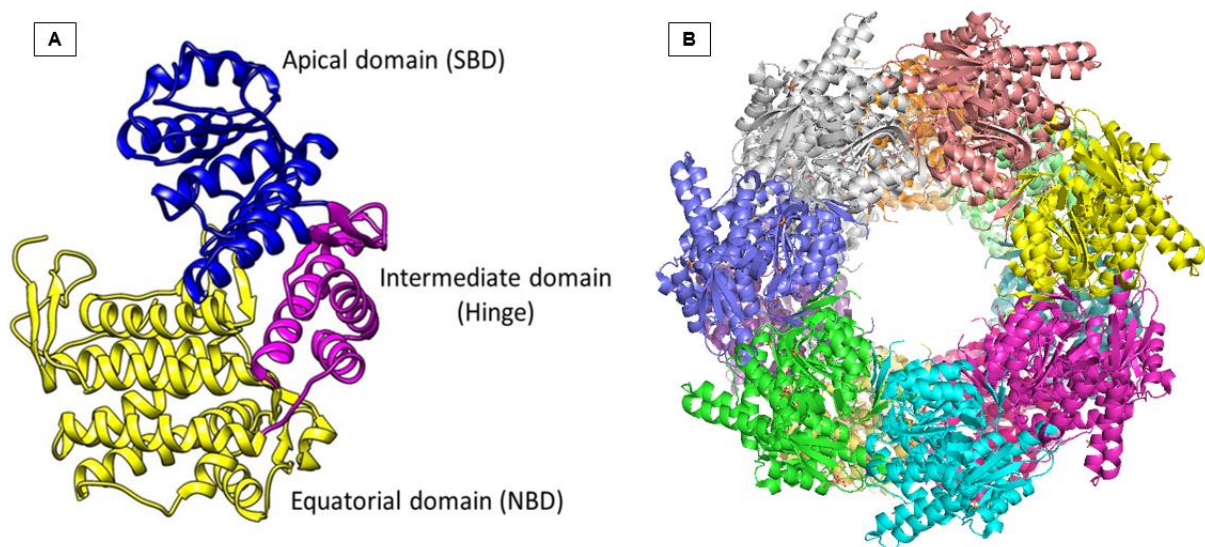


Figure 1.11. A representation of the structure of the GroEL. (A) A chain from the double ring indicating apical domain (SBD) in blue, intermediate domain (Hinge region) in magenta and equatorial domain (NBD) in yellow. (B) A double ring functional complex of GroEL indicating a hollow opening. Adapted from Kelley *et al* (2015).

In *E. coli*, GroEL/ES cooperates with the DnaK/DnaJ/GrpE chaperone system to facilitate the folding of some proteins (Hartl & Hayer-Hartl, 2009). DnaK binds unfolded proteins and delivers them to GroEL-GroES chaperonin for further folding (Calloni *et al.*, 2012). Therefore, the presence of DnaK in the cytosol is important since about 10% of cytosolic proteins which interact with GroEL in *E. coli* proteome are GroEL

dependent for their proper folding (Gomes *et al.*, 2019). There have been reports of the upregulation of GroEL in response to stress in the context of absent or mutated DnaK (Klaper *et al.*, 2014; Makumire *et al.*, 2015). It is, therefore, speculated that GroEL is upregulated to compensate for the lack of DnaK.

1.5.3. Heat shock protein 70

DnaK is a major molecular chaperone in *E. coli* (Kityk *et al.*, 2012). A full-length *E. coli* DnaK structure in an ATP-bound state has been resolved and is often referred to as the basis of the information on DnaK/Hsp70 from other organisms (Kityk *et al.*, 2012). DnaK is composed of an N-terminal 44 kDa Nucleotide-binding domain (NBD) with ATPase activity, substrate binding domain (SBD), and a C-terminal lid (Fig. 1.12). These two domains are connected by a highly conserved 7- residue linker region (Sharma and Masison, 2009). To provide a general explanation of the function of the DnaK domains (Fig. 1.12A), a nucleotide-binding domain (NBD) binds and hydrolyze ATP while a substrate-binding domain (SBD) will bind to extended polypeptides. ATP binding to the NBD promotes polypeptide release and when polypeptide rebinds then ATP hydrolysis is further stimulated (Kityk *et al.*, 2012). DnaK regulates bacterial proteostasis. SBD is the site for peptide substrate binding which is divided into SBD α and SBD β subdomains (Bukau *et al.*, 2006; Bertelsen *et al.*, 2009).

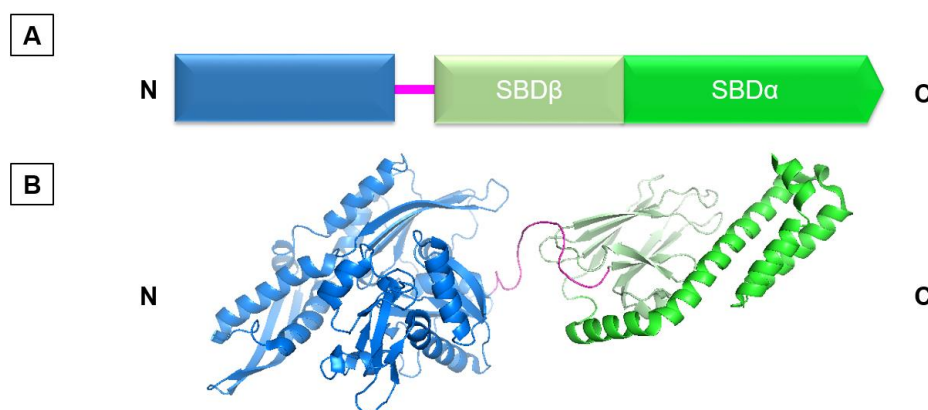


Figure 1.12. A representation of the structural motifs of *E. coli* DnaK. (A) Schematic representation of domain organization of *E. coli* DnaK molecular chaperone. NBD represents the nucleotide-binding domain and SBD represents the substrate-binding domain. The unstructured region indicates the C-terminal domain that recruits the J-domain of DnaJ. Adapted from Banerjee *et al* (2015). (B) Schematic representation of *E. coli* DnaK 3D structure. Blue indicates the NBD binding sites (N – terminal); cyan and green indicate SBD β and SBD α binding sites (C – terminal); Red coiling indicates NBD–SBD linker (Adapted from Sekhar *et al.*, 2018).

The greater part of these proteins (>95 %) diminishes in the presence of ATP which indicated that these proteins interact with DnaK in an ATP-regulated manner. Consistent with the functional cycle of DnaK (Fig. 1.13), the interaction with GrpE is also lost in the presence of ATP. Several proteins in the heat shock family are known to interact with DnaK in the presence of ATP (Section 1.5.2.6) in reversing protein aggregation (Mogk *et al.*, 2018; Kityk *et al.*, 2012).

1.5.3.1. DnaK chaperone cycle

During its functional cycle (Fig. 1.13), DnaK binds to ATP and in this state, the chaperone releases the polypeptide substrate (Kityk *et al.*, 2015). In an ATP-controlled manner, DnaK can bind and release polypeptide substrates, the process which is dependent on allosteric regulation between DnaK NBD and SBD. SBD inhibits the ATPase activity of DnaK by interacting with the NBD through a conserved hydrogen bond network.

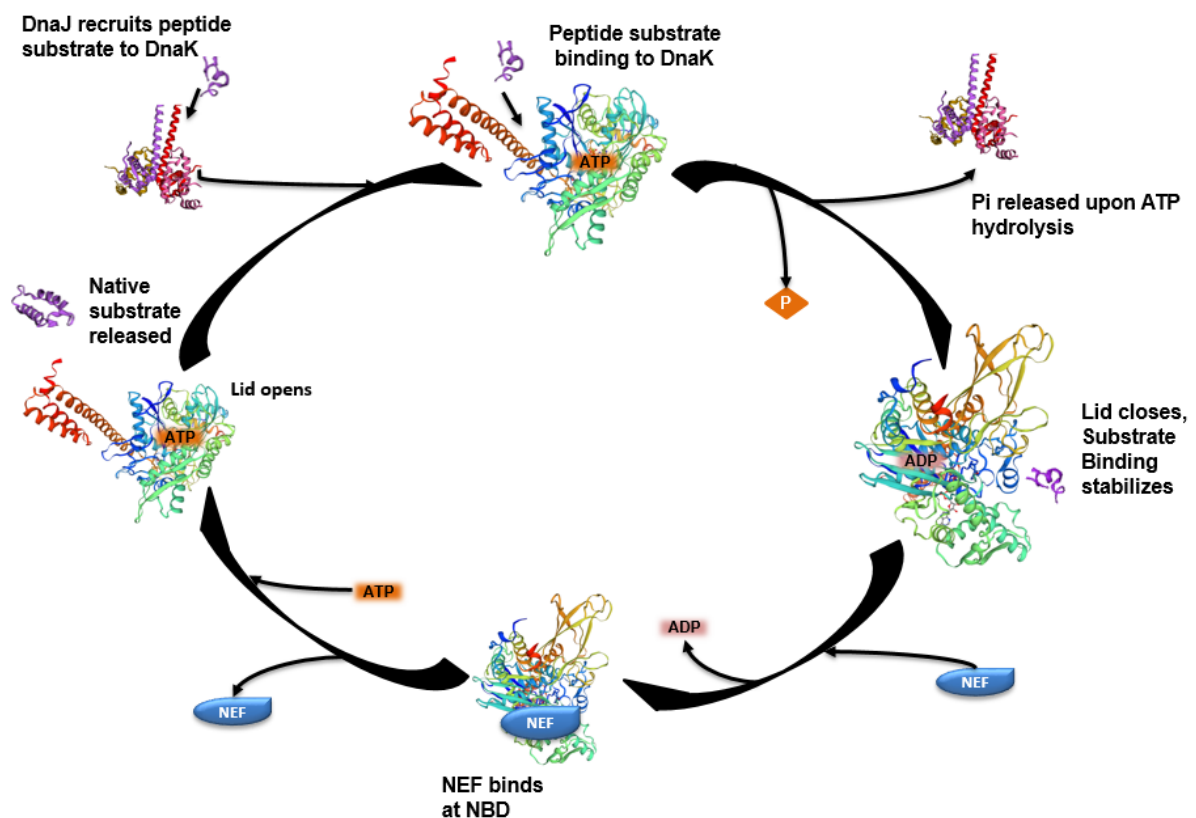


Figure 1.13. A representative model for the functional cycle of DnaK. Recruited peptide substrate is bound to DnaJ and delivered to the SBD of the ATP-bound DnaK. ATP is hydrolyzed and DnaJ is released from the chaperone complex. ADP is bound to DnaK and the lid closes to stabilize the substrate binding within the SBD (Adapted from Chakafana *et al.*, 2019b).

The signal transduction pathway that allows bound substrates to trigger ATP hydrolysis is then defined by the allosteric regulation between SBD and NBD. After DnaK-bound ATP initiates binding of a polypeptide substrate, the rate of dissociation of the DnaK-substrate complex is lowered and the binding stability is increased (Mayer *et al.*, 2005).

DnaK can convert ATP to ADP while either free in solution or bound to DnaJ (section 1.5.1). In the case where DnaJ is in solution with DnaK, DnaK may bind preferentially to sites localized spatially near DnaJ binding sites (Zhuravleva *et al.*, 2012). The introduction of GrpE, a nucleotide exchange factor that regulates the efficient functioning of Hsp70 facilitates the release of ADP from DnaK (Bracher and Verghese, 2015). The next cycle of ATP binding increases significantly the rate of substrate dissociation from DnaK-substrate complexes and allows scanning to continue for more association and binding to continue the cycle (Rosam *et al.*, 2018; Mayer & Gierasch, 2018).

1.5.3.2. Nucleotide exchange factors of Hsp70

NEFs act as substrate release factors to Hsp70 (Rosam *et al.* 2018). Different types of NEFs cooperate with Hsp70, these include; GroP-like gene E (GrpE) in prokaryotes (Packschies *et al.*, 1997) and Hsp110/Grp170 in the eukaryotic cytosol. The BAG-type NEFs in animals are diversified and in contrast to the single GrpE type NEF which is found in bacteria (Bracher and Verghese, 2015). The functional diversity of NEFs is crucial for the specialized function of Hsp70s as they determine different substrate binding time span (Kabani *et al.*, 2008). ATP promotes NEF function (Bracher & Verghese, 2015). Both under heat stress and normal physiological conditions, GrpE is active and enables rapid Hsp70 cycling which is needed for the folding of newly synthesized proteins (Rampelt *et al.*, 2012; Bracher & Verghese, 2015).

1.5.2.4. Hsp90 family

Heat shock protein 90s (Hsp90) includes HtpG in eubacteria. They are a group of ATP-dependent molecular chaperones involved in a variety of cellular processes including cell survival and other cell signaling pathways (Moran-Luengo *et al.*, 2019). Hsp90s

are widespread in eubacteria and eukaryotes. They are the most abundant molecules in the human cell where they constitute about 2 % of the total cell protein mass (Finka *et al.*, 2015). As such, Hsp90 has been identified as a drug target in many cellular disorders and its inhibition could aid the development of anti-viral agents (Lamut *et al.*, 2020). In *S. cerevisiae*, at least 10 % of the proteins will require Hsp90 for proper folding at some stage in proteostasis (Zhao *et al.*, 2005). The Hsp90 family is highly conserved from eubacteria to eukaryotes (Moran-Luengo *et al.*, 2018).

1.5.2.5. Hsp100 family

Hsp100 is also called Clp (caseinolytic protease) in eubacteria. They are categorized into ClpA and ClpB with the number 100, representing their average molecular mass (Deville, 2017). They are a group of molecular chaperones which are primarily involved in the disassembly of the quaternary structure of polypeptide complexes. Hsp100 plays an important role in thermotolerance and the resolubilization of aggregates (Deville, 2017). Hsp100 possesses nucleotide-binding domains (NBD1 and NBD2; AAA+ domains) (Nowicki *et al.*, 2011). Hsp100 is involved in an ATP hydrolysis functional cycle and it is stimulated by substrate binding (Nowicki *et al.*, 2011). The N-terminus serves as the substrate binding domain (Banerjee *et al.*, 2016). Hsp100 functions in cooperation with Hsp70/Hsp40 to support heat-shock survival. Hsp100 uses energy from ATP to extract single polypeptides from aggregated particles (Wang *et al.*, 2019). Within the Hsp100/Hsp70/Hsp40 complex, it is thought that Hsp100 is the first protein to bind to aggregated substrates to pull them out from the aggregated mesh and expose the hydrophobic patches to enable Hsp70 to bind and allow the substrate to fold into its native form (Mogk *et al.*, 2018).

1.5.2.6. Association between DnaK, DnaJ, and GrpE

Hsp70 has a low basal ATPase activity in which one mole of ATP gets hydrolyzed by equimolar Hsp70 in about 25 minutes at 30 °C. The activity is activated by the binding of a substrate at the Hsp70-SBD (Mayer *et al.*, 2000). Hsp70 is thought to be recruited by Hsp40 to sites of protein aggregates which enables Hsp70 to disaggregate proteins (Kampinga *et al.*, 2018). Upon its recruitment to the site or location of aggregates,

Hsp70 subsequently disentangles the aggregated polypeptides ultimately facilitating their refolding (Mogk *et al.*, 2018).

1.6. Problem Statement, Hypothesis, Aim, and Objectives

1.6.2. Problem Statement

Gold nanoparticles (AuNPs) play an important role in nanobiotechnology. However, the interaction of AuNPs with biological materials is not fully understood. Concern in the field of nanobiotechnology is whether NPs impact negatively on biological systems due to their highly active surfaces (Matur *et al.*, 2020). It is of great interest to investigate whether nanoparticles, either acting alone or in conjunction with chaperones themselves, would improve the efficiency of protein folding (Pajerski, *et al.*, 2019). Nanoparticles have been reported to play a role in protein refolding. Gold nanoparticles functionalized with 2-(10-mercaptodecyl) malonic acid played a role in refolding of α -chymotrypsin, lysozyme, and papain. Consequently, *E. coli* molecular chaperones may have a wide range of affinities for AuNPs depending on the size and charge of the AuNPs (De and Rotello, 2008; Sennuga *et al.*, 2012). It is therefore envisaged that molecular chaperones have the potential to interact with AuNPs. Under AuNPs induced stress, *E. coli* cells have been reported to isolate, group, and presumably keep AuNPs from causing cell damage (Makumire *et al.*, 2015). However, mutant *E. coli* cells with deleted DnaK have been reported to slow down ribosome biogenesis which may indicate that DnaK is involved in ribosome assembly which is important for protein synthesis (Maki *et al.*, 2002). Similarly, Makumire *et al.* (2015) reported that *E. coli* with deleted DnaK indicated signs of cell damage under stress, and as such the two reports make DnaK one of the heat shock proteins involved in a diversity of cellular functions. There is a need to further understand the interactions between NPs and proteins. Citrate-AuNPs have been shown to possess chaperone-like properties. It is not fully understood how AuNPs present themselves as molecular chaperones against their possible biotoxicity on the other hand. For these reasons the current study seeks to answer the following questions:

- What other chaperone partners and co-chaperones of DnaK could be expressed as a result of citrate-AuNPs upregulated stress?

- What is the effect of citrate-AuNPs on the structural and functional features of the DnaK chaperone?

The study seeks to investigate the effects of citrate-AuNPs on the integrity of the model *E. coli* proteome towards exploring the role of other chaperone partners and co-chaperones of DnaK during AuNPs induced cellular stress.

1.6.3. Hypothesis

DnaK functions with other chaperones and co-chaperones in conferring cytoprotection to *E. coli* cells in the wake of citrate-AuNPs induced toxicity.

1.6.4. Study Aim

The current study aims to investigate the role of DnaK together with its interaction partners and co-chaperones to *E. coli* cells exposed to citrate-AuNPs induced stress.

1.6.5. Study Objectives

1.6.5.1. Synthesis and characterization of citrate-AuNPs

- Experimental approaches
 - a) Chemical synthesis of citrate-AuNPs was undertaken by the reduction of chloroauric acid to AuNPs
 - b) Validation of the citrate-AuNPs was done using UV-vis

Further characterization of citrate-AuNPs was undertaken by DLS, FTIR, SEM, TEM, and XRD

1.6.5.2. Investigation of the effects of citrate-AuNPs on *E. coli* cells and exploring the effect of recombinant DnaK in *E. coli* cells exposed to citrate-AuNPs

- Experimental approaches
 - a) Expression levels of proteomic constituents were assessed in the absence and presence of citrate-AuNPs and quantitatively identify proteins by LC-MS/MS

- b) Effects of recombinant DnaK in *E. coli* $\Delta dnaK52$ cells exposed to citrate-AuNPs were assessed using TEM
- c) Possible interactors of DnaK were investigated with the use of co-affinity assay and LC-MS/MS respectively

1.6.5.3. Investigation of the effects of citrate-AuNPs on the structural and functional features of DnaK chaperone system in vitro

- Experimental approaches
 - a) Recombinant DnaK and DnaJ were expressed and purified using nickel affinity chromatography
 - b) The secondary structures of the recombinant DnaK were determined via far-UV circular dichroism (CD) spectroscopy analysis in the presence and absence of citrate-AuNPs
 - c) Tertiary structural conformation of the recombinant DnaK was analyzed by intrinsic (tryptophan) fluorescence spectroscopy in the presence and absence of citrate-AuNPs
 - d) The ATPase activity of the recombinant DnaK was determined using colorimetric ATP hydrolysis activity assays.
 - e) MDH aggregation suppression assays were conducted to determine the suppression of heat-induced aggregation by DnaK and citrate-AuNPs

CHAPTER 2

2. Synthesis and Characterization of Citrate-Capped Gold Nanoparticles

2.1. INTRODUCTION

Reducing gold salts with a capping or stabilizing agent has been the basis of the synthesis of gold nanoparticles (AuNPs) since the days of original Faraday preparations in the 1800s. Except for the preparation to make gold wires using sodium hydroxide yielding AuNPs (Turkevich *et al.*, 1951), chloroauric acid has had a monopoly in the preparation of gold colloids (AuNPs in solution) (Pooja *et al.*, 2011). Traditional methods to prepare AuNPs from chloroauric acid (Refer to Chapter 1, Table 1.2) were re-examined by Turkevich in 1951, and only the reduction by sodium citrate resulted in symmetrical size distribution of citrate-coated AuNPs. It is from these findings that to date sodium citrate reduction of gold salt to form AuNPs is still regarded as the standard (Muniba *et al.*, 2020; Lopes-Rodriguez *et al.*, 2020). Other methods of gold salt reduction considered to be efficient include sodium borohydride reduction (Deraedt *et al.*, 2014). It is from the reduction of gold salt by either sodium citrate or sodium borohydride that the synthesis of AuNPs with naturally occurring compounds was established and termed green synthesis. Recently, environmentally friendly procedures have been developed which rely on the first reduction of gold salt by sodium citrate or sodium borohydride followed by the addition of any other compound of interest to form a complex useful for a specific purpose. The above is also seen as the introduction of a stabilization agent or ligand exchange (Umamaheswari *et al.*, 2018; Muniba *et al.*, 2020). There are several factors to note when modifications to the surface of the AuNPs are of importance during synthesis. Factors such as temperature and reducing salt concentration have been recorded as determinants in some synthesis procedures. These factors may determine several features and properties of the particles such as shape, size, and charge (Martin *et al.*, 2010; Gagner *et al.*, 2011; Singh *et al.*, 2018). Amongst several other compounds, 3-butenoic acid is unable to reduce HAuCl_4 ions to Au^0 at room temperature thereby promoting nucleation and growth. Such compounds require elevated temperatures for reduction to occur favorably. As the temperature increases, the rate of reaction also increases (Casado-Rodriguez *et al.*, 2016). It is important to also note that citrate-AuNPs surface

features are efficiently modifiable to become biocompatible with therapeutic drugs or macromolecules (Sperling *et al.*, 2008). Although the chemical synthesis of citrate-AuNPs has been extensively studied, it is important to synthesize and characterize every batch of citrate-AuNPs to determine the specific physicochemical properties of the product. Citrate-AuNPs are ascertained using UV-Vis to ensure validity and dispersion of the particles in solution throughout the study.

2.1.1. Specific Objectives

- 2.1.1.1. To chemically synthesize gold nanoparticles using sodium citrate dihydrate
- 2.1.1.2. To characterize citrate-AuNPs using UV-spectrophotometry, scanning electron microscopy (SEM), X-ray diffraction (XRD), transmission electron microscopy (TEM), dynamic light scattering (DLS) and zetasizer
- 2.1.1.3. To determine chemical functional groups of citrate-AuNPs using fourier transform infrared spectroscopy (FTIR).

2.2. EXPERIMENTAL PROCEDURES

2.2.1. Materials

Analytical grade reagents such as hydrogen tetrachloroaurate trihydrate ($\text{HAuCl}_4 \cdot 3\text{H}_2\text{O}$) (Sigma-Aldrich, 99.99% pure) and trisodium citrate dihydrate ($\text{Na}_3\text{C}_6\text{H}_5 \cdot 2\text{H}_2\text{O}$) (Sigma-Aldrich, 99.99%) were used to synthesize colloidal AuNPs. All chemicals were utilized without further purification. The aqueous solutions were prepared using ultrapure water as a solvent. Strong acid $\text{HCl}:\text{HNO}_3$ (Aqua regia) was prepared immediately before use (Appendix B-1).

2.2.2. Synthesis of spherical gold nanoparticles

Colloidal citrate-AuNPs were synthesized by the citrate salt reduction method previously described (Zabetakis *et al.*, 2012) with a slight modification using trisodium citrate for the reduction in aqueous phase. Briefly, 0.1 mM chloroauric acid solution was prepared in ultrapure water. Glasswares were cleaned in aqua regia (Appendix B-1). A 100 ml of chloroauric solution in a three-neck condenser flask with magnetic stirrer bar, glass condenser, stoppers, and a thermometer were assembled and the

set-up was brought to boil with stirring at 100 °C. The solution was stirred continuously for a total of 30 minutes at 100 °C (Fig. 2.1). While the system boils, 1 ml of 0.01 M trisodium citrate dihydrate was added drop-wise into the stirring solution. Then boiling and stirring were further continued with a gradual change noticed in the color of the citrate gold solution being from pale yellow to deep red, then the solution further refluxed for extra 10 minutes (Zabetakis *et al.*, 2012). The solution was then cooled to 25 °C with continuous stirring. Synthesized citrate gold nanoparticles (citrate-AuNPs) were then transferred into sterile media bottles and stored at room temperature for further use.

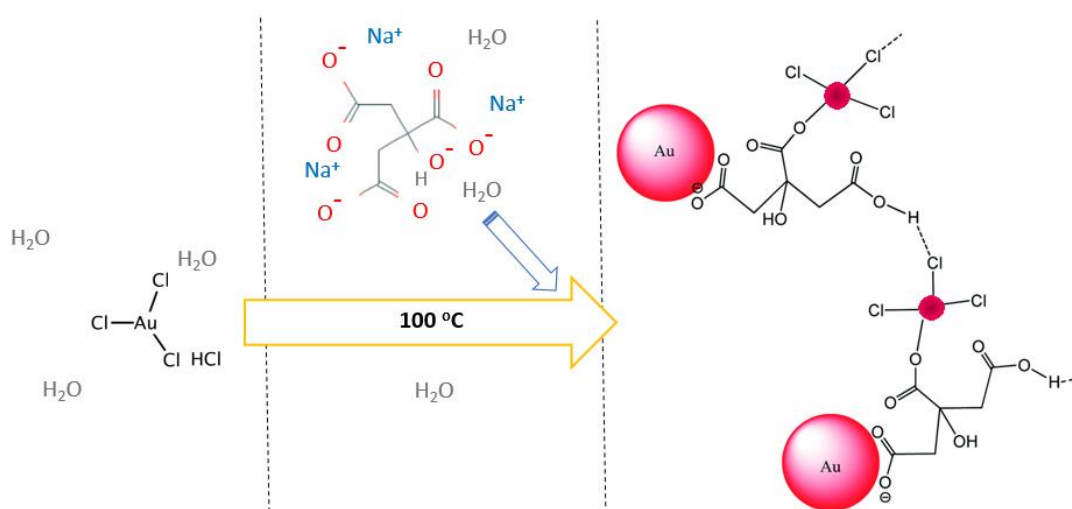


Figure 2.1. Schematic representation of the general synthetic procedure of citrate-capped gold nanoparticles. The procedure is performed at high temperatures under reflux action (Compiled from Zabetakis *et al.*, 2010; PubChem database, 2020).

2.2.3. Determination of formation, validity, and stability of synthesized AuNPs by UV-Vis

The UV-Vis-NIR Spectrophotometer was used in the validation of the formation of synthesized citrate-AuNPs. The UV-Vis absorption spectrum of synthesized citrate-AuNPs was recorded with the use of PerkinElmer UV-VIS-NIR spectrophotometer Lambda 1050 (PerkinElmer, Germany) in the wavelength ranging from 200 – 800 nm (Sobczak-Kupiec *et al.*, 2011).

2.2.4. Determination of functional groups on citrate-AuNPs by FTIR

A Bruker ATR-FTIR spectrometer (Bruker, Germany) was used to establish the integrity of the citrate-AuNPs in the range of 4000 – 400 cm⁻¹ wavenumbers. A 0.1 mg of the dried sample was analyzed under the diamond ATR after subtracting values of the empty sample holder (background values) and values of 1 mM trisodium dihydrate citrate.

2.2.5. Determination of crystallinity of citrate-AuNPs by XRD

Samples of 2.5 mg/ml citrate-AuNPs were prepared by drying out solvent from the solution using an evaporator concentrator plus (Eppendorf, Hamburg, Germany) at the highest speed overnight. For the current study, a Bruker AXS-D8 Advance X-ray diffractometer of 40 keV and 35 mA was used in the high angle 2θ range to scan the dried citrate-AuNPs sample from 25° to 90° for the structural analysis at 25 °C (Khan *et al.*, 2017). Bruker AXS-D8 was equipped with a nickel filtered Cu Kα radiation (λ = 1.5418 Å) at 40 kV, 40 mA at 25 °C. The scan speed and step sizes were 0.5 min⁻¹ and 0.01314 respectively. Transmission spectra were recorded for all the samples including the background which was an empty chamber. The crystallite sizes were calculated from the Scherrer equation (eq. 2.1) using the diffraction pattern perpendicular to the (111) plane.

$$d = K\lambda/B\cos\theta$$

$$d = 0.98\lambda/B\cos\theta \dots\dots\dots \text{(eq. 2.1)}$$

Where: *d* is the mean size of the ordered crystalline domain; *K* is the dimensionless shape factor, with a value close to a unit; λ is the X-ray wavelength, *B* is the line broadening at half maximum intensity after subtracting the instrumental baseline broadening in radians; θ is the Bragg angle in degrees.

2.2.6. Determination of morphology and size by electron microscopy

2.2.6.1. Scanning Electron Microscopy

Characterization with SEM is aimed at determining the morphology of the surface layer of citrate-AuNPs (Grys *et al.*, 2020). In this study, a Carl Zeiss ultra plus FEG SEM (Carl Zeiss, Germany) equipped with an Oxford detector (20 KeV) was used at a voltage of 10 KeV to acquire images from triplicate samples. Citrate-AuNPs were

dispersed in ultrapure water before drying on a metallic sample holder. Empty grids were used as controls.

2.2.6.2. Transmission Electron Microscopy

In this study, TEM was performed to estimate the size and to determine morphology using JEOL JEM-1010 (JEOL, Japan) electron microscope at an accelerating voltage of 100 KeV, Megaview III camera Soft Imaging Systems iTEM software. A drop of the synthesized sample solution containing 0.025 mg/ml citrate-AuNPs diluted in ultrapure water was put on a 200 mesh x 125 μm pitch copper grid with amorphous carbon and kept for 5 minutes at 25 °C to further dry before analysis. An empty copper grid with amorphous carbon was viewed under the same microscopic conditions to ascertain non-contamination. Imaging was done at an accelerating voltage of 100 kV, 20 000x magnification using a Megaview III camera and Soft Imaging Systems iTEM software at a frame size of 550 x 550 nm with 4 s image acquisition time per frame. The original version of ImageJ software was used to further calculate and validate the size of particles and the shapes using the images obtained from TEM analysis as input (Rueden *et al.*, 2017).

2.2.7. Determination of surface charge and validation of size of citrate-AuNPs

Particle size was measured by dynamic laser scattering (DLS) spectroscopy using a Malvern Zetasizer Nano ZS (Malvern Instruments, Worcestershire, United Kingdom). Each of the triplicate samples was measured diluted to 0.025 mg/ml in ultrapure metal-free water in low volume quartz cuvette (ZEN2112) sample cell holder. Light scattering was detected at 830 nm with a fixed detection angle of 90° and data were collected in automatic mode at 25°C using a solvent refractive index of 1.334. The intensity-weighted mean value was measured as the average of three independent measurements. The Zeta potential was determined using a Malvern Zetasizer Nano ZS (Malvern Instruments, Worcestershire, United Kingdom) at pH 6.8 at 25°C. Each sample was measured diluted to 0.025 mg/ml in ultrapure metal-free water to determine the Zeta potential. Net surface charge was analyzed by electrophoretic mobility using the laser doppler velocimetry and data was collected in automatic mode

at 25°C. The solvent was used as a control for both zetasizer and zeta-potential. Data were further analyzed using ZetaSizer Nano Software v3.30.

2.3. RESULTS

2.3.1. Sodium citrate salt reduces Au³⁺ ions to Au⁰ in the synthesis of gold nanoparticles

The synthesis of the uniquely sized and spherical-shaped citrate-AuNPs in this study was based on the controlled concentration of capping and stabilizing agent. Trisodium citrate dihydrate (C₆H₅Na₃O₇·2H₂O) was successfully utilized as a capping and stabilizing agent (Muniba *et al.*, 2020; Lopes-Rodriguez *et al.*, 2020). The particles were spherical shapes in solution and had a size distribution in the range 11 nm to 20 nm (Fig. 2.2C). As expected the production of AuNPs was evident as supported by the observed color change from a yellowish solution of HAuCl₄ to ruby red or grape-red in real-time. The fully synthesized citrate-AuNPs were validated using UV-VIS immediately after synthesis and a peak was observed at 520 nm and confirmed annually by monitoring agglomerates and conducting another UV-Vis validation to monitor any wavelength shift from 520 nm (Molecular Devices, USA). The synthesized citrate-AuNPs were stable for 36 months (Fig. 2.2D).

UV-Vis absorption spectrum at 520 nm indicates the formation of citrate-AuNPs. The citrate-AuNPs solution was monitored using UV-VIS throughout the study to validate stability (Fig. 2.2D) before use in biological assays. A decrease in absorbance for the first 12 months was attributed to stagnant storage longevity which could cause the formation of agglomerates at 25 °C. An absorbance intensity decrease of citrate-AuNPs without a shift in SPR was noted during the period of validation of stability and therefore particles remain valid for use in assays. The narrow peak at 520 nm (Fig. 2.2A) indicated a narrow size distribution of particles. An actual size distribution between 2 nm and 25 nm with high distribution at 11 nm of citrate-AuNPs was observed (Fig. 2.2B) to correlate with the narrow peak of the curve (Fig. 2.2A). The particles being analyzed were observed (Fig. 2.2C) in an image captured at 100 nm resolution using the TEM (Fig. 2.3C; Fig. 2.6).

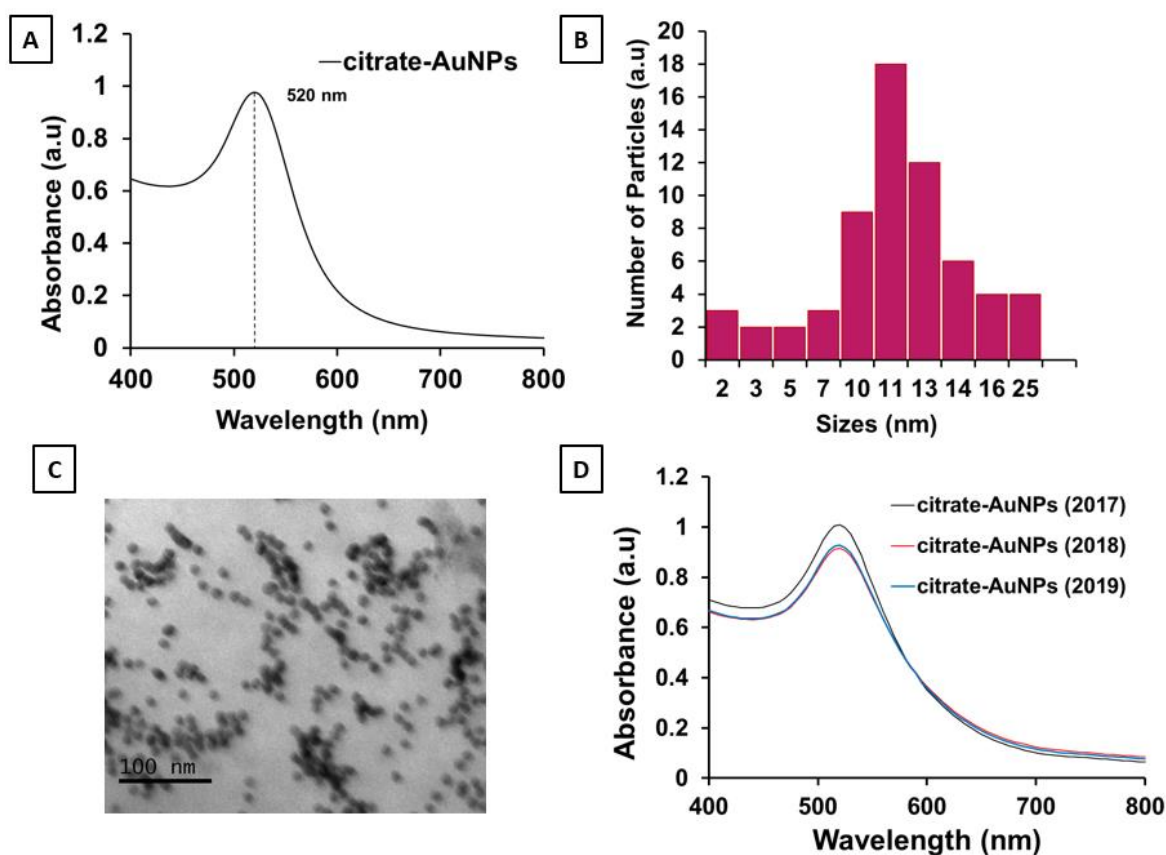


Figure 2.2. The synthesis of citrate-coated gold nanoparticles (citrate-AuNPs) was validated. Synthesis of citrate-AuNPs was validated by monitoring a spectrum of 400 nm to 900 nm wavelength. (A) UV-Vis absorption spectrum of fully synthesized citrate-AuNPs indicating an absorbance maximum 520 nm to validate the crystallinity and purity of fully synthesized citrate-AuNPs. Citrate solution was measured as a control to indicate the non-absorbance of the capping agent. (B) A histogram indicating the size distribution of citrate-AuNPs in solution. (C) TEM image of the citrate-AuNPs diluted in solution for purposes of UV-Vis absorption analysis. (D) Absorbance measure to validate citrate-AuNPs throughout the study indicating that particles remained stable at 520 nm wavelength.

2.3.2. Fourier Transform Infrared Spectroscopy (FTIR) detects possible dangling functional groups between citrate species and AuNPs

FTIR spectrum of citrate-AuNPs concentrated in ultrapure water and dried at high-speed vacuum concentrator at 25 °C (Fig. 2.3). The FTIR analysis was conducted for the determination of functional groups attached to the outer surface of the particles. The band indicating the presence of water molecules and another indicating the presence of amide groups were observed respectively at 3365.60 and 1636.25 wavenumbers which confirming the presence of hydroxyl and carboxyl groups

dangling on synthesized citrate-AuNPs. These findings agree with a previous study which observed that the anions adsorbed on citrate-AuNPs through central carboxylate groups were probed by the presence of dihydrogen anions and hydrogen bonding of carboxylic acid groups between adsorbed and dangling citrate anions (Fig. 2.3; Park *et al.*, 2014).

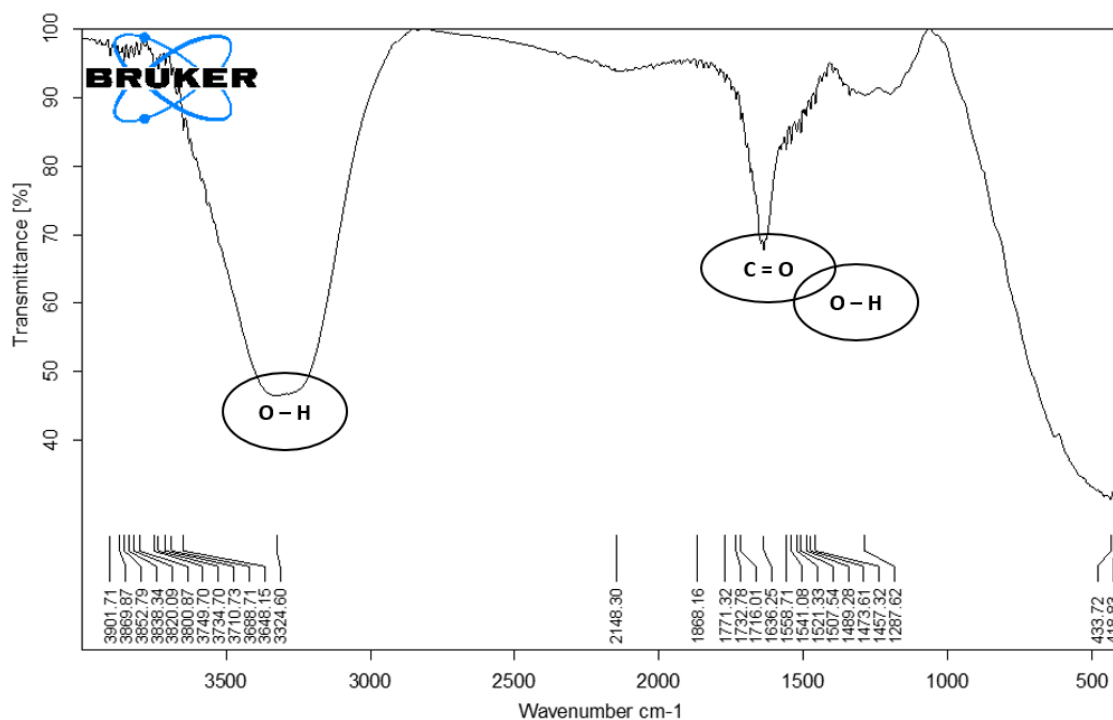


Figure 2.3. ATR-FTIR spectrum of synthesized citrate-AuNPs indicated different functional groups. Synthesis of citrate-AuNPs was monitored by a transmittance spectrum from 4000 cm^{-1} to 400 cm^{-1} wavenumbers. The spectrum of synthesized citrate-AuNPs indicated a pure composition of citrate-AuNPs in solution due to the bond stretches probed on ionic carboxylic interactions of hydrogen atoms on citrate ions with a gold core. OPUS software (Bruker, Germany) was used to analyze the distinct functional groups.

The absence of a distinct band at around 1086 cm^{-1} (arsenate) indicated non-toxicity of the citrate-AuNPs. The less exposed bands between 1650 cm^{-1} and 1440 cm^{-1} were assigned to the C=O (strong bond) and O–H (medium strength bond) stretches (carboxylic compound class).

2.3.3. XRD pattern confirms highly oriented crystallinity rate of citrate-AuNPs

The XRD patterns of the synthesized and powdered citrate-AuNPs indicated narrow diffraction peak broadness which is relative and signifies that there are crystalline particles in the samples analyzed (Fig. 2.4). An increase of theta (degrees) is evidence of the widening of peaks in XRD experimental analysis. The widening is attributed to the agglomeration of small individual particles which lead to clusters (Tshemese *et al.*, 2018). In the current study, the highest peak intensity shows that the preferred growth is in the first crystallinity phase (111) plane at 25 °C (Fig. 2.3). The diffraction peaks of the probed crystal phase were indexed to four planes (111), (200), (220), (222) and (311) in the diffractogram. These are regular repeating atoms of the citrate-AuNPs forming crystal lattice and are in arbitrary units.

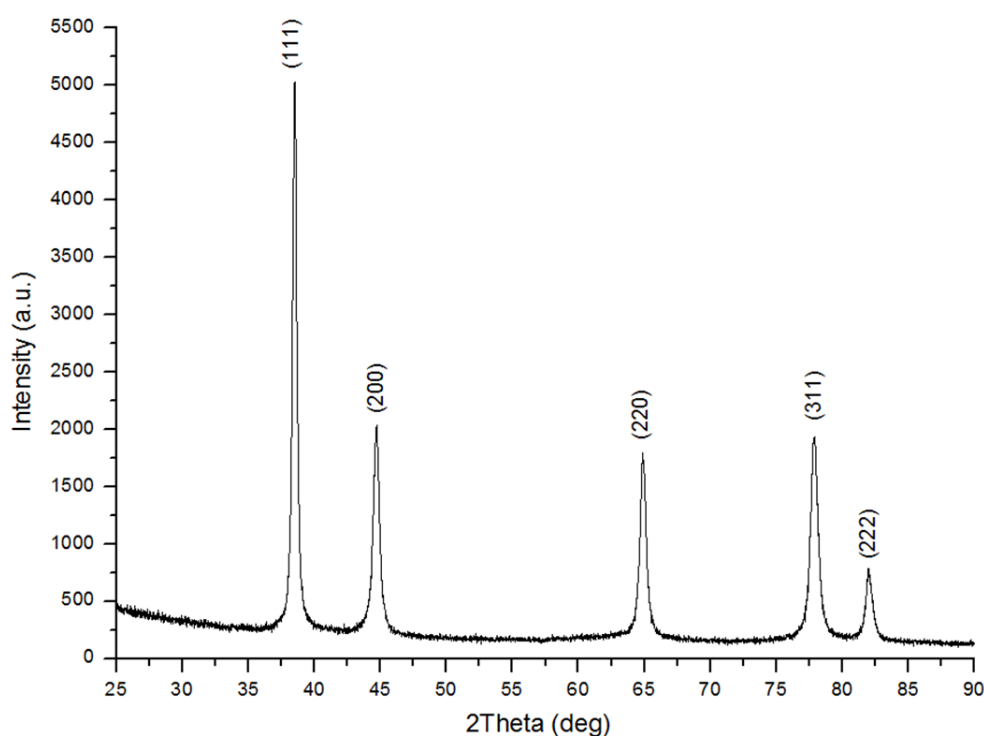


Figure 2.4. XRD diffractogram determined the basic crystalline nature of citrate-AuNPs. Citrate-AuNPs were synthesized and immediately dried with a vacuum concentrator before analysis with Bruker AXS-D8 Advance diffractometer. Particles were changed from in-solution to powder for the powder-XRD to perform efficiently. X-ray diffractometer was equipped with the copper x-ray source and set at 40 keV, 35 mA, and a high angle 2θ range from 25° to 90° at room temperature.

The crystallite sizes calculated from the Scherrer equation (eq. 2.1) using the diffraction pattern perpendicular to (111) plane were found to be 13.4 nm on average, validating the size distribution outcomes from TEM, ImageJ, and DLS analysis of around 11 nm – 25 nm which will be discussed in sections 2.3.5.

2.3.4. Scanning electron microscopy (SEM) and transmission electron microscopy (TEM) based determination of the morphology and size of the synthesized citrate-AuNPs

SEM image indicated the formation of both spherical and non-spherical shaped morphology of citrate-AuNPs obtained at 100 °C (Fig. 2.5). Although drying of citrate-AuNPs at high concentrations was necessary to determine the surface morphology, SEM images however showed that the dried citrate-AuNPs at high concentrations formed clusters (agglomerations). Therefore, citrate-AuNPs must remain in solution.

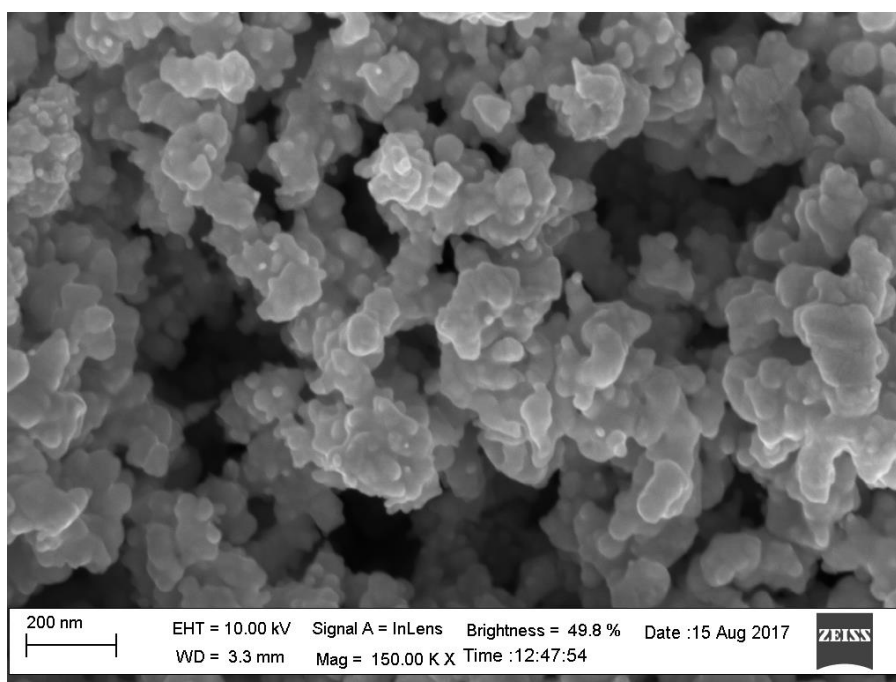


Figure 2.5. SEM image showing surface features of citrate-AuNPs including particle agglomeration due to concentration and drying. Although complete synthesis of citrate-AuNPs was already validated by monitoring a spectrum of wavelength, SEM was performed to further validate surface morphology attributed to the formation of spherical and non-spherical particles. Although particles agglomerated due to drying, it was noted that particles were predominantly spherical.

TEM analysis of citrate-AuNPs (Fig. 2.6) indicates that the nanoparticles were fully synthesized and dispersed in solution with a general spherical shape. The nanoparticle sizes have a distribution range of about 11 nm to 20 nm, largely determined by ImageJ software.

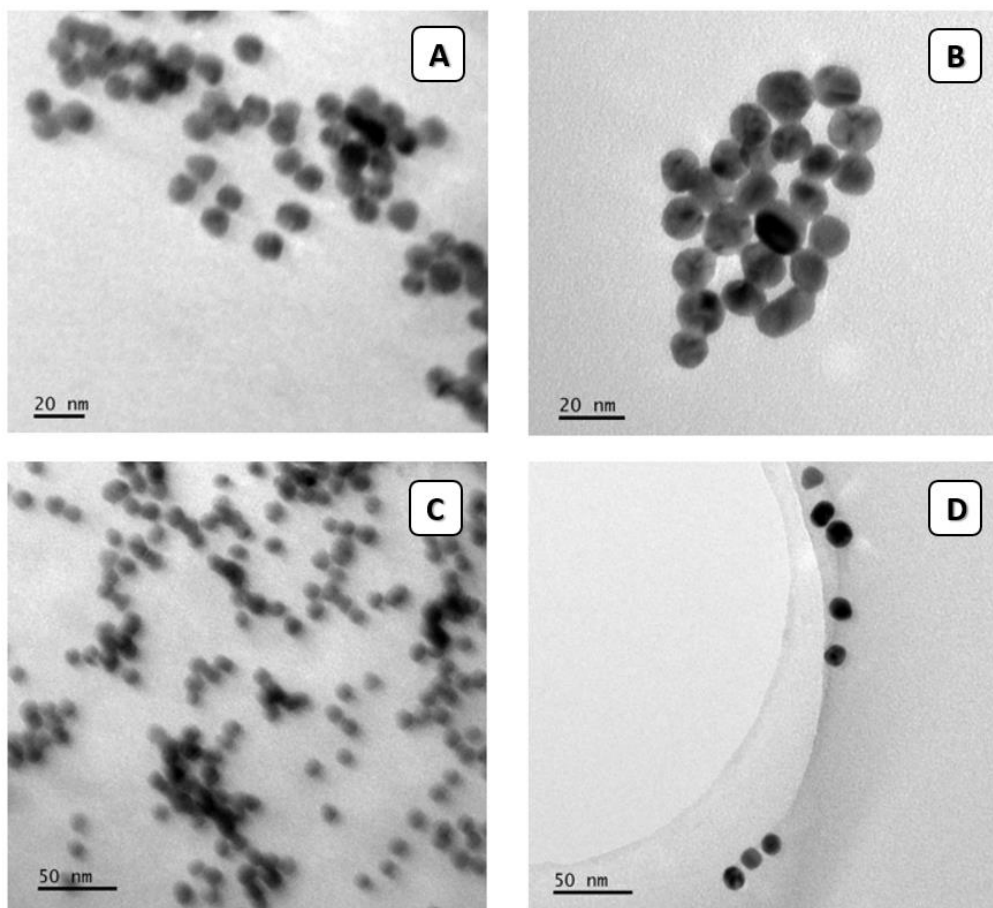


Figure 2.6. TEM image showing features of citrate-AuNPs dispersed in ultrapure water before analysis. Samples were dried completely at room temperature before the viewing was done at an accelerating voltage of 200 keV and images captured digitally using a Megaview III camera. Images were then measured using imaging systems iTEM software. TEM was performed to further validate the morphology of the particles and it was noted that particles were predominantly spherical.

2.3.5. Use of particle size analyzer zetasizer to determine the size and surface charge of synthesized citrate-AuNPs

Particle size analyser and zetasizer are methods used to measure the size of particles and charge in submicron levels respectively. Measurements are done by assessing thermal motion in response to light intensity. A concentration of 2.5 mg/ml of citrate-AuNPs diluted (1:100) in ultrapure water and analyzed indicated a range of size

distribution of about 11 nm to 20 nm that agrees with previous studies (Rodriguez *et al.*, 2018). The synthesis procedure used was targeting about 13 nm size of citrate-AuNPs and this was achieved (Fig. 2.6; 2.7). Although a different technique of size analysis was used by Makumire *et al* (2015), the size range of citrate-AuNPs agrees in principle. An indication of agglomeration of higher concentration of citrate-AuNPs was observed with the 500 µg/ml citrate-AuNPs which indicated a much smaller volume percentage of NPs at 13 nm as compared to much higher dilution of 100 µg/ml citrate-AuNPs (Fig. 2.7).

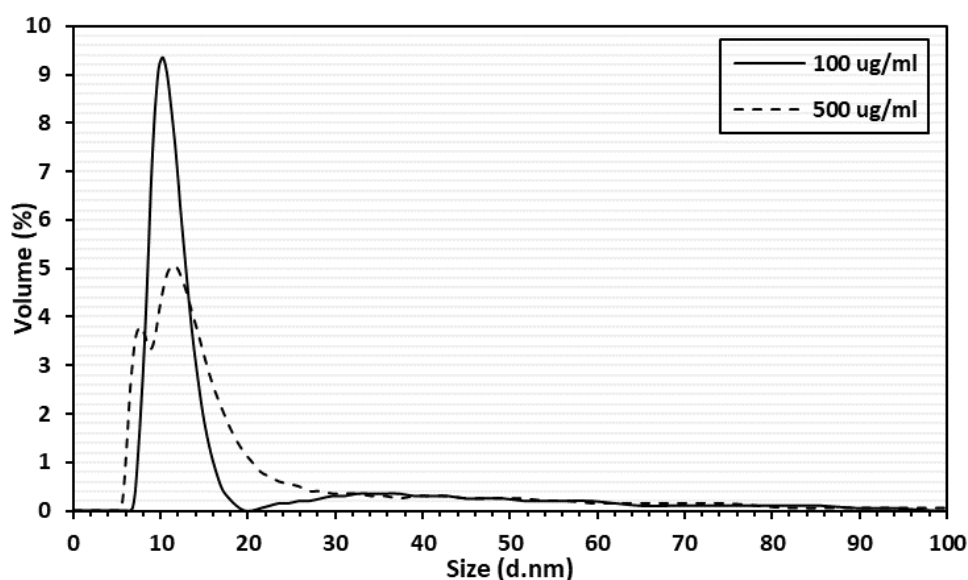


Figure 2.7. Size distribution analysis of the citrate-AuNPs dispersed in ultra-pure water was performed between the minimum and maximum concentration recommended for samples. Citrate-AuNPs were synthesized and immediately centrifuged and dispersed in ultrapure water before analysis. A 0.1 mg/mL of each resulting dispersion was transferred to a 1 ml quartz low volume cuvette and subjected to DLS measurements. DLS measurements show a much wider size distribution from both dilution concentration and a sizeable distribution was observed from around 5 nm – 30 nm which is then followed by a non-significant distribution from around 20 nm – 90 nm.

The zeta potentials (ζ) calculated by measuring the electrophoretic mobility of citrate-AuNPs as a streaming potential surrounding the electric double layer of oscillating electric fields indicated a slightly negative charge of the widely distributed (100 %) citrate-AuNPs in solution (Fig. 2.8). The negative charge of -1.45 mV (Table 2.1; Fig. 2.8) is due to charge stabilization between gold core and citrate ions which also gives

an advantage to less agglomeration due to electrostatic repulsion of tri-anionic citrate species hanging or dangling on AuNPs within the solution.

Table 2.1. AuNPs exhibit a slightly negative charge.

Temperature (°C)	25	Zeta Runs	15
Count Rate (kcps)	133.1	Attenuator	10
Cell Description	Clear zeta cell		
		<i>Mean (mV)</i>	<i>Area (%)</i>
Zeta Potential (mV)	-1.45	Peak 1	-1.45
Zeta Deviation (mV)	3.44	Peak 2	0
Conductivity (mS/cm)	0.42	Peak 3	0
			<i>St Dev (mV)</i>
			3.44
			0
			0

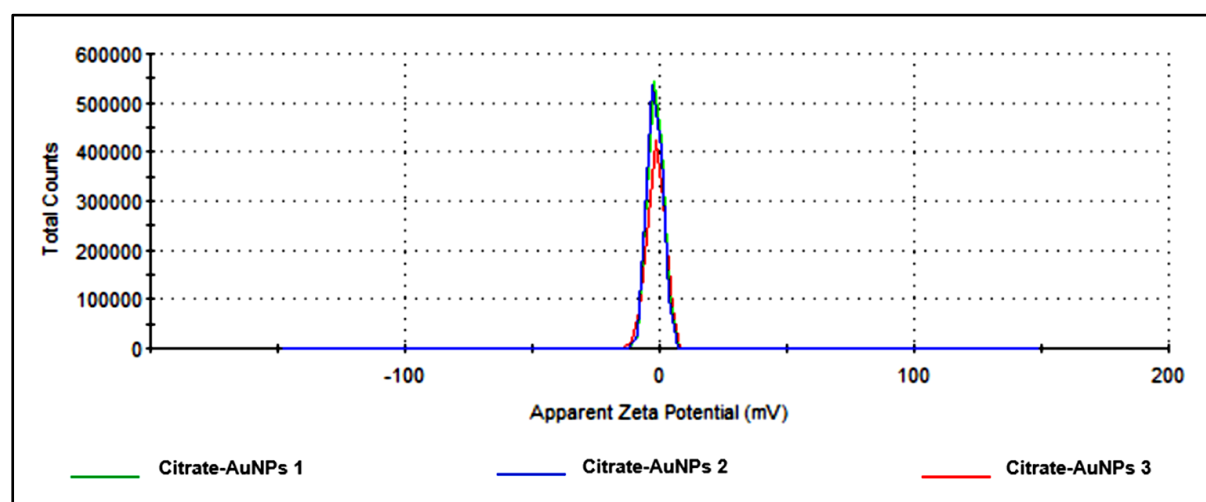


Figure 2.8. Zeta potential analysis of citrate capped AuNPs dispersed in ultra-pure water. Citrate-AuNPs were dispersed in ultrapure water (Dispersant RI, 1.330) before analysis with Zetasizer DLS a viscosity and dielectric constant of 0.8872 and 78.5 respectively. All 20 zeta runs were performed at room temperature. All particles indicated a slightly negative average *ZP* in solution.

2.4. DISCUSSION

This study aimed at synthesizing and characterizing citrate-AuNPs. Apart from UV-Vis used to validate the synthesis of nanoparticles, other techniques used to analyze features of the citrate-AuNPs included ATR-FTIR, XRD, SEM, TEM, and DLS. Controlled synthesis of AuNPs by sodium citrate gave rise to particles of diameter less than 100 nm exhibiting a surface plasmon resonance (λ_{SPR}) between 510 – 530 nm (Umamaheswari *et al.*, 2018; Luthuli *et al.*, 2014; Ni *et al.*, 2019) confirming the complete reduction of chloroauric gold salt to citrate-AuNPs. It is important to note that

λ_{SPR} has a relation to the resulting diameter of synthesized citrate-AuNPs since broadening of the λ_{SPR} peak is caused due to resulting size increase, agglomeration, or nucleation of nanoparticles during synthesis. It is also the basic principle behind the applications of many color-based biosensors (González-Díaz *et al.*, 2008). Notably, the coating agent trisodium citrate dihydrate herein used and referred to as capping agent played the role of three agents by reducing Au^{3+} to Au^0 while capping, stabilizing, and dispersing the synthesized citrate-AuNPs. The plasmon wavelength (λ_{max}) shows the size distribution of citrate-AuNPs which was later revealed by analysis with other techniques. In this study, λ_{max} is approximately at 520 nm and did not give any shift even after a prolonged shelf-life of 36 months, enabling the study to continue into subsequent assays with the same batch of nanoparticles. Nucleation and growth of the particles in solution were not observed, further confirming the integrity of the particles.

TEM analysis of citrate-AuNPs indicated that NPs were fully synthesized, spherical, and well dispersed as expected, and that the higher percentage of nanoparticle sizes has a distribution range of less than 50 nm. An insignificant quantity of nanoparticles around 20 – 90 nm in size distribution can be observed with DLS. The zeta potentials (ζ) were calculated by measuring the electrophoretic mobility of citrate-AuNPs as a streaming potential surrounding the electric double layer of oscillating electric fields (Mandiwana *et al.*, 2018). *et al.*, 2018). The small size at around 20 nm and the slightly negative charge of citrate-AuNPs present a potential to bind or adsorb and enter positively charged bacterial cell walls. The possibility of entering negatively charged bacterial cell walls exists in agglomerated forms of citrate-AuNPs which forcefully break cell walls.

Spherical shapes of citrate-AuNPs agglomerated by drying in a concentrator are observed through SEM analysis of surface morphology (Fig. 2.5). The nanoparticle shape observed here as spherical has been demonstrated to influence particle uptake into cells (Makumire *et al.*, 2015). Spherical nanoparticles are also generally desirable to produce optimal optical properties for potential absorption into cells. The synthesized citrate-AuNPs were examined for structure and phase purity by XRD. Apart from the purity of the sample, XRD also determines the extent of agglomeration in liquid samples. The XRD patterns of the citrate-AuNPs were recorded in a spectrum of 2θ from 25° to 90° , and the results showed the presence of the five characteristic

planes (111), (200), (220), (311) and (222) of the spherical citrate-AuNPs. These results are in line with many other reports (Deręgowska *et al.*, 2013) and confirm the formation of crystalline, non-aggregated citrate-AuNPs (Bharathiraja *et al.*, 2016). While sharp plane (111) peak at 2θ of about 38.81 indicates a highly oriented crystallinity rate in citrate-AuNPs, it is the best stabilized low energy plane provided with a high catalytic surface. The particles synthesized demonstrated crystalline potential to interact and influence living cells as metallic ions carrying materials. This is a crystalline nature obtained with similar crystallite phases for the different analyses performed experimentally (Ogundare *et al.*, 2019).

FTIR confirmed the existence of citrate-capped nanoparticles by revealing the absence and presence of various infrared marker bands. Although amide and O–H bands could not be distinct due to the formation of stabilization between citrate ions and gold colloid metallic core, there exist multiple amide stretches ($\sim 1500 - 1700 \text{ cm}^{-1}$) which were expected along with characteristics $-\text{CH}_2$ and $-\text{CH}_3$ groups of citrate capping and stabilizing agent. The O–H functional groups at 3324.6 cm^{-1} observed in the spectra of both sodium citrate as a control and that of the particles could be involved in the formation of citrate-AuNPs or to a lesser extent be detected due to the ultrapure water used as suspension solvent. Similar observations about the distinct O–H band were reported for the green synthesis of AuNPs (Patil *et al.*, 2018). The C=O around the same band is a direct result of dangling carboxyl groups on AuNPs. The absence of a distinct band at around 1086 cm^{-1} (arsenate) indicated non-toxicity of the citrate-AuNPs in analysis, which also confirms citrate-AuNPs stable in solution. vibration between capping citrate ions and gold particle core. Functional groups are exposed in solution when the adsorbed citrate interacts with each other through hydrogen bonds between the terminal carboxylic acid groups. Therefore, the existence of carbon double bond oxygen atoms and carbon single bond hydrogen indicates the bond stretches representing interactions between citrate ions and gold core. The citrate chains interact with each other through van der Waals attraction between directly opposite CH_2 groups, the process leads to the formation of a self-assembled layer of citrate molecules tightly adsorbed to AuNPs crystal surfaces (Fig. 2.3). The monolayer exposes the dangling citrate species with carboxylic and hydroxyl groups detected by FTIR.

CHAPTER 3

3. The effects of citrate-AuNPs in *E. coli* cells and exploration of their effects on DnaK structure-function features

3.1. INTRODUCTION

Gold nanoparticles (AuNPs) continue to gain traction in respect to their application in several biomedical fields. However, their effective usage is impeded by a limited understanding of their interaction with proteins. It is believed that when AuNPs interact with proteins to form complexes, AuNPs acquire some biological identity which cascades down facilitating their recognition by other biological entities (Giri *et al.*, 2014). No clear evidence of interaction of citrate-AuNPs with *E. coli* proteomic constituents containing possible expressed molecular chaperones is available in literature. Therefore, evaluation of expression levels of *E. coli* molecular chaperones such as DnaK, ClpB, DnaJ, and GroEL is important (Gomes *et al.*, 2019).

The action of molecular chaperones in a stressful environment is seen when certain chaperones are upregulated against some which are down-regulated as an indication of increased induced oxidative stress (Barreto *et al.*, 2020). Molecular chaperones are maintained in an appropriate ratio to the level of unfolded polypeptides in the cell. An increase in unfolded polypeptides triggers over-expression of certain molecular chaperones such as DnaK (Wang *et al.*, 2018) and GroEL/ES (Bukau *et al.*, 2006).

The presence of AuNPs may induce an overaccumulation of unfolded peptides which may in turn trigger differential expression of chaperones to enhance stress tolerance. In the case where AuNPs do not enhance any differential expression of chaperones and other key enzymes allowing cells to maintain their proteostasis, they are regarded as stable molecules which could be used in applications such as drug delivery and imaging without cellular interference (Rodriguez *et al.*, 2014; Fratoddi *et al.*, 2019; Chatterjee *et al.*, 2020).

There is a need to distinguish or determine the abundant constituents of the soluble against the insoluble proteomic constituents in cells since soluble proteins are known to possess properly folded structures for function.

Mutant *E. coli* strain devoid of DnaK (MC4100 Δ *dnaK52::CmR sidB1*) function has been reported to lose cell viability when exposed to elevated temperatures (Paek and Walker, 1987). Report of complementary assays conducted in cells expressing exogenous DnaK and cells deficient in DnaK chaperone (*E. coli* Δ *dnaK52*) exhibited cellular damage which may have led to protein misfolding and aggregation within *E. coli* Δ *dnaK52* (Paek and Walker, 1987). Normal cell growth and cellular division were observed when a plasmid possessing the *dnaK* gene was introduced into *E. coli* Δ *dnaK52* mutant at 42°C (Paek and Walker, 1987), highlighted the importance of DnaK in *E. coli*. The presence and function of other chaperones and co-chaperones of DnaK have not been thoroughly studied. In this study, citrate-AuNPs were introduced as cell stressors to ascertain the cellular response through the expression of molecular chaperones. Although some studies reported toxicity of AuNPs to cells, DnaK has been reported to function alongside AuNPs to prevent aggregation of non-native proteins within cells (Makumire *et al.*, 2015; Gomes *et al.*, 2019).

This study explored the role of DnaK and its functional partners in the alleviation of possible AuNPs induced cellular stress. Quantitative evaluation by LC-MS may provide a comprehensive insight into the global response of *E. coli* cells to nanoparticles, which will aid in elucidating the underlying antibacterial mechanism involving aggregation of both membrane and cytosolic proteins (Gomes *et al.*, 2019).

3.1.1. Specific Objectives

- 3.1.1.1. To assess the expression levels of selected proteomic constituents by *E. coli* cells in response to AuNPs exposure
- 3.1.1.2. To investigate the role of DnaK in response to citrate-AuNPs toxicity using complementation assay
- 3.1.1.3. To investigate and identify possible interaction partners of DnaK by co-affinity assay and LC-MS/MS respectively

3.2. EXPERIMENTAL PROCEDURES

3.2.1. Materials

The *E. coli* O157:H7 clinical isolate strain was obtained from Prof Samie Amidou's bacteriology lab of the University of Venda. *E. coli* Δ *dnaK52* strain, BB1553 (MC4100 Δ *dnaK52::CmR sidB1*) (Georgopoulos *et al.*, 1979) and plasmid *pQE30/dnaK* encoding for *E. coli* DnaK (Shonhai *et al.*, 2005; Makhoba *et al.*, 2016) were used. Citrate-AuNPs were prepared (Chapter 2, Section 2.1). Other reagents used in this study are listed in Appendix D-16.

3.2.2. Expression and evaluation of *E. coli* O157:H7 proteomic constituents in the presence of citrate-AuNPs cell stressors

The study was conducted to quantitatively identify the proteomic constituents of *E. coli* O157:H7 which are differentially expressed in the presence of citrate-AuNPs. The study also investigated the possible interaction of recombinant DnaK with proteomic constituents of *E. coli* Δ *dnaK52* exposed to citrate-AuNPs.

In the current study, analysis of proteome *E. coli* strain O157:H7 when exposed to varying concentrations of citrate-AuNPs under normal growth conditions (37 °C) was conducted to determine the expression of select proteins.

E. coli O157:H7 cells were grown as previously described (Haupt *et al.*, 2014; Stachelska and Charmas, 2018). Briefly, freshly defrosted stock of *E. coli* O157:H7 cells were plated on double-strength tryptone soy with 0.6 % (w/v) yeast extract (2x TSBYE) agar under septic conditions and incubated at 37 °C overnight. A single colony was inoculated in 2x TSBYE broth and incubated at 37 °C overnight with moderate shaking at 100 rpm. The overnight culture was transferred into fresh 2x TSBYE broth and was divided into five separate flasks when OD₆₀₀ was at 0.6. Citrate-AuNPs at concentrations 0 – 100 µg/mL (Appendix C-3; Table C-3) were added into each separate flask. Fresh media (2x TSBYE) with varying doses (0 µg/ml – 100

µg/ml) of citrate-AuNPs was used as an observation experimental control to monitor possible contamination and for blanking the growth curve of each growth experiment. Initially, all concentrations of citrate-AuNPs were suspended in 2x TSBYE broth without bacterial cultures, incubated at 37 °C with shaking (200 rpm) shaking for five hours. Each concentration was averaged for an absorbance value at OD₆₀₀. Cultures with citrate-AuNPs were also incubated at 37 °C with shaking (200 rpm) shaking for a further five hours before harvesting. Harvested cells were subjected to sodium dodecyl sulphate-polyacrylamide gel electrophoresis (SDS-PAGE) analysis and proteins were subsequently excised and identified by LC-MS/MS (Section 3.2.3). Expression level of proteins was analysed with the use of IBM statistical package for social sciences (SPSS) version 27 statistical analytical tool (<https://www.ibm.com/za-en/analytics/spss-trials>). Regression test was performed to determine effect of continuous variables on another variable while one-way analysis of variance (ANOVA) was performed to estimate how independent variables affect a dependent variable.

3.2.3. Identification of the interaction partners of DnaK associated with citrate-AuNPs induced cell stress

To identify proteins interacting with DnaK to confer cytoprotection to *E. coli* cells under moderate as well as excessive concentrations of citrate-AuNPs, LC-MS/MS was used. Mass spectrometric identification of DnaK and its possible interaction partners was conducted as previously described (Sharma *et al.*, 2017). Briefly, proteins co-eluted with DnaK were separated on 10 % SDS-PAGE (1D). Proteins on the 1D gel were Silver stained and imaged with ChemiDoc™ (BioRad, USA) image analyzer (Fig. 3.4). Protein bands were manually excised and digested with trypsin (Promega, USA) before identification with LC-MS/MS. Extraction buffer (1:2 (v/v) 5 % formic acid/acetonitrile) was added to digested peptides, vortexed and incubated for 30 minutes at 37 °C. Extracted peptide samples were then subjected to LC-MS/MS analysis which was performed on LTQ Orbitrap Velos LC-MS/MS (Thermo Fischer, UK) connected to an ESI mass spectrometer. The generated MS data were searched against the *E. coli* subset of the Uniprot *E. coli* reviewed cRAP FASTA database (<ftp://ftp.thegpm.org/fastacRAP>; 29,023 sequences) by Mascot (Matrix Science, USA). The Mascot results were further subjected to a subset search by XTandem

followed by determination of probability assessments of the peptide assignments and protein identifications by Scaffold (version 4.10.0, Proteome Software Inc., USA) (Searle, 2010). The scaffold was used to validate MS/MS- based peptide and protein identifications. Peptide identifications were accepted if they could be established at greater than 82.0% probability. Peptide probabilities from MS-Amanda Proteome Discoverer and Sequest were assigned by the Scaffold Local FDR algorithm. Peptide probabilities from XTandem were assigned by the Peptide Prophet algorithm (Mohammed *et al.*, 2016) with Scaffold delta-mass correction. Protein identifications were accepted if they could be established at greater than 6.0 % probability and contained at least 3 identified peptides. Protein probabilities were assigned by the Protein Prophet algorithm (Nesvizhskii *et al.*, 2003; Mazur *et al.*, 2011). Proteins that contained similar peptides and could not be differentiated based on MS/MS analysis alone were grouped to satisfy the principles of parsimony. Proteins sharing significant peptide evidence were grouped into clusters (Moreiras *et al.*, 2018).

3.2.4. Confirmation of the pQE30/*dnaK* and pQE30 vector plasmid

The integrity of the DNA segment encoding for DnaK (pQE30/*dnaK*) together with that of the plasmid pQE30 vector (Makhoba *et al.*, 2016; Lebepe *et al.*, 2020) was confirmed by restriction digest and agarose gel electrophoresis (Appendix C-4, D-10).

3.2.5. Determination of soluble proteomic constituents of *E. coli* Δ *dnaK52* exposed to citrate-AuNPs stress inducers

Solubility analysis of proteins expressed in *E. coli* Δ *dnaK52* exposed to citrate-AuNPs was conducted as previously described (de Marco, 2007; Wang *et al.*, 2018). A solubility study was performed to ascertain the extent to which cytosolic proteins remain soluble in the presence of citrate-AuNPs. Cell line *E. coli* Δ *dnaK52* strain, BB1553 (MC4100 Δ *dnaK52::CmR sidB1*) was transformed with pQE30/*dnaK* and pQE30 plasmids (Appendix C-4, E-10). Transformants were then inoculated and grown in separate double strength yeast tryptone (2x YT) broth (Yeast extract, 1.0 %; tryptone, 1.6% and sodium chloride, 0.5%) supplemented with 35 μ g/ml chloramphenicol and 100 μ g/ml ampicillin and incubated at 30 °C overnight with

moderate shaking. Overnight cultures were then upscaled tenfold by transferring into fresh 2x YT broth and cultures were allowed to grow to mid-log phase ($OD_{600} = 0.6$) at 30 °C. The overexpression of the recombinant DnaK was induced at mid-log phase with 1 mM IPTG. Cultures were then divided into parts and grown for further 5 hours until an $OD_{600} = 2.00$ (Post induction). Cells were centrifuged at $5000 \times g$ for 15 minutes to harvest and pellets were suspended in TBS buffer (20 mM Tris-HCl, 150 mM NaCl, pH 7.4). Following another centrifugation of pelleted cell suspensions at $5000 \times g$ for 15 minutes, the washed pellets were further suspended in ice-cold (10 % w/v) TBS buffer with Halt™ protease cocktail inhibitor (0.1 % v/v) The suspension was then mixed with an equal volume of lysis buffer (20 mM Tris-HCl, 150 mM NaCl, pH 7.4 and 500 µg/ml lysozyme) and immediately incubated on ice for 60 minutes with agitation. It was then frozen at -80 °C for 60 minutes before thawing. Each culture of *E. coli* $\Delta dnaK52$ was exposed to a citrate-AuNPs concentration ranging from 0 – 50 µg/ml and incubated on ice with agitation for 60 minutes before centrifugation at $12,000 \times g$ for 5 minutes to collect possible soluble proteomic constituents against insoluble and agglomerated particles. Both pellets and clarified supernatants were washed with TBS buffer to clear any unbound proteins from citrate-AuNPs and kept for SDS-PAGE analysis.

3.2.6. Assessment of the role of DnaK in *E. coli* cells exposed to citrate-AuNPs

This study sought to validate that the model *E. coli* $\Delta dnaK52$ strain cells used with the synthesized citrate-AuNPs agree with that of previous studies. Bacterial cell specimens were prepared as previously described (Makumire *et al.*, 2015). Briefly, cell line *E. coli* $\Delta dnaK52$ strain, BB1553 (MC4100 $\Delta dnaK52::CmR sidB1$) was transformed with *pQE30/dnaK* and *pQE30* plasmids. Transformants were then inoculated and grown in separate 2x YT broth as described in section 4.2.5 until the induction of the overexpression of the recombinant DnaK at mid-log phase with 1 mM IPTG. Cultures were then divided into parts before the addition of varying concentrations from 0 µg/ml, 2.5 µg/ml, and 50 µg/ml and grown for further 5 hours until an OD_{600} reading of 2.00 (Post induction). Cells were then centrifuged and harvested before suspension in sodium phosphate buffer (100 mM Na_2HPO_4 , 100 mM NaH_2PO_4 , pH 7.4). Following several washes with phosphate buffer, specimens were fixed with 2.5 %

glutaraldehyde for 4 hours and rinsed several times thereafter. Specimens were then quenched in 100 mM glycine solution for 20 minutes and subsequently incubated in 200 mM Sucrose solution overnight in the cold. Specimens were then incubated in two changes of 70 % ethanol for 30 minutes each. Then incubated in a mixture of L.R. White and 70 % ethanol (2:1). Specimen were kept in the last change of L.R. White overnight at room temperature before polymerization in 60 °C oven for 48 hours. Ultrathin sections were cut at 90 nm and collected on nickel grids and allowed to dry overnight before staining with uranyl acetate and lead citrate. Visualization was performed using a JEOL JEM-1010 at an accelerating voltage of 200 KeV. A specimen-embedded nickel grid was kept for 5 minutes at room temperature for further drying before analysis (Naz *et al.*, 2016).

3.2.7. Identification of the interaction partners of *E. coli* DnaK

Several protein partners of DnaK, be it direct physical or intermittent interactors within the *E. coli* proteome are known (Yu *et al.*, 2010; Calloni *et al.*, 2012). Within *E. coli*, at least 300 proteins must interact with the GroEL-ES system to complete their proper folding (Ami *et al.*, 2013), the role of DnaK, ClpB, DnaJ, NEFs among other molecular chaperones have been elucidated (Lee *et al.*, 2003; Kityk *et al.*, 2012; Wang *et al.*, 2013). To assess the effect of citrate-AuNPs on the interaction of recombinant DnaK with proteome constituents from prey lysates, a pull-down assay on the Ni²⁺-chelating column was used to isolate DnaK interaction complexes expressed in prey lysates (Rodina *et al.*, 2011). Here, the identification of several proteomic constituents interacting with recombinant *E. coli* DnaK was investigated. A first attempt to modify and influence the binding of DnaK interaction partners is performed with the addition of varied citrate-AuNPs concentrations. Both *E. coli* $\Delta dnaK52$ transformed with *pQE30* and *E. coli* $\Delta dnaK52$ transformed with *His₆-tagged pQE30/dnaK* in previous experiments (Appendix D-1) were grown in 2x YT broth as previously described (Makumire *et al.*, 2015). Both cultures were grown to mid-log phase and *E. coli* $\Delta dnaK52$ transformed with *pQE30/dnaK* culture was induced with 1 mM IPTG while *E. coli* $\Delta dnaK52$ transformed with *pQE30* was divided into parts before treatment with varying concentrations of citrate-AuNPs (0 μ g/ml – 100 μ g/ml). Both cultures were further grown for five hours at 30 °C. Co-affinity chromatography was conducted using

a Thermo Scientific Pierce Protein Interaction kit (Thermo Scientific, USA), with modifications and an indication of control and experimental for the exposure of cell lysates to citrate-AuNPs (Table 3.2). Briefly, for preparation of bait protein lysate, 50 mL of *E. coli* Δ *dnaK52 pQE30/dnaK* culture was harvested and suspended in 5 mL of TBS buffer. Following the centrifugation of cell suspension at 5000 \times *g* for 5 minutes, the washed pellet was suspended in TBS buffer with Halt™ protease inhibitor cocktail. The suspension was then mixed with an equal volume of lysis buffer (20 mM Tris-HCl, 150 mM NaCl, 5 % SDS, pH 7.4) and immediately incubated on ice for 60 minutes. The mixture was then centrifuged at 12,000 \times *g* for 5 minutes to retain the clarified supernatant lysate. The lysate was kept as bait. For the preparation of prey protein lysate exposed to varied citrate-AuNPs, 50 mL of *E. coli* Δ *dnaK52 pQE30* culture was also harvested and clarified similarly as for the preparation of bait except for 10 mM imidazole that was added before prey protein capture. The lysate was kept as prey. For the preparation of affinity beads, each volume of 50 μ L of HisPur™ cobalt resin was washed with 400 μ L of the wash buffer (TBS: Lysis buffer (1:1) containing 10 mM Imidazole and repeated for a total of three washes. Recombinant (His)₆-tagged DnaK lysate was then added to the HisPur cobalt resin and immobilized at 4 °C for at least an hour before collection of flow-through and subsequent washes to effectively eliminate nonspecific bindings or interactions. For prey protein capture, a 600 μ L of prepared prey protein lysate was added to the immobilized bait protein and incubated at 4 °C for 60 minutes with gentle rocking motion on a rotating platform. After collection of flow-through, the immobilized mixture of protein lysate was washed to a total of three repeats before bait-prey protein elution. To each column, 250 μ L of the elution buffer (290 mM Imidazole in wash buffer) was added to the spin column and incubated for 5 minutes with gentle rocking motion on a rotating platform before centrifugation at 1250 \times *g* for 30 seconds to collect the bait-prey protein mixture. SDS-PAGE was employed for the detection of candidate interacting proteins across all concentrations of treatment with citrate-AuNPs. SDS-PAGE gels were stained using Pierce® Silver Stain Kit per manufacturer's instruction without modification (ThermoScientific, USA; Appendix C-2). LC-MS was used to identify possible interactors of DnaK (Protocol: Section 4.2.3).

Table 3.2. Indication of experimental and controls for co-affinity assay.

Exp/Control	Samples	IPTG	Treatment
Prey Control	<i>E. coli</i> Δ <i>dnaK52</i> <i>pQE30</i>	x	None
Prey Experiment 1	<i>E. coli</i> Δ <i>dnaK52</i> <i>pQE30</i>	x	2.5 μ g/ml AuNPs
Prey Experiment 2	<i>E. coli</i> Δ <i>dnaK52</i> <i>pQE30</i>	x	50 μ g/ml AuNPs
Bait	<i>E. coli</i> Δ <i>dnaK52</i> <i>pQE30/dnaK</i>	√	None

3.3. RESULTS

3.3.1. Expression of proteomic constituents of *E. coli* O157:H7 subjected to citrate-AuNPs induced stress

Bacterial growth assays were conducted to evaluate the effect of citrate-AuNPs on the growth rate. Bacterial growth assays were complemented by staining and visualizations of the proteins expressed during the process of cell growth in the presence of citrate-AuNPs. Using LC-MS, expressed proteins were quantitatively identified and evaluated for the changes thereof.

E. coli O157:H7 strain is known to grow at temperatures between 55 °C and 62 °C at pH7 and moderately grow at pH4 at the same temperatures (Stachelska, 2015; Suehr *et al.*, 2020). To this effect, the growth rate of the control (cells exposed to 0 μ g/ml citrate-AuNPs) had a notable difference with that of the growth rate of cells exposed to 2.5 μ g/ml citrate-AuNPs ($p < 0.05$). Cells exposed to citrate-AuNPs concentrations above 5 μ g/ml up to 50 μ g/ml were observed to grow exponentially with a much notable inhibition ($p < 0.01$) (Fig. 3.1). Cells exposed to concentrations from 5 μ g/ml – 50 μ g/ml citrate-AuNPs were observed to be inhibited at 150 minutes which was half an hour after exposure to citrate-AuNPs. The growth trend after the inhibition at 150 mins was exponential for all the cells exposed to citrate-AuNPs at increasing levels of concentrations. The difference in the growth rate of *E. coli* O157:H7 in the presence of 2.5 μ g/ml citrate-AuNPs compared to 5 μ g/ml – 50 μ g/ml citrate-AuNPs was also notable ($p < 0.01$). There was no difference noted in the effect of all concentrations from 5 μ g/ml – 50 μ g/ml citrate-AuNPs ($p > 0.05$).

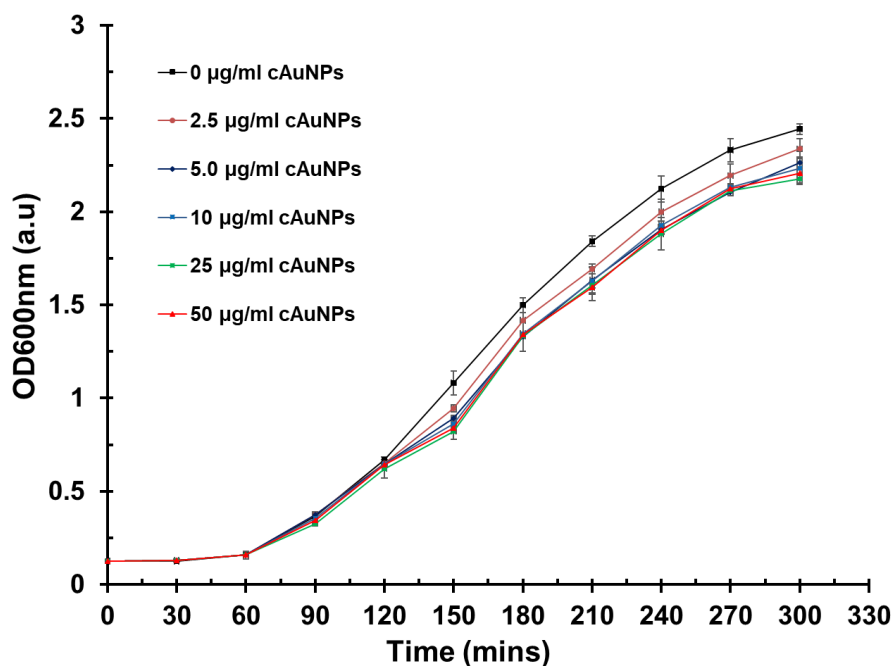


Figure 3.1. *E. coli* O157:H7 growth curve in the presence of citrate-AuNPs. The *E. coli* O157:H7 strain was grown in fresh 2x TSBYE at 37 °C and 200 rpm shaking. The point at 120 mins indicated the addition of citrate-AuNPs at OD₆₀₀ = 0.6. Each concentration of citrate-AuNPs is indicated. Error bars were generated from data obtained using independent *E. coli* O157:H7 growth monitoring experiments. Statistical significance was determined by using regression test.

The growth curve (Fig. 3.1) indicated differences between control cells and the rest of the cells exposed to varying concentrations of citrate-AuNPs by absorbance values at time points from 150 mins. Proteome analysis indicated insignificant differences across all concentrations of citrate-AuNPs visualized by coomassie staining (Fig. 3.2). None of the highly expressed proteins indicated any upregulation or downregulation across control and through increasing concentrations of citrate-AuNPs experiments determined by LC-MS. Citrate-AuNPs were non-toxic to *E. coli* O157:H7 at any concentration and given time point during growth rate studies.

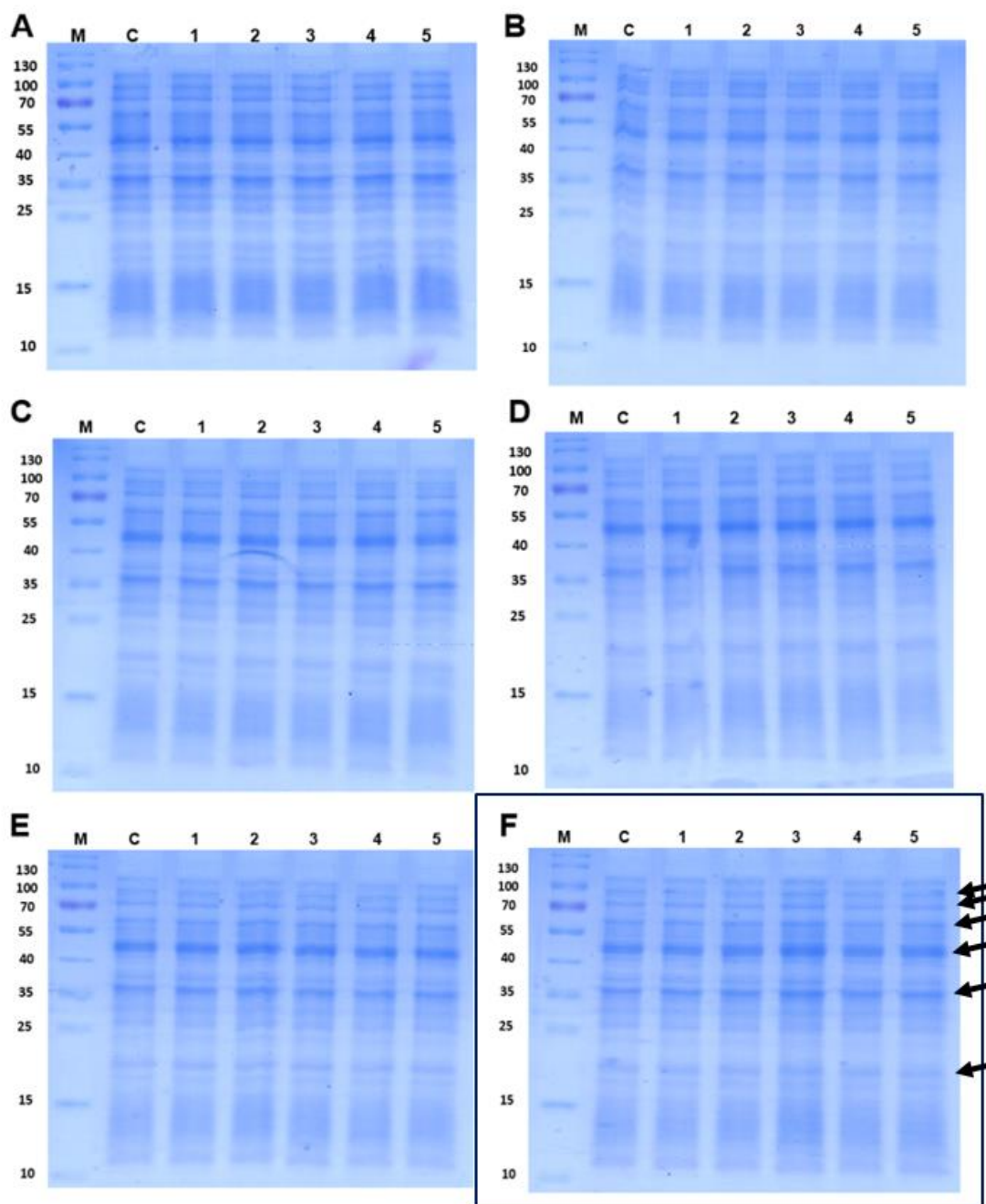


Figure 3.2. Protein expression profiles of *E. coli* O157:H7 cells subjected to varying concentrations of citrate-AuNPs on 10 % SDS PAGE indicated non-toxicity and stable proteome expression. Lane M represents molecular weight marker (PAGE Ruler™ in kDa); Lane C represents control (Cells not exposed to citrate-AuNPs); Lanes 1 – 5 represents proteome expressed after the exposure of cells to varying and increasing concentrations of citrate-AuNPs (2.5, 5.0, 10, 25 µg/ml – 50 µg/ml). (A) Analysis of the proteome expression of *E. coli* O157:H7 after only one hour of incubation at 37 °C. (B) two hours (C) four hours (D) six hours (E) eight hours and (F) twelve hours. Arrows are indicative of sampled bands of proteins twelve hours.

To determine either upregulation or downregulation of certain proteins especially molecular chaperones within *E. coli* cells exposed to varying concentrations of citrate-AuNPs, LC-MS/MS analysis of proteins at five hours was performed. Proteins indicated in arrows were targeted and sampled (Fig. 3.2) for evaluation and analysis with LC-MS/MS and Scaffold software. Quantitative evaluation of total spectra in Scaffold software of the targeted molecular chaperones indicated an increase in the normalized total spectrum (NTS) between control (0 µg/ml citrate-AuNPs) and 2.5 µg/ml citrate-AuNPs ($p < 0.05$). Total proteomic load or expressed proteins in the presence of 50 µg/ml citrate-AuNPs was notably higher than expressed in the absence of citrate-AuNPs ($p < 0.01$). A protein identified as glyceraldehyde-3-phosphate dehydrogenase (GAPDH) was upregulated at normal growth conditions at 37 °C followed by catalytic protease protein X (ClpX) while Survival Protein A (SurA), DnaK, and GroEL were the least upregulated at the same control conditions (Sing *et al.*, 2001; Wu *et al.*, 2012; Table 3.3). Only ClpX and GAPDH were observed to follow a diminishing trend across an increasing concentration of citrate-AuNPs from 54 NTS count down to 50 NTS count with the difference of 1 - 2 NTS counts between each citrate-AuNPs concentration. The latter could suggest that increase in concentration has a detrimental effect on the expression of ClpX and GAPDH. DnaK, GroEL, and SurA were observed to increase with an increase of citrate-AuNPs. The difference in NTS count was observed from 1 – 12 counts with the highest increase being double of the count observed from control. All proteins analyzed had a 100 % identification probability and slightly different spectrum percentage coverages from 0.4 % to 1 % difference. DnaK, GroEL, and SurA are larger than ClpX and GAPDH in molecular weight (Table 3.3). DnaK, GroEL, and SurA are involved in the biogenesis of proteins within *E. coli* cells which might explain their increase in cells exposed to a higher concentration of citrate-AuNPs. Apart from gene regulation and conversion of substrates in metabolic reaction within *E. coli* cells, GAPDH is known to initiate programmed cell death in cells under stress, the downregulation of GAPDH in response to the high concentration of citrate-AuNPs could be a result of survival proteins alleviating cell stress. The Clp class of proteins are ATP-dependent protein unfoldases known to facilitate specific protein degradation (Singh *et al.*, 2001). Similarly, the downregulation of ClpX in response to the high concentration of citrate-AuNPs could be a result of survival proteins alleviating cell stress.

Table 3.3. Molecular chaperones and other proteins identified from the growth of *E. coli* O157:H7 under different concentrations of citrate-AuNPs (0 – 50 µg/ml).

					0 µg/ml citrate-AuNPs		2.5 µg/ml citrate-AuNPs		5 µg/ml citrate-AuNPs		10 µg/ml citrate-AuNPs		25 µg/ml citrate-AuNPs		50 µg/ml citrate-AuNPs	
	Identified Proteins (6/432)	Accession number	Molecular weight (KDa)	Identification Probability (%)	NTS (Quantitative)	Percentage Coverage (%)	NTS (Quantitative)	Percentage Coverage (%)	NTS (Quantitative)	Percentage Coverage (%)	NTS (Quantitative)	Percentage Coverage (%)	NTS (Quantitative)	Percentage Coverage (%)	NTS (Quantitative)	Percentage Coverage (%)
1	DnaK	P0A6Y9.2	69	100	12	26	18	25	18	25	20	26	21	26	24	25
2	GroEL	B7MSV9.1	57	100	28	27	28	39	28	27	30	28	30	30	30	30
3	SurA	Q1RGE4.1	47	100	10	41	10	41	12	40	12	40	12	41	12	41
4	ClpX	A7ZIJ6.1	46	100	52	8	52	8	51	9	50	8	50	8	50	8.4
5	GAPDH	P0A9B4.2	36	100	54	41	52	40	52	40	52	39	52	39	50	34

E. coli O157:H7 cells exposed to varying concentrations of citrate-AuNPs indicated varying outcomes in quantitative NTS analysis. Probability identification was done in mass spectrometry and analyzed by Scaffold software. Statistical significance was determined by using a regression test. Key: NTS – Normalized Total Spectrum; GREEN – Control; RED – Highest Exposure Outcome.

3.3.2. Assessment of the bacterial/AuNPs interaction

The toxic effect of nanoparticles on *Escherichia coli* has been demonstrated before to involve the presence of agglomerating nanoparticles and upregulation of certain molecular chaperones such as GroEL (Makumire *et al.*, 2015). Analysis of changes to cells exposed to citrate-AuNPs with the use of TEM will reveal important information to understand the cell response to citrate-AuNPs (Planchon *et al.*, 2017). Solubility of the proteome of DnaK defective *E. coli* BB1553 cells was performed on lysates harvested at five hours of incubation.

Adaptation to citrate-AuNPs stress may involve upregulation of certain survival proteins including membrane proteins (Makumire *et al.*, 2015; Planchon *et al.*, 2017). TEM analysis (Fig. 3.3F) have revealed changes to the membrane of DnaK defective cells exposed to higher concentrations (50 µg/ml) of citrate-AuNPs. DnaK defective

cells exposed to lower concentrations (2.5 $\mu\text{g/ml}$) of citrate-AuNPs indicated the formation of a bridge-like agglomerated NPs in the middle, while cells were also observed to elongate which could be a response to the presence of citrate-AuNPs. Control cells (Fig. 3.3A Fig. 3.3B) were untreated and as such indicated no changes to the structure. Cells expressing DnaK exposed to higher concentrations of citrate-AuNPs indicated no damage to the cell wall compared to defective DnaK cells which indicated cell wall damage at higher concentrations of citrate-AuNPs (Fig. 3.3E).

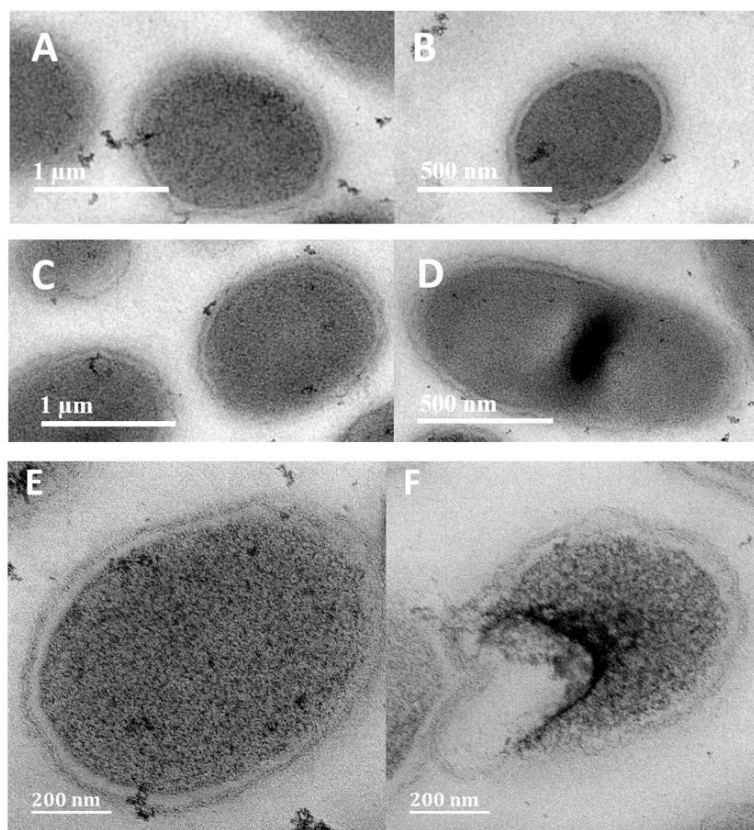


Figure 3.3. TEM images of *E. coli* ΔdnaK52 cells subjected to lower and higher-order citrate-AuNPs concentrations. (A) Untreated *E. coli* ΔdnaK52 cells expressing DnaK, (B) *E. coli* ΔdnaK52 cells untreated, (C) *E. coli* ΔdnaK52 cells expressing DnaK are subjected to 2.5 $\mu\text{g/ml}$ citrate-AuNPs indicating largely intact cell, (D) *E. coli* ΔdnaK52 cells subjected 2.5 $\mu\text{g/ml}$ citrate-AuNPs indicating the formation of a bridge with agglomerated particles and largely intact cell, (E) *E. coli* ΔdnaK52 cells expressing DnaK subjected to 50 $\mu\text{g/ml}$ citrate-AuNPs indicating largely intact cell, (F) *E. coli* ΔdnaK52 cells subjected 50 $\mu\text{g/ml}$ citrate-AuNPs indicating scattered contents of the cell and distorted cell membrane.

3.3.3. The DnaK interactome identified in silver-stained SDS-PAGE

Within *E. coli*, several proteins interact with DnaK, NEFs, ClpB, DnaJ, and GroEL-ES systems to assume a properly folded state and complete their proper function (Ami *et*

al., 2013; Kravats *et al.*, 2016; Wang *et al.*, 2018). In the current study, a co-affinity assay was employed to identify the possible interaction of recombinant *E. coli* DnaK with several other chaperones, co-chaperones, and other role players of the DnaK chaperones system and confirmed with densitometry. The assay was conducted under normal physiological conditions (control) and exposure to varying concentrations of citrate-AuNPs (Fig. 3.4A-B). Exposure to 2.5 µg/ml citrate-AuNPs indicated in the measure of percentage intensity a much higher value than at 50 µg/ml citrate-AuNPs as both were compared to control. The eluate complexes (EC, E1, and E2) from co-affinity assay analyzed using silver stain (Fig. 3.4A) detected protein bands which were analyzed by LC-MS and identified as DnaK, GroEL, ClpB, DnaJ, and SurA.

Since it is the target bait expected to interact with partners from the prey lysate (Mayer and Bukau 2005; Kravats *et al.*, 2016), recombinant DnaK from bait whole lysate was used as a reference (Fig. 3.4B; Fig. 3.4A; Appendix C-6) for quantification of all other bands in percentage intensity, hence given a value of 1 (One) which is converted to 100 % in interpretation (Fig. 3.4B). The amount of bait recovered was detected and quantified at a similar level across concentrations of citrate-AuNPs (Fig. 3.4B; Appendix C-7, C-8). The observed percentage of interacting partners (Fig. 3.4B) in the targeted quantified band(s) recovered with bait DnaK (Appendix C-8) was marginally different between control and at concentrations of 2.5 µg/ml) of citrate-AuNPs ($p < 0.05$). Recovery of DnaK with interacting proteins at higher concentrations (50 µg/ml) of citrate-AuNPs indicated much lower interacting protein partners (Fig. 3.4B). The bands were identified in co-elution with DnaK due to their consistency from the control to the highest concentration of treatment. These were therefore excised and identified with LC-MS /MS (Table 3.4.; Appendix C-5, C-7).

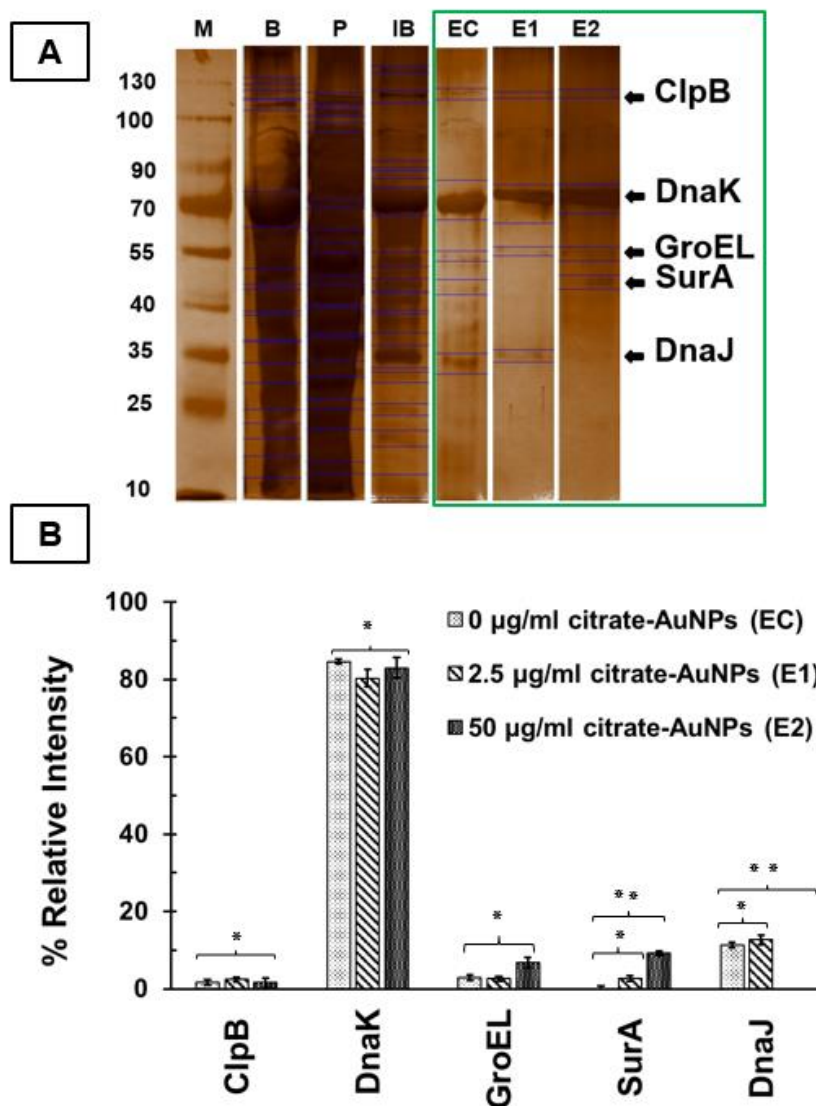


Figure 3.4. The interactome of DnaK was recovered under various concentrations of citrate-AuNPs. (A) An indication of untreated proteins recovered in co-elution with recombinant DnaK in experimental control eluent (EC) experimental eluent 1 and experimental eluent 2 (E2). **(B)** A comparison of the level of proteins co-eluting with recombinant DnaK. Both E1 and E2 indicated binding of certain target proteins to recombinant DnaK herein identified as ClpB, DnaK, GroEL, SurA, and DnaJ as later identified as possible recombinant DnaK interactors by LC-MS/MS. Error bars were generated from three independent experimental values. Statistical significance was determined using regression test. (* $p < 0.05$, ** $p < 0.001$). Key: M – Protein marker, P – Prey lysate, IB – Immobilized bait protein.

The tandem mass spectra were searched and identified by Comet for all samples representing control and varied concentrations of citrate-AuNPs. Preliminary searches without applying stringent cut-offs identified over 600 proteins. Only six out of six hundred and thirty-four proteins were highlighted as molecular chaperones or co-

chaperones of DnaK at 100 % identification probability (Table 3.4). Although DnaK was used as a known bait protein, it was quantified and observed to increase with an increase in citrate-AuNPs from 300 NTS counts in control to 1014 NTS counts in 50 µg/ml citrate-AuNPs. Unique peptides increased by a margin of 4 counts from 2.5 µg/ml citrate-AuNPs to 50 µg/ml citrate-AuNPs ($p < 0.001$) while the count was marginally different from control to 2.5 µg/ml citrate-AuNPs ($p < 0.05$). Changes in bait protein molecule may indicate that the binding of DnaK to citrate-AuNPs was enhanced with the increase in the concentration of citrate-AuNPs. Quantitative evaluation of total spectra and percentage coverage in Scaffold software of the targeted possible interactome of DnaK (Table 3.4) indicated on average a decrease in NTS count in all proteins except for GroEL which notably increased from 28 NTS counts in control to 39 NTS counts in 50 µg/ml citrate-AuNPs ($p < 0.05$). ClpB and HtpG were observed to have higher NTS counts at 2.5 µg/ml citrate-AuNPs than in control ($p < 0.05$) and 50 µg/ml citrate-AuNPs ($p < 0.001$). DnaJ and SurA had the least NTS counts with no count at all in 50 µg/ml citrate-AuNPs, indicating no unique peptides were identified. Identification probability was at 100 % for all proteins identified indicating no count of false discovery for any unique peptides.

Table 3.4. Molecular chaperones identified from the co-elution fractions of recombinant DnaK lysates exposed to varying concentrations of citrate-AuNPs.

			0 µg/ml citrate-AuNPs				2.5 µg/ml citrate-AuNPs				50 µg/ml citrate-AuNPs				
Identified Proteins (6/634)	Accession number	Molecular weight	Identification Probability (%)	Percentage Coverage	NTS (Quantitative)	Exclusive Unique Peptide	Identification Probability (%)	Percentage Coverage	NTS (Quantitative)	Exclusive Unique Peptide	Identification Probability (%)	Percentage Coverage	NTS (Quantitative)	Exclusive Unique Peptide	
1	DnaK	P0A6Y9.2	69 kDa	100	26	390	247	100	19	400	247	100	87	1014	251
2	GroEL	B7MSV9.1	57 kDa	100	27	28	14	100	34	32	16	100	27	39	17
3	ClpB	P63285.1	96 kDa	100	12	10	7	100	9.5	21	10	100	14	20	11
4	HtpG	B11ZC1.1	71 kDa	100	5	19	3	100	25	25	13	100	25	21	11
5	DnaJ	B1XBE0.1	41 kDa	100	30	35	11	100	29	3	1	100	0	0	0
6	SurA	Q1RGE4.1	47 kDa	100	26	9	1	100	7.7	0	0	100	0	0	0

* Probability identification was done in mass spectrometry and analysed by Scaffold Q+ software. Statistical significance was determined by using a regression test. Key: NTS – Normalized Total Spectrum (Bold).

Proteins with spectral counts less than 5 were filtered and the rest were subjected to reproducibility testing, whereby 0 µg/ml citrate-AuNPs (control), 2.5 µg/ml citrate-AuNPs and 50 µg/ml citrate-AuNPs are compared in a Venn diagram for the identified unique peptides (Fig. 3.5). Further, a comparison of the unique peptides count per protein may indicate the best discovery rate for each protein. For DnaK, GroEL, HtpG, and ClpB peptides were fairly distributed between 4 – 13 counts in each overlap but the same did not apply for SurA. Although at much less count of unique peptides, DnaJ indicated a fair distribution in all concentrations of citrate-AuNPs (Fig. 3.5).

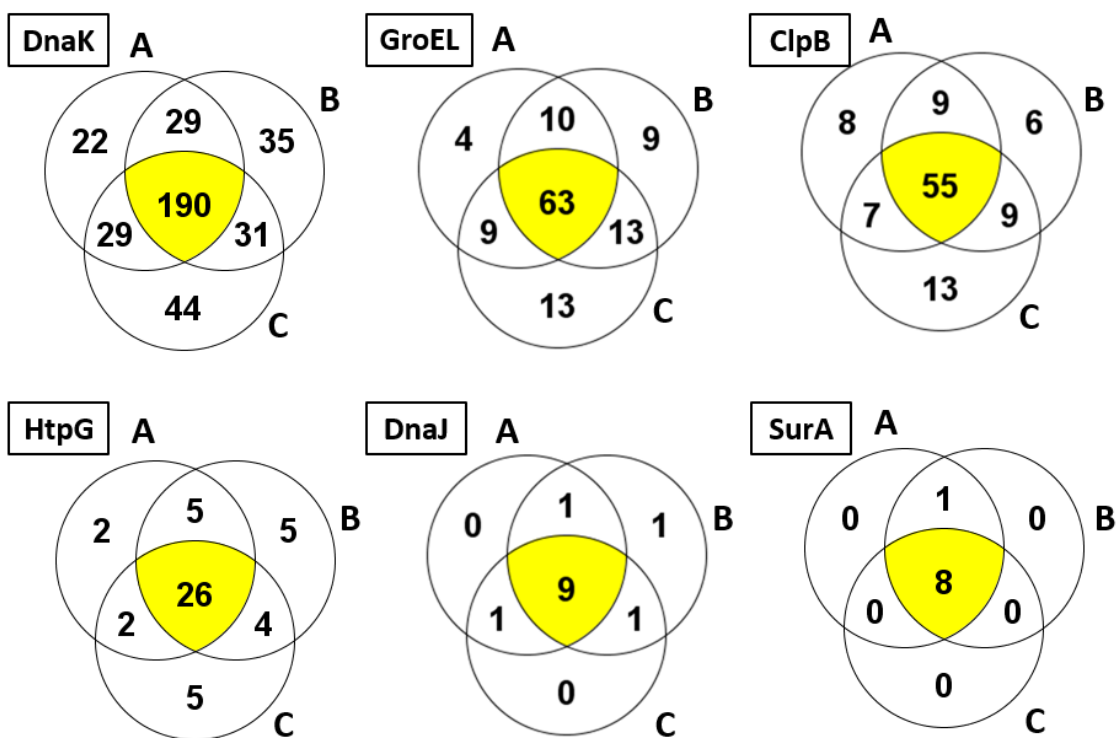


Figure 3.5. Proportional Venn diagram demonstrating the overlap of unique peptides of each interactome of DnaK. Unique peptides representing each heat shock protein involved in the alleviation of citrate-AuNPs induced stress were identified from the interactome of DnaK exposed to each concentration of citrate-AuNPs (A – C) and analysed by Scaffold Q+ software. **A**, 0 µg/ml citrate-AuNPs; **B**, 2.5 µg/ml citrate-AuNPs; **C**, 50 µg/ml citrate-AuNPs.

3.4. DISCUSSION

There are many features by which a protein can be described and identified. These include expression, localization, interaction, domain structure, modification, and protein activity. Although proteomic constituents may change even in the slightest change of cellular environment and stress, a degree of proteomic stability is important for the survival of the cells. This study mainly investigated the proteomic changes on *E. coli* cells and proteins due to the presence of citrate-AuNPs by way of identifying and quantifying select proteins by LC-MS/MS.

The presence of varying citrate-AuNPs concentrations exposed to *E. coli* would have generated distinct proteomic profiles. The growth rate indicated a certain degree of difference in the growth pattern of the control from those of the experimental, similarly, the proteomic constituents also indicated changes across varying concentrations of

citrate-AuNPs as analyzed by LC-MS/MS. There was no obvious identification of upregulation or downregulation of proteins observed in SDS-PAGE across either time of incubation or varying concentrations of citrate-AuNPs, therefore proteins which indicated different expression level from control were targeted for an LC-MS/MS quantitatively and compared across concentrations of citrate-AuNPs by NTS count and identified unique peptides. Decreasing NTS counts indicated the downregulation of proteins in response to the higher concentration of citrate-AuNPs, a phenomenon previously reported for DnaK, GroEL and SurA in response to heat stress (Kityk *et al.*, 2015; Wang *et al.*, 2018; Humes *et al.*, 2019). Apart from the soluble DnaK and GroEL chaperones which had an increase of NTS count with increasing citrate-AuNPs concentration, a survival chaperone protein (SurA) responsible for the correct folding and assembly of outer membrane proteins was identified and noted to have diminished with increasing citrate-AuNPs. Diminishing SurA protein may explain the damage on the *E. coli* cell wall exposed to higher concentrations of citrate-AuNPs. The absence of SurA as a membrane protein would result in a compromised cell wall. DnaK is known to play a vital role in the protection of cells against stress, SurA is known to play a vital role in membrane assembly in stable conditions, it can therefore be postulated that DnaK may interact with SurA to aid protection to the *E. coli* cell under stress although such claim remains to be investigated. The presence of SurA as part of the interactome confirms its role as a molecular chaperone. Another protein highly expressed was the NAD-dependent glyceraldehyde-3-phosphate dehydrogenase (GAPDH) at 36 kDa. GAPDH is a known housekeeping protein important for the glycolysis pathway, but most importantly for the gene regulation and metabolic function, it performs in different cellular compartments (Henderson *et al.*, 2014). It has also been noted to be secreted by enteropathogenic *E. coli* strains such as O157:H7 leading to its involvement in pathogenesis in humans and animals (Egea *et al.*, 2007). Being a substrate of DnaK, GAPDH is rescued by DnaK in an ATP-dependent manner (Liu *et al.*, 2005). Therefore, the presence of GAPDH in large quantities could talk to the much less quantity of DnaK and DnaJ during *E. coli* cell growth under normal conditions. The presence of diminishing ClpX could not be linked to citrate-AuNPs but merely to its role in cell division.

TEM analysis implicated the presence of heterologously expressed DnaK in the survival of cells in the presence of citrate-AuNPs in that the cells without functional DnaK could hardly stay intact in the presence of particles. The observation was that the cells with functional DnaK survived damage during the internalization of particles (Makumire *et al.*, 2015). This then validates that wild-type *E. coli* cells have a natural cytoprotection against citrate-AuNPs stressors, which then links to the stability of *E. coli* O157:H7 proteomic profiles across particle concentrations.

The identification of proteins recovered with recombinant DnaK indicated that certain interaction partners bind to DnaK depending on the concentration of citrate-AuNPs. It could either be that proteins were binding to particles and therefore unable to bind to DnaK or vice versa. A much less number of proteins (Fig. 3.4A) were measured by densitometric analysis as compared to the rest (Fig. 3.4B, C) indicating lower and higher concentrations of citrate-AuNPs with much higher sensitivity in densitometric quantification. The LC-MS/MS analysis of excised bands indicated several molecular chaperones amongst the many identified proteins (Appendix C-5). There are few chaperones of interest due to their supposed functional interaction with DnaK in the alleviation of citrate-AuNPs stress. SurA chaperone protein was highly expressed but similarly distributed in wild-type *E. coli* O157:H7 exposed to particles in the previous section. Although SurA is a survival protein, it is highly unlikely that it functions alongside DnaK to alleviate stress. In quantification, it completely diminished with the introduction of concentrations of citrate-AuNPs. Almost similar behaviour is observed with co-chaperone DnaJ which is also seen to diminish. ClpB, HtpG, and GroEL were identified and quantified to be much more consistent across the concentrations of particles. These proteins are known to interact with DnaK during proteostasis in *E. coli* cells. It is therefore possible that these proteins remain stable in the presence of citrate-AuNPs to carry on with their chaperone function unabated. The identification of proteins whose expression level was altered by citrate-AuNPs treatment using LC-MS/MS indicated that proteins respond differently to interacting with DnaK after exposure to citrate-AuNPs.

CHAPTER 4

4. Biophysical and Biochemical Characterization of Recombinant DnaK subjected to citrate-AuNPs

4.1. INTRODUCTION

Although DnaK may function alongside DnaJ, the full chaperone machine includes GrpE with DnaK and DnaJ (Nunes *et al.*, 2015; Mayer *et al.*, 2015). DnaK as an Hsp70 is divided into two major domains, NBD which is a 45 kDa N-terminal binding domain that exhibits ATPase activity and SBD which is a 25 kDa peptide binding domain. There is also a short C-terminal domain which is largely known to function by interacting with partner proteins (Mayer and Bukau, 2005). An ATP-bound DnaK exhibits a low affinity for its substrates (De Los Rios and Barducci, 2014). DnaK is regulated by co-chaperones to prevent uncontrolled cycling of random substrates (Laufen *et al.*, 1999). An important co-chaperone to DnaK in ATP hydrolysis contributing to the survival of the cell is DnaJ, it synergizes with DnaK to assist in the folding of proteins (Nunes *et al.*, 2015; Kityk *et al.*, 2015). It is generally believed that the conformational changes of protein alter the function of the protein, hence when DnaK is in an ATP-bound state is reported to be in an open conformation (Kityk *et al.*, 2012). During the ongoing conformational changes process, some amino acids tend to assume a defect mode which may lead to protein dysfunction (Kityk *et al.*, 2012). There have been reports of an interaction between proteins and bivalent transition metal ions (Parveen *et al.*, 2016; Chakraborty *et al.*, 2018). Such interaction may regulate the structure and chaperone function of the protein (Yang *et al.*, 2008). The interaction of citrate-AuNPs with DnaK and the impact of such interaction on its secondary and tertiary structure and chaperone function is not yet known. Due to their high area to size ratio, AuNPs have an advantage over bulk gold metal material when it comes to binding proteins (Gagner *et al.*, 2013). In the current study, an investigation was done to gain an insight into the possible interaction of citrate-AuNPs with DnaK. Subsequently, the impact of the supposed interactions is investigated on the structure and chaperone function of *E. coli* DnaK.

4.1.1. Specific Objectives

4.1.1.1. To investigate the effect of citrate-AuNPs on ATPase activity of recombinant DnaK aided by co-chaperone DnaJ

4.1.1.2. To investigate the effect of citrate-AuNPs on the ability of recombinant DnaK to suppress aggregation of MDH enzyme *in vitro*

4.1.1.3. To investigate the effect of citrate-AuNPs on the secondary and tertiary structure of DnaK by CD spectroscopy and fluorescence spectroscopy

4.2. EXPERIMENTAL PROCEDURES

4.2.1. Materials

The list of reagents used in this study is presented in Appendix D-16. The following antibodies were used for protein validation by Western blotting (Appendix D-5, D-6) rabbit raised α -DnaJ antibody and horseradish peroxidase (HRP) conjugated α -rabbit (Zininga *et al.*, 2015a), mouse raised α -DnaK antibody (Sigma-Aldrich, U.S.A), HRP conjugated α -mouse secondary antibodies (Sigma-Aldrich, U.S.A) and an HRP-conjugated α -His antibody (Sigma-Aldrich, U.S.A). The plasmid constructs and bacterial strains used for confirmation of constructs and recombinant protein production are listed (Table 4.1).

Table 4.1. List of plasmids and *E. coli* strains used for protein expression and purification

Construct	Description	Supplier/Reference
pQE30/DnaJ	pQE30 encoding DnaJ, Ampicillin resistant	Makhoba <i>et al.</i> , 2016
pQE30/DnaK	pQE30 encoding <i>E. coli</i> DnaK, Ampicillin resistant	Makhoba <i>et al.</i> , 2016
<i>E. coli</i> strains (Protein Expression and Purification)		
<i>E. coli</i> XL1 Blue	<i>recA1 endA1 gyrA96 thi1 hsdR17 supE44 relA1 lac</i> (<i>F'proAB lacIqZM15 Tn10 (Tetr)</i>)	ThermoFischer Scientific, USA
<i>E. coli</i> JM109	<i>e14- (McrA-) recA1 endA1 gyrA96 thi-1 hsdR17 (rK - mK +) supE44 relA1 Δ(lac-proAB) (F' traD36 proAB lacIq ZΔM15)</i>	Promega Scientific, USA

4.2.2. Expression and purification of DnaK and DnaJ from *E. coli* XL1 Blue strain

Plasmid constructs (*pQE30/dnaJ* and *pQE30/dnaK*) were transformed (Appendix D-1) and confirmed by restriction analysis (Appendix D-2, D-3). The restriction fragments were resolved on 0.8 % agarose gel electrophoresis (Appendix D-4). The recombinant proteins were expressed in *E. coli* XL1 Blue cells (ThermoFisher Scientific, USA) after chemically competent *E. coli* XL1 Blue cells were transformed with respective constructs coding for DnaJ and DnaK. For the production of both DnaK and DnaJ, protein expression was conducted as previously described by Zininga *et al.*, 2015a. Briefly, transformed cells were grown in 2 x YT broth (Yeast extract, 1.0 %; Tryptone, 1.6 % and 0.5 % NaCl) supplemented with 100 µg/ml ampicillin at 37 °C. Induction of protein expression was initiated by the addition of 1 mM isopropyl β-d-1-thiogalactopyranoside (IPTG). Expression of proteins was allowed for 5 hrs during which samples were collected at 1 hr intervals for SDS-PAGE (Appendix C-1) analysis before protein purification. Proteins were purified using HisPur™ Ni-NTA (Thermo Scientific, USA) affinity chromatography as previously described (Zininga *et al.*, 2015a). Purified proteins were dialyzed and stored in dialysis buffer (20 mM Tris-HCl, pH 7.5, 100 mM NaCl, 5 % (v/v) glycerol, containing 1 mM 2-β-mercaptoethanol and 1 mM PMSF; Appendix D-8) using 30 KDa Amicon® centrifugal filter units per manufacturer's protocol (Merck, USA).

4.2.3. Investigation of the effect of citrate-AuNPs on ATPase activity of recombinant DnaK aided by co-chaperone DnaJ *in vitro*

The ATPase activity of DnaK together with DnaJ was measured based on the amount of released inorganic phosphate (*P_i*), the ATPase activity of DnaK aided by DnaJ and citrate-AuNPs was determined by performing a colorimetric ATPase activity assay as previously described with modifications (Palleros *et al.*, 1993; Mabate *et al.*, 2018). Initially, 2.5 µM DnaK, 1 µM DnaJ, 1 µM BSA were each and in combination incubated for 5 hour in ATPase buffer (10 mM HEPES-KOH pH 7.5, 100 mM KCl, 2 mM MgCl₂, 0.5 mM DTT) with 0 – 1.5 mM ATP concentrations and citrate-AuNPs. Boiled samples of each protein were used as control and to monitor spontaneous hydrolysis of ATP. Three independent assay runs were conducted for each recorded outcome per protein

with citrate-AuNPs. To determine kinetics for the ATPase activity of the batch of proteins with citrate-AuNPs, Michaelis-Menten plots were generated using GraphPad Prism 6.05.

4.2.4. Investigation of the effect of citrate-AuNPs on the ability of DnaK aided by co-chaperone DnaJ to suppress aggregation of MDH enzyme *in vitro*

The main objective was to investigate the effect of citrate gold nanoparticles on the structure and functionality of proteins. The assay was conducted as previously described (Makumire *et al.*, 2015; Chakraborty *et al.*, 2018) in the presence and absence of citrate-AuNPs. Briefly, 1 μM of porcine heart MDH (Sigma-Aldrich-Roche, Darmstadt, German) was suspended in an MDH assay buffer (20 mM Tris, pH 7.4; 100 mM NaCl). Citrate-AuNPs were added to each reaction mix to final concentrations ranging from 0 – 100 $\mu\text{g}/\text{mL}$. As a positive control, 2 μM of DnaK (Shonhai *et al.*, 2008) was included in place of citrate-AuNPs. Citrate-AuNPs, DnaJ, and DnaK were added to separate reactions. The solutions were set in triplicate and incubated at 51 $^{\circ}\text{C}$ for 30 minutes. BSA was used as control. Protein aggregation was monitored based on the development of turbidity spectrophotometrically at 360 nm. Optical density (OD) readings were taken every 2 mins at 360 nm using a SpectraMax M3 spectrometer (Molecular Devices, USA). The resultant absorbance units were then converted to aggregation percentages relative to the aggregation level of MDH (set at 100 %) and data was analyzed using GraphPad Prism 6.05 software (San Diego, USA).

4.2.5. Investigation of the effect of citrate-AuNPs on the secondary and tertiary structure of DnaK by circular dichroism spectroscopy and fluorescence spectroscopy

Proteins have been reported to change structural conformation and function in response to metallic NPs binding (Nandi *et al.*, 2018; Chakraborty and Biswas, 2020). Fluorescence spectroscopic analysis and circular dichroism were used to determine citrate-AuNPs protein binding dependent conformational changes to DnaK. The secondary structure of DnaK was determined using far-UV circular dichroism (CD) spectroscopy. The relative secondary structures and thermal stability of the DnaK were also determined following a previously described method (Achilonu *et al.*, 2014;

Chakraborty and Biswas, 2020) using a JASCO far-UV J-1500 CD spectrometer (JASCO Ltd, UK) equipped with a Peltier temperature control system. Briefly, Spectra measurements were recorded at 100 nm/min scan speed, 1 nm bandwidth and averaged for 5 accumulations after subtraction of assay buffer (10 mM Tris buffer pH 7.4) baseline measurement. The protein concentration (Appendix D-7) used for all the measurements was kept at 1 μ M DnaK in assay buffer pre-incubated at room temperature for 60 minutes. Data deconvolutions of derived spectra to determine changes in α -helix, β -sheet, β -turn, and unordered regions in DnaK were performed on the Dichroweb server (<http://dichroweb.cryst.bbk.ac.uk>) (Lobley *et al.*, 2002). The relative stability of DnaK in the presence of thermal and chaotropic denaturants was compared to that of the same protein in the presence of citrate-AuNPs in analysis. Comparative thermal melts in the presence and absence of citrate-AuNPs were determined by subjecting the proteins to monotonical temperature increments at a rate of 0.5 $^{\circ}$ C per minute from 20 $^{\circ}$ C – 90 $^{\circ}$ C and spectra measurements were recorded at a fixed wavelength of 222 nm as previously described (Nandi *et al.*, 2018; Chakraborty and Biswas, 2020). The folded state of DnaK was monitored by assessing the molar residue ellipticity (MRE) at 222 nm (Appendix D-9) in the presence of varying concentrations (0 – 100 μ g/ml) of citrate-AuNPs. The folded state of the proteins exposed to various urea levels was then calculated as previously described (Zininga *et al.*, 2015b).

Proteins in assay buffer (20 mM Tris, pH 7.4; 100 mM NaCl, pH 7.4) were added to a volume of citrate-AuNPs solution to a determined final concentration. The mixture was equilibrated with shaking at 26 $^{\circ}$ C for 60 minutes. The tertiary structure of DnaK was analyzed using intrinsic fluorescence spectroscopic analysis. Tryptophan/tyrosine fluorescence spectroscopic assays were conducted to monitor changes in the structure of DnaK in response to the presence of citrate-AuNPs, as previously described (Chakraborty and Biswas, 2020) with minor modifications. The generated fluorescence spectra were analyzed after excitation at 280 nm using a JASCO FP-6300 spectrofluorometer (JASCO International CO., Ltd, UK). The emission spectra were monitored between 280 to 450 nm with the excitation wavelength of 280 nm at a scan speed of 500 nm/min. Briefly, DnaK was incubated in assay buffer (20 mM Tris, pH 7.4; 100 mM NaCl, pH 7.4) for 30 minutes at room temperature in the presence of

varying concentrations of citrate-AuNPs (0 – 50 µg/ml) before spectral measurements were taken. Varying concentrations of chaotropic denaturant urea were used in the place of citrate-AuNPs to determine the effect of positive control in inducing a red or blue shift conformational changes of the tertiary structure of DnaK (Eftink, 1991). Spectra used for baseline subtraction and negative controls were taken from readings of the buffers with citrate-AuNPs (0 – 50 µg/ml).

4.3. RESULTS

4.3.1. Citrate-AuNPs regulate the ATPase activity of recombinant DnaK aided by its co-chaperone DnaJ *in vitro*

The pQE30/*dnaK* and pQE30/*dnaJ* constructs used in the expression of proteins were verified by restriction digestion with *BamHI*, *HindIII*, and *BamHI*, *PstI* restriction enzymes respectively (Appendix D-3 and Appendix D-4). Recombinant DnaK and DnaJ were successfully expressed and purified as observed with the use of SDS PAGE and Western blot analysis (Appendix D-11, D-12).

ATPase activity assays were conducted to investigate the effect of the presence of citrate-AuNPs on the hydrolysis of ATP by DnaK and DnaJ. DnaK exhibited V_{\max} and K_m values of 24 nmol/min/mg, 85 µM (0.085 mg) while in combination with DnaJ, DnaK exhibited V_{\max} and K_m values of 32 nmol/min/mg and 226 µM (0.266 mg) respectively (Table 4.1; Fig 4.1). Combination of DnaK and DnaJ required higher concentrations of ATP to achieve less than double the V_{\max} of DnaK alone. These findings were comparable to those observed in a previous study (Lieberk *et al.*, 1991).

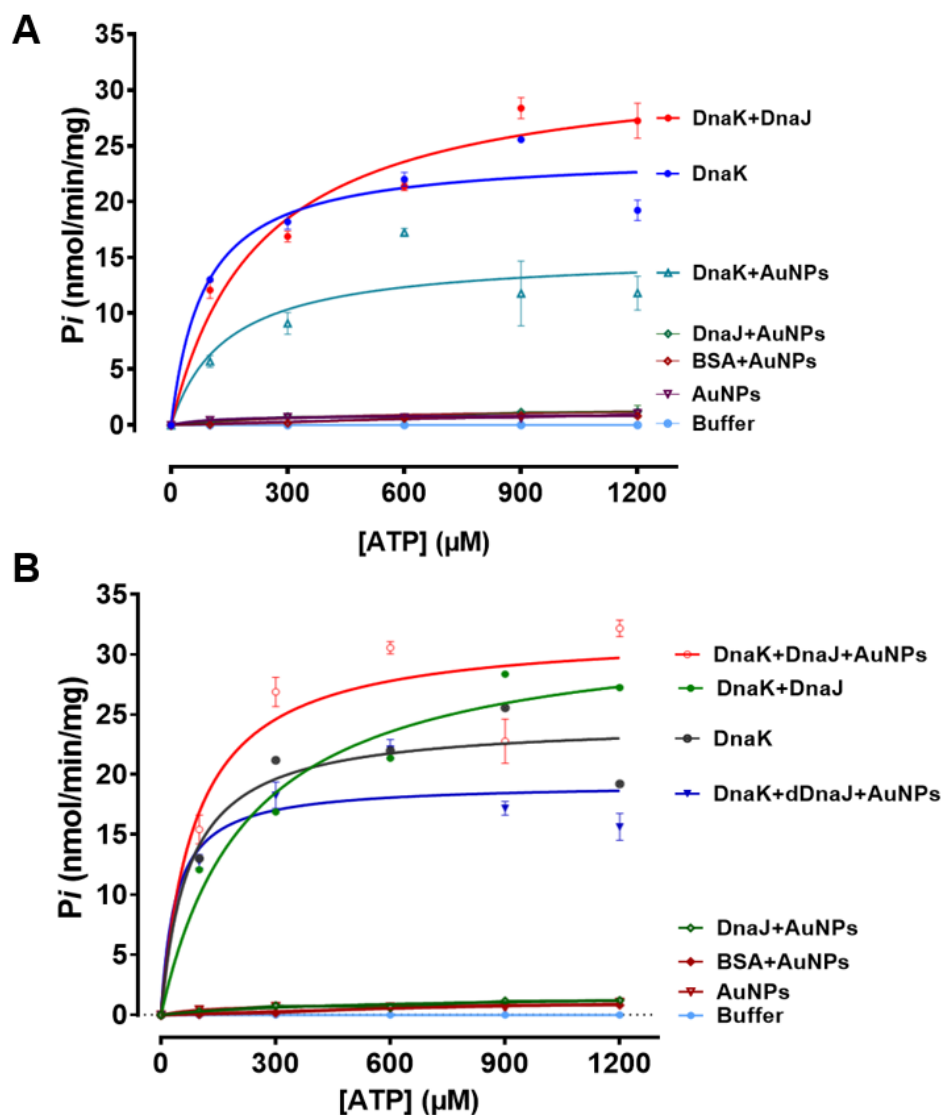


Figure 4.1 Citrate-AuNPs regulate ATPase activity of recombinant DnaK. (A) The ATPase activity of DnaK with DnaJ agrees with previous studies indicating cooperativity. All controls had a baseline subtraction of buffer. (B) ATPase activity of DnaK with DnaJ and 2.5 μg/ml citrate-AuNPs exhibited the highest catalysis. ATPase activity rates were calculated and reported based on catalytic efficiency (Table 4.2, Fig. 4.2). The assay was carried out in triplicates. At least three independent assays were conducted using independently purified protein each time.

Several ATPase assays conducted in this study validated that indeed DnaJ protein (Appendix D-7) stimulated ATPase activity of DnaK. ATPase activities of DnaK with DnaJ (Fig 4.1A) became the basis for the evaluation of the activities of the same molecular chaperones in the presence of varying concentrations of citrate-AuNPs (Appendix D-14). Citrate-AuNPs were validated and found stable in assay buffer before use (Appendix D-13). It was observed that lower-order concentrations (2.5

$\mu\text{g/ml}$) of citrate-AuNPs altered and abrogated the basal ATPase activity of DnaK measure in catalytic efficiency from $1.9 \times 10^{-04} \text{ sec/mol}^{-1}$ to $4.2 \times 10^{-07} \text{ sec/mol}^{-1}$ (Table 4.2; Fig 4.1A), while higher-order ($50 \mu\text{g/ml}$) citrate-AuNPs had abrogated the ATPase activity of the chaperones from $1.9 \times 10^{-04} \text{ sec/mol}^{-1}$ to $2.1 \times 10^{-30} \text{ sec/mol}^{-1}$. DnaK with citrate-AuNPs had a catalytic efficiency of $3.2 \times 10^{-30} \text{ sec/mol}^{-1}$ while that of DnaK with DnaJ and citrate-AuNPs was $2.1 \times 10^{-30} \text{ sec/mol}^{-1}$. The catalytic efficiency of DnaK+DnaJ+ $2.5 \mu\text{g/ml}$ citrate-AuNPs ($p < 0.001$) (Fig 4.2; Table 4.2) was increased by more than half in comparison with that of DnaK (Fig 4.1; Table 4.2).

Table 4.1 Michaelis-Menten kinetics for DnaK+DnaJ+citrate-AuNPs

	Vmax (nmol/min/mg)	Km (μM)	Kcat (mol^{-1})	Catalytic efficiency (sec/mol^{-1})
Buffer	1.69E+12	2.05E+27	ND	ND
DnaK	24.250	85.060	1.617	1.901E-04
DnaK+DnaJ	32.490	226.500	0.928	4.098E-04
DnaK+AuNPs (2.5 $\mu\text{g/ml}$)	15.290	142.900	0.612	4.280E-07
DnaK+DnaJ+AuNPs (2.5 $\mu\text{g/ml}$)	31.930	89.140	0.912	1.023E-03
DnaK+Boiled DnaJ+AuNPs (2.5 $\mu\text{g/ml}$)	19.260	38.960	0.550	1.412E-05
DnaK+AuNPs (50 $\mu\text{g/ml}$)	1.95E+02	2.37E+27	7.796	3.287E-30
DnaK+DnaJ+AuNPs (50 $\mu\text{g/ml}$)	3.82E+02	5.05E+27	10.920	2.161E-30
DnaK+Boiled DnaJ+AuNPs (50 $\mu\text{g/ml}$)	2.33E+02	3.33E+27	6.660	1.999E-30

ND –Not Determined

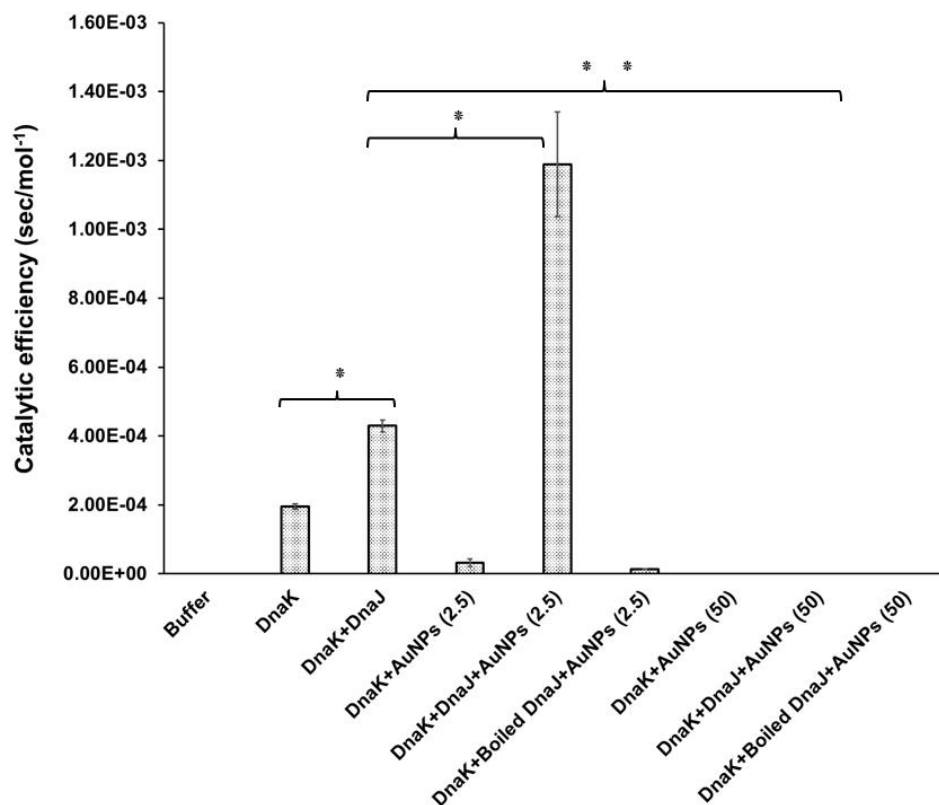


Figure 4.2 The combination with DnaJ and 2.5 $\mu\text{g/ml}$ citrate-AuNPs increases the ATPase catalytic efficiency of recombinant DnaK. Catalytic efficiency ($\text{sec}\cdot\text{mol}^{-1}$) of DnaK, DnaK with co-chaperone DnaJ and DnaK with citrate-AuNPs were calculated based on Michaelis-Menten turnover number per concentration of substrate at half maximum velocity (Table 4.2). Error bars were generated from data obtained from independent catalytic efficiency of DnaK analysis. Statistical significance was determined using regression test. (* $p < 0.01$, ** $p < 0.001$).

4.3.2. Citrate-AuNPs influences the ability of DnaK and co-chaperone DnaJ to suppress aggregation of MDH enzyme *in vitro*

Malate dehydrogenase (MDH) has been extensively used as an aggregation-prone protein to demonstrate the aggregation suppression capabilities of DnaK and other molecular chaperones in the Hsp70 family. Molecular chaperone DnaK was previously observed to be thermally stable at as high as 48 °C (Makumire *et al.*, 2015; Mabate *et al.*, 2018), therefore it would be an efficient aggregation suppressant chaperone. Citrate-AuNPs were also assessed for thermal stability at 48 °C and observed to be stable (Appendix D-15). MDH aggregated in response to heat stress at 48 °C was used as a control and reference percentage to which other aggregation measurements

were then calculated (Fig 4.3). BSA was used as an additional control to validate that aggregation suppression of MDH quantified at any given time would be due to the presence of molecular chaperone DnaK or DnaJ (Fig 4.3A). To further validate the chaperone action of either DnaK, DnaJ, or a combination of DnaK and DnaJ (DnaKJ) in the current study, an investigation to reverse the heat-induced aggregation of MDH was successful in the presence of DnaK and measure at 69 % aggregation suppression, while that of DnaJ only yielded a 2 % aggregation suppression. However, a combination of DnaK and DnaJ yielded 79 % aggregation suppression which is 10 % higher than that of DnaK on its own (Fig 4.3B-D).

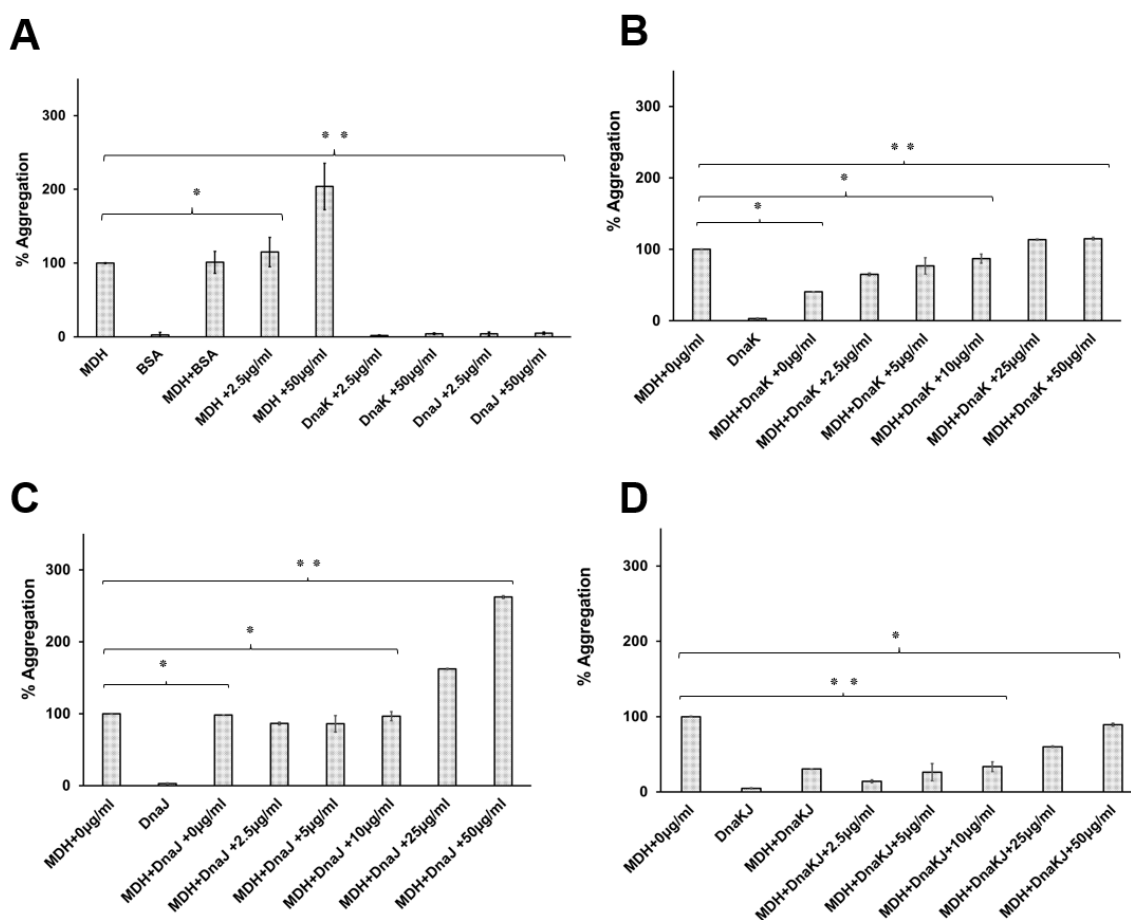


Figure 4.3. Citrate-AuNPs increases the efficiency of DnaK and DnaJ chaperone functional association in vitro. Heat-induced aggregation of MDH was investigated at 48 °C. The capability of DnaK and DnaJ and that of the combination of DnaK and DnaJ to suppress MDH aggregation was reported. The assay was performed in the absence and presence of 0 – 50 µg/ml citrate-AuNPs. Error bars were generated from data obtained from independent proteins preparation. Statistical significance was determined using one-way ANOVA test. (* $p < 0.01$, ** $p < 0.001$).

It was generally observed that DnaK together with co-chaperone DnaJ exhibited elevated capabilities of suppressing the aggregation of MDH in the presence of 2.5 µg/ml citrate-AuNPs as compared to when DnaK and DnaJ function invitro to suppress the aggregation of MDH (Fig 4.3A-D). DnaK individually suppressed the aggregation of MDH, it was however not significantly aided by citrate-AuNPs in its function. When DnaJ was tested, the presence of either lower end (2.5 µg/ml) or higher end (50 µg/ml) citrate-AuNPs significantly increased the aggregation of MDH beyond 100 %. Both chaperones DnaK and DnaJ were thermally stable in MDH buffer at high temperatures and so were both lower order and high order citrate-AuNPs individually.

4.3.3. Citrate-AuNPs do not affect the secondary and tertiary structure of DnaK

The effect of citrate-AuNPs and heat stress on the secondary structure of DnaK was investigated by conducting circular dichroism (CD) spectrophotometric analysis. The purified recombinant DnaK (Appendix D-12) was pre-incubated at 26 °C for 60 minutes. The secondary structure of DnaK was initially determined by far-UV CD spectroscopy before performing modifications to the assay (Mabate *et al.*, 2018). *E. coli* DnaK (P0A6Y8) is predominantly alpha helical (α -helical) as observed in prior *in silico* predictions using obtained sequence from UniProtKB database (<https://www.uniprot.org/uniprot/P0A6Y8>). The respective CD spectra are characterized by a peak at approximately 195 nm as well as troughs at approximately 208 nm and 220 nm, respectively (Fig 4.5). As such, deconvolutions of the structures of DnaK using Dichroweb online tools confirmed that DnaK is α -helical (Fig 4.5A; Table 4.3). All the structural values derived upon deconvolution were quality checked with RMSD values less than 1 which indicated the confidence in data reliability (Table 4.3). There were no significant differences observed between the secondary structures analyzed between DnaK with or without citrate-AuNPs concentrations (0 – 50 µg/ml) and DnaK as a control (Fig 4.5 B1 – B3) (Table 4.3; $p > 0.01$). It was generally observed that the secondary structure of DnaK was not perturbed by the presence of any concentration of citrate-AuNPs (0 – 50 µg/ml). Although a study done on Hsp18 which is a small chaperone indicated perturbation in the structure of the protein

(Chakraborty and Biswas, 2020), the current study on Hsp70 (DnaK) which is a larger chaperone indicated little or no perturbation (Fig 4.4).

Recombinant DnaK exhibited thermal tolerance up to temperatures approximating 45 °C where molar ellipticity monitored at 220 nm was observed to indicate loss of alpha-helical residues (Fig 4.4). The folded fraction assessment of recombinant DnaK protein showed that more than 60 % of the protein maintained its folded state at 48 °C (Fig. 4.4A). Both DnaK and DnaK in the presence of lower order AuNPs (2.5 µg/ml) were observed to retain or recover twice as many residues as compared to DnaK in the presence of higher-order citrate-AuNPs (50 µg/ml) (Fig 4.4 B1 – B3).

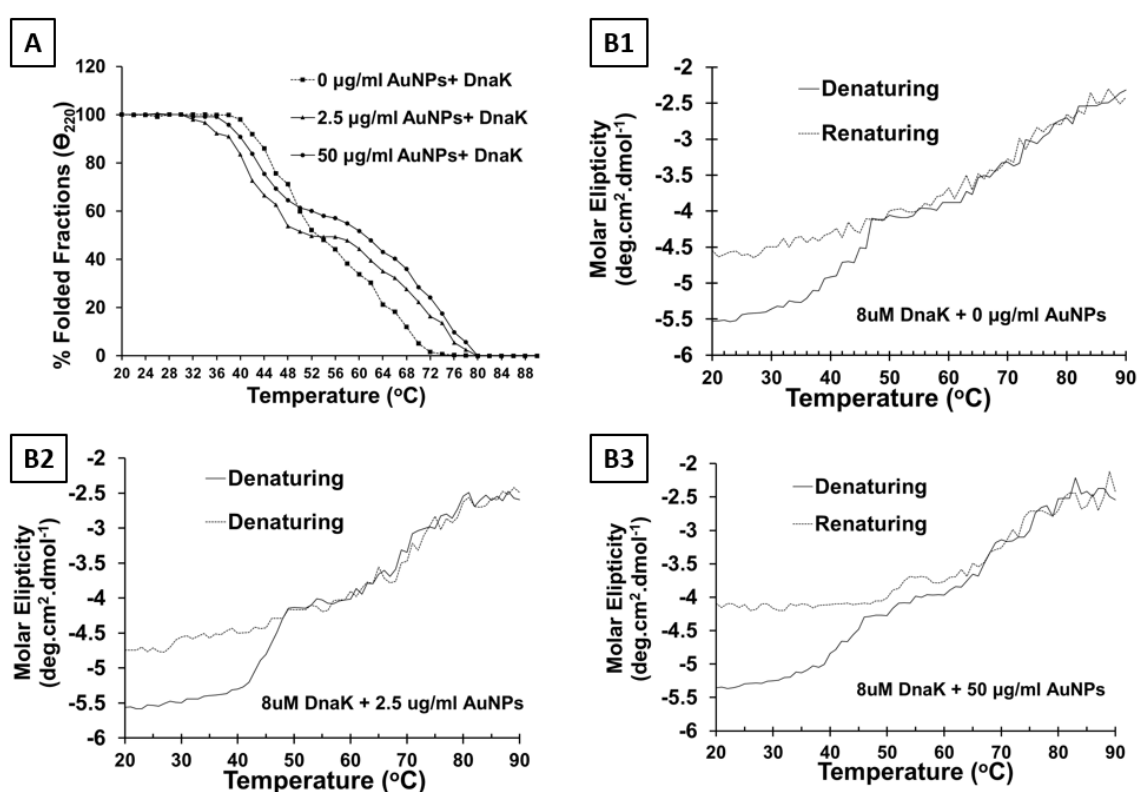


Figure 4.4. Lower order citrate-AuNPs enhances the stability of the secondary structure of DnaK at higher temperatures than normal functional levels. The secondary structural analysis of DnaK, (A) at room temperature in the absence and presence of lower and higher order citrate-AuNPs concentration, (B1) before denaturation and after renaturation, (B2) exposed to 2.5 µg/ml citrate-AuNPs then denatured and subsequently renatured, (B3) exposed to 50 µg/ml citrate-AuNPs then denatured and subsequently renatured. All calculations emanated from the Dichroweb tool and IBM statistical software.

To validate the recovery of residues after renaturation, a full secondary structural analysis was conducted and compared before and after exposing DnaK to increasing and decreasing temperatures in the presence of citrate-AuNPs. Similarly, the lower order citrate-AuNPs concentration was observed to effectively maintain the alpha-helical content of the protein at $\theta = 220\text{nm}$ (Fig 4.5 A).

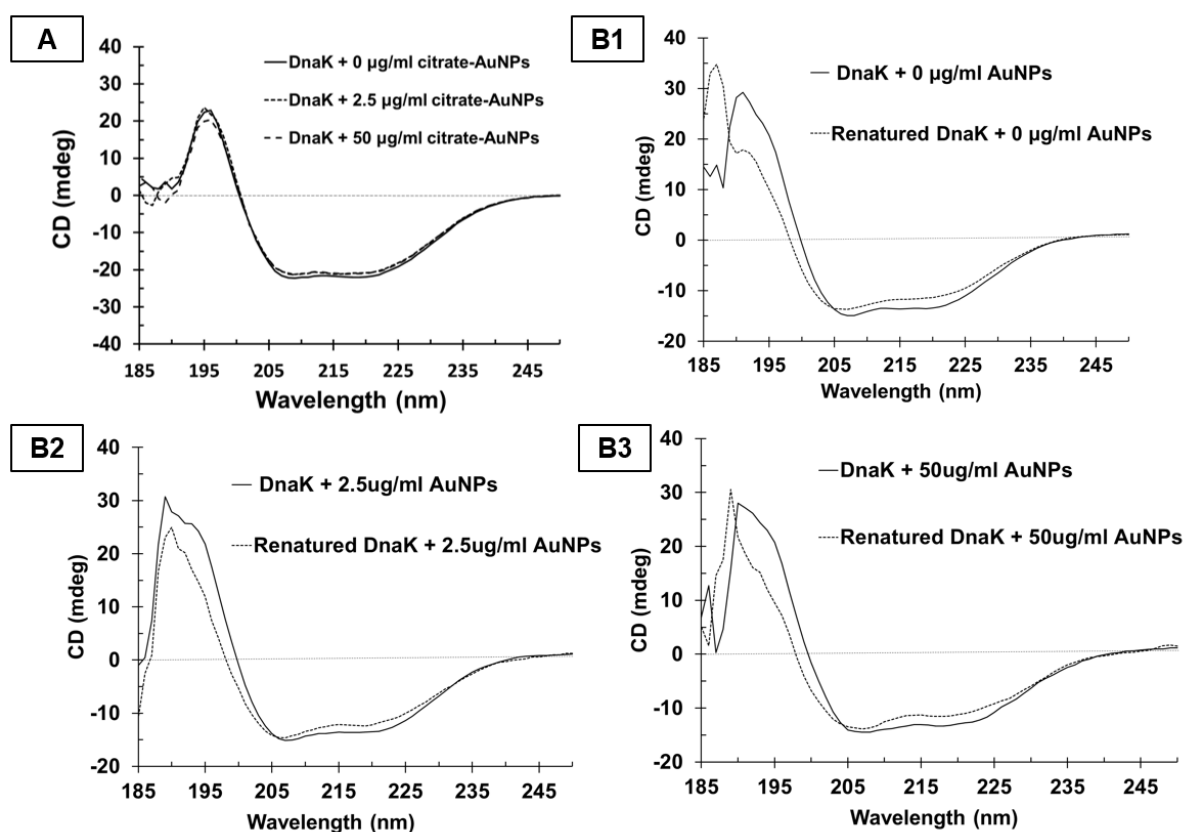


Figure 4.5. Citrate-AuNPs do not perturb the secondary structure of DnaK. The secondary structural analysis of DnaK, (A) at 20 °C in the absence and presence of lower and higher order citrate-AuNPs concentrations, (B1) before denaturation at 90 °C and after renaturation by cooling down to 20 °C, (B2) exposed to 2.5 µg/ml citrate-AuNPs then denatured and subsequently renatured, (B3) exposed to 50 µg/ml citrate-AuNPs then denatured and subsequently renatured. All calculations emanated from the Dichroweb tool.

Table 4.3. Comparative secondary structures residue content of DnaK and DnaK exposed to citrate-AuNPs. Comparative analysis was conducted with the use of regression test and indicated statistical significance at $p < 0.01$ between control and each of the citrate-AuNPs.

	Combined α -helices	β -sheets	β -turns	Unordered	Total Content	RMSD
DnaK	0.438	0.264	0.202	0.054	1	0.495
DnaK + 2.5 μ g/ml citrate-AuNPs	0.495	0.232	0.175	0.093	0.995	0.508
DnaK + 50 μ g/ml citrate-AuNPs	0.438	0.265	0.243	0.049	0.995	0.531

After observing no effect on the secondary structure of DnaK, change in the tertiary structure of the DnaK through monitoring of intrinsic fluorescence analyses were conducted using tryptophan fluorescence spectroscopy. DnaK harbors one tryptophan (TRP-102) residue located in its NBD. Although tyrosine (TYR) has a quantum yield similar to that of TRP, the indole group of TRP is considered the dominant source of excitation at ~ 280 nm and emission at $\sim 340 - 350$ nm in proteins (Teale *et al.*, 1957). It was observed that DnaK possessed maxima in the range of 340 - 350 nm depending on external factors such as salt content or temperature, which suggests that the proteins assumed a folded state in which tryptophan residue is buried within the hydrophobic region.

To validate that the structural changes to DnaK were possible, conformational changes on the protein tertiary structure were induced by exposing the protein to chaotropic denaturant, urea (Fig 4.6B). The protein was incubated with an increasing concentration of urea (0 – 8 μ M) and analyzed. Fluorescence intensity decreased with a red spectral shift being observed (Fig 4.6B, D). Red spectral shift indicated a tertiary structural conformational change due to the presence of varying concentrations of urea. At 4 μ M urea, complete perturbation of DnaK was achieved.

Fluorescence spectra of DnaK either in the presence or absence of citrate-AuNPs did not indicate any changes to the tertiary structure of DnaK as expected of proteins under modulation by external agents (Fig 4.6 A). This may suggest that the tryptophan residues in DnaK remained buried within the hydrophobic core and not exposed to the microenvironment. Hence, fluorescence intensity is quenched from above 400 arbitrary units to less than 100 units without red or blue spectral shift. Fluorescence

intensity decreased with the increasing citrate-AuNPs, indicating the extent to which the presence of citrate-AuNPs induces a change in buffer composition (Fig 4.5). Dehydration of buffer induced quenching of hydrophilic residues of the protein resulting in decreased relative intensity. Lack of spectral shift is due to TRP hidden in deep hydrophobic pockets remaining unaffected by either change in buffer composition or citrate-AuNPs binding. Although there was sufficient quenching of the protein as seen in the decrease of the fluorescence intensity, the tertiary structure of DnaK remained intact.

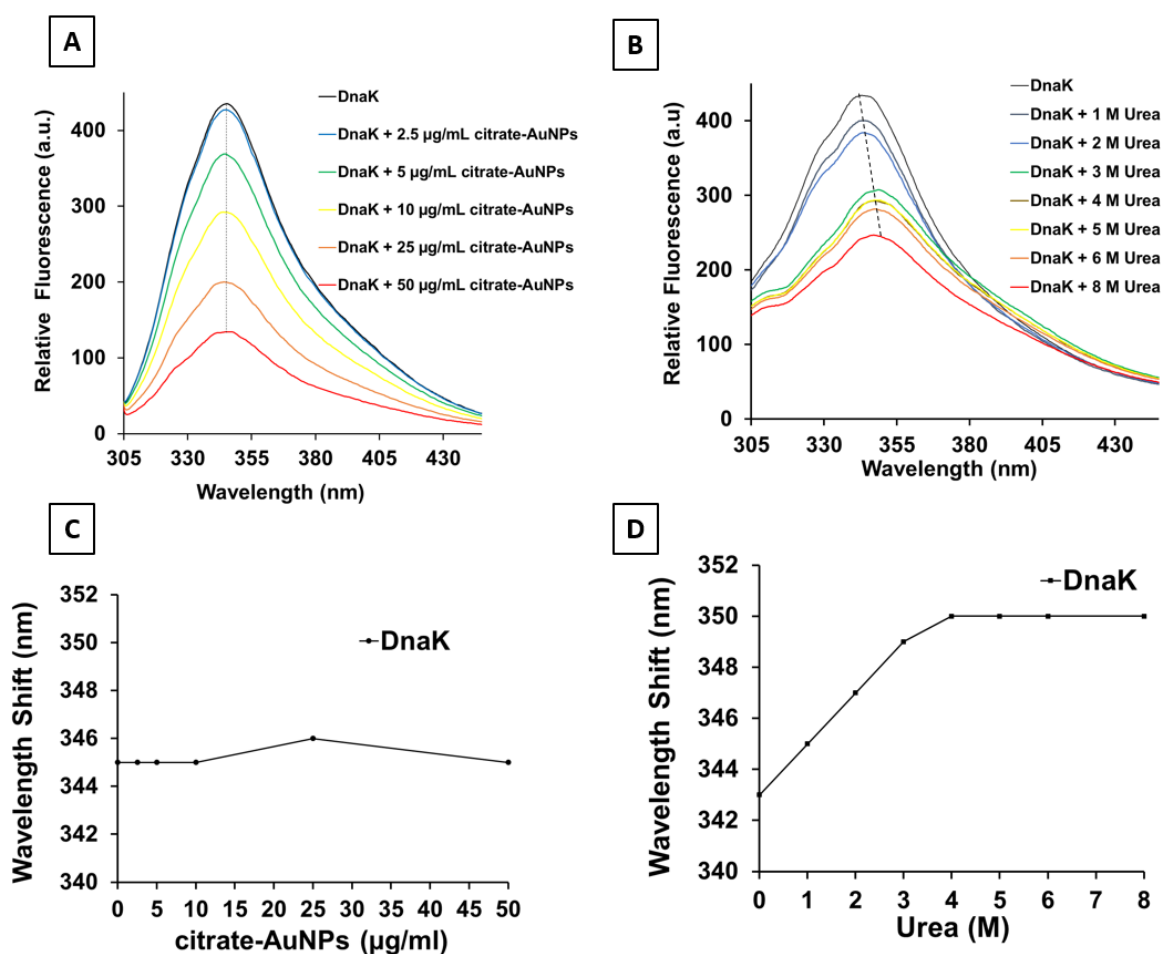


Figure 4.6. Citrate-AuNPs have no effect on the tertiary structure of DnaK. The stability of DnaK in the presence of citrate-AuNPs was not affected either at lower order or higher order of AuNPs concentration. (A) Relative fluorescence intensities of DnaK in the presence of a range of citrate-AuNPs from 0 – 50 µg/ml. (B) Relative fluorescence intensities of DnaK in the presence of a range of urea concentration from 0 – 8 M. (C) Wavelength shifts were calculated from the highest fluorescence intensities of the untreated protein, citrate-AuNPs indicated little to no effect on the wavelength shift of DnaK. (D) Redshift intensity was determined when DnaK was treated to urea concentrations.

4.4. DISCUSSION

The current study sought to determine the effect of citrate-AuNPs on functional features and in modulating the secondary and tertiary structural conformations of DnaK *in vitro*. Based on the STRING prediction of the possible interaction partners of DnaK, DnaJ is a known co-chaperone of DnaK and is also listed among the proteins with experimental evidence of functional interaction (Kityk *et al.*, 2015). Hence the inclusion of DnaJ in the biochemical assays. In the presence of citrate-AuNPs, the function of DnaK together with co-chaperone DnaJ in suppressing aggregation of MDH was enhanced. Furthermore, DnaJ stimulated more effectively the hydrolysis of ATP by DnaK in the presence of citrate-AuNPs. As seen in the high catalytic efficiency exhibited by DnaK and DnaJ in the presence of citrate-AuNPs compared to that of DnaK and DnaJ on their own *in vitro*. Although without GrpE, DnaK and DnaJ can hydrolyze ATP (Kityk *et al.*, 2015). Although according to Nunes and colleagues (2015) the addition of GrpE to experiments in the presence of DnaJ and DnaK lowers the fraction of unfolded states of peptides and marginally increases the fraction of folded and peptides, which is not established in the current study is whether citrate-AuNPs could replace GrpE in its functional responsibilities in ATP hydrolysis or NPs and GrpE could completely be independent in function. It is important to note that only lower-order concentration of NPs in this regard has higher catalytic efficiency as the higher-order concentration had a detrimental effect on the proteins hindering their normal or elevated function in the process. Citrate-AuNPs were also unsuccessful in elevating the ATPase activity of DnaK but instead abrogated it. With the cooperation of chaperone DnaK and co-chaperone DnaJ, citrate-AuNPs also failed to reverse the aggregation of MDH. On the contrary, it was interesting to note the role of lower order (2.5 µg/ml) concentrations of citrate-AuNPs in cooperation with co-chaperone DnaJ in stimulating DnaK ATPase activity *in vitro*. These findings are in support of a previous proposal by Makumire *et al* (2015) that citrate-AuNPs at lower concentrations maintain proper conformation of proteins while at higher concentrations, citrate-AuNPs agglomerate and lead to protein conformation.

DnaK did not exhibit any tertiary structural conformational changes in the presence of citrate-AuNPs but instead remained stable. After observing no spectral shift in emission maxima of DnaK in the presence and absence of citrate-AuNPs, it was speculated that the effect citrate-AuNPs have on the protein is quenching of hydrophobic residues burying tryptophan. Tryptophan residue (W102) in the NBD is buried within the hydrophobic core and packed against SBD α (Swain *et al.*, 2007), the presence of citrate-AuNPs created a more hydrophobic tryptophan microenvironment as the concentration increases which results in quenching of fluorescence intensities. Citrate-AuNPs do not induce conformational changes in DnaK, therefore DnaK would be able to function optimally in the presence of citrate-AuNPs. It is not known at this stage how citrate-AuNPs elevate the ATPase activity of DnaK without modulating structural changes of the protein.

This study noted that the lower concentration ($< 2.5 \mu\text{g/ml}$) of citrate-AuNPs had a stabilizing effect on the secondary structure of DnaK. DnaK treated to high temperatures in the presence of citrate-AuNPs could retain more of their alpha-helical content than DnaK alone or DnaK exposed to temperatures above $65 \text{ }^\circ\text{C}$. While NPs seemed to have a stabilizing effect on DnaK secondary structure, chaotropic denaturants significantly destabilize the structure of DnaK causing a redshift. Findings from the current study would suggest that the citrate-AuNPs slightly enhances the stability of DnaK under high temperatures by taking most of the heat to itself while allowing DnaK to take less heat at the same time (De and Rotello, 2008).

AuNPs are also heat tolerant, which explains the slightly increased tenacity of DnaK in the presence of citrate-NPs.

CHAPTER 5

5. CONCLUDING REMARKS AND FUTURE PERSPECTIVES

5.1. CONCLUDING REMARKS

An understanding of every aspect of the triangle protein-nanoparticle-protein interaction is highly unlikely to be achieved in a short space of time. Nevertheless, it must start with the prediction of possible interaction of known proteins in the same system. Here, prediction tools which included the STRING database were instrumental in giving important details to enable the initial steps into understanding molecular networks of DnaK interaction partners including the co-chaperone DnaJ and chaperone GroEL.

Gold nanoparticles continue to gain momentum in biomedical applications. However, the limited understanding of the interaction with proteins impedes their outright success in biomedical applications. The size of particles plays a major role in the determination of surface area to volume ratio, the smaller size of the particles aid absorption into cells. The crystalline surface curvature also plays a role in the binding of proteins while influencing structural modifications of proteins. A slightly negative to neutral charge determined by the zetasizer meant that a fraction of the concentration of citrate-AuNPs would not be adsorbed or absorbed into cells since repulsion is to be expected at the negatively charged peptidoglycan membrane layer of *E. coli* in vivo. These particles possess less danger to negatively charged DNA material, hence *E. coli* continues to grow in the presence of citrate-AuNPs. Due to the slightest charged capping of the particles, the amino acids such as aspartic acid and glutamic acid are negatively charged at pH 6.9 – 7.9 and contain acidic side chains that would propagate non-binding of the protein domains which are dominated by the two amino acids. Lysine, arginine, and histidine contain basic side chains and is positively charged, as such would be the target binding residues of the particles on the protein.

This study mainly investigated the proteomic changes on *E. coli* cells and proteins due to the presence of citrate-AuNPs by way of identifying and quantifying upregulated proteins by LC-MS/MS which has not been studied or reported elsewhere currently. The emergence of SurA which is a survival membrane protein co-eluting with DnaK

gave a different insight to what was expected from possible interaction partners' prediction in the previous section. SurA happened to be the only possible interaction partner identified by LC-MS/MS sharing the hydrophobic transmembrane property (Appendix A-2) with DnaK while the rest are cytosolic. It is therefore assumed that DnaK functions alongside SurA in alleviating external stress such as aggregated citrate-AuNPs forcibly entering cells. The presence of diminishing ClpX could not be linked to citrate-AuNPs but merely to its role in cell division. GAPDH, a known enteropathogenic protein is important for the pathogenesis of most *E. coli* strains but not known to cooperate with the DnaK chaperone system during cellular stressful conditions. Therefore, the presence of GAPDH in large quantities could talk to the much less quantity of DnaK and DnaJ in the wild-type strain of *E. coli*.

Generally, citrate-AuNPs did not induce conformational changes to DnaK. But it is important to note that at higher concentrations ($> 10 \mu\text{g/ml}$ citrate-AuNPs), quenching of the fluorescence intensity might indicate that the microenvironment surrounding DnaK is dehydrated with the increase of concentration of citrate-AuNPs molecules. Therefore, the hydrophilic residues are exposed, but most importantly, tryptophan (102) gets buried even further in a hydrophobic patch resulting in decreased fluorescence but no conformational change.

The ATPase and the MDH aggregation suppression assays gave an insight into the functional cooperation between citrate-AuNPs and the DnaK chaperone system. The overall conclusion from the current study suggests that lower concentrations ($< 2.5\mu\text{g/ml}$) citrate-AuNPs do not induce changes in structural conformation of DnaK but instead enhances its functional activity together with co-chaperone DnaJ. AuNPs are also heat tolerant, which explains the slightly increased tenacity of DnaK in the presence of metallic NPs. SurA survival protein is likely to encounter citrate-AuNPs before any other cytosolic molecular chaperones which explains its co-existence with DnaK in vivo and in vitro almost similarly. Overall, the study demonstrated that at low concentrations ($<10 \mu\text{g/ml}$), citrate-AuNPs do not disrupt the structural integrity of DnaK. Furthermore, low levels of citrate-AuNPs did not disrupt integrity of network partnerships of DnaK. At higher concentrations ($>10 \mu\text{g/ml}$), citrate-AuNPs compromise the structural conformation and integrity of DnaK network partnership.

Altogether, the findings suggest that at lower concentrations, citrate-AuNPs could be safely integrated within living systems without destabilizing the structure and function of proteins.

5.2. FUTURE PERSPECTIVE

It should be noted that techniques such as affinity chromatography used to determine protein interactions may have limitations as a stand-alone technique. Future studies should make use of techniques such as immunogold labelling, protein-correlation-profiling (PCP) in combination with exhaustive qualitative proteomics methods. Stable isotope labelling of amino acids in cell culture (SILAC) must be considered to identify protein complexes under native expression conditions and without genetic manipulation (Carlson *et al.*, 2019). The use of SPR tool will enhance and validate the outcomes from the use of affinity chromatography in determining interaction of proteins. After the validation that DnaK and DnaJ co-chaperone are also enhanced by the presence of citrate-AuNPs without GrpE, it would be interesting to determine whether AuNPs could act as a NEF in place of GrpE which is the main player in the continuing life cycle of heat shock proteins. It would be highly recommended that such a study be designed to determine the extent to which AuNPs could be applied in place of certain molecular chaperones such ClpB and ClpX which share SBD with GrpE. If such assumptions could be proven valid, biomedical and therapeutic applications will be advanced. Generally, the protective efficacy of DnaK towards the cell survivability in presence of AuNPs against thermal stress should be studied in detail.

6. REFERENCE LIST

- Adur, A. J., Nandini, N., Shilpashree Mayachar, K., Ramya, R., & Srinatha, N. (2018). Bio-synthesis and antimicrobial activity of silver nanoparticles using anaerobically digested parthenium slurry. *Journal of Photochemistry and Photobiology B: Biology*, 183, 30–34. <https://doi.org/10.1016/j.jphotobiol.2018.04.020>
- Ahmed, S., Ahmad, M., Swami, B. L., & Ikram, S. (2016). A review on plants extract mediated synthesis of silver nanoparticles for antimicrobial applications: A green expertise. *Journal of Advanced Research*, 7(1), 17–28. <https://doi.org/10.1016/j.jare.2015.02.007>
- Alim, S., Vejayan, J., Yusoff, M. M., & Kafi, A. K. M. (2018). Recent uses of carbon nanotubes & gold nanoparticles in electrochemistry with application in biosensing: A review. *Biosensors and Bioelectronics*, 121, 125–136. <https://doi.org/10.1016/j.bios.2018.08.051>
- Al-Johani, H., Abou-Hamad, E., Jedidi, A., Widdifield, C. M., Viger-Gravel, J., Sangaru, S. S., Gajan, D., Anjum, D. H., Ould-Chikh, S., Hedhili, M. N., Gurinov, A., Kelly, M. J., El Eter, M., Cavallo, L., Emsley, L., & Basset, J.-M. (2017). The structure and binding mode of citrate in the stabilization of gold nanoparticles. *Nature Chemistry*, 9(9), 890–895. <https://doi.org/10.1038/nchem.2752>
- Amendola, V., Amans, D., Ishikawa, Y., Koshizaki, N., Scirè, S., Compagnini, G., Reichenberger, S., & Barcikowski, S. (2020). Room-Temperature Laser Synthesis in Liquid of Oxide, Metal-Oxide Core-Shells, and Doped Oxide Nanoparticles. *Chemistry – A European Journal*, 26(42), 9206–9242. <https://doi.org/10.1002/chem.202000686>
- Andrievski, R. A., & Glezer, A. M. (2009). Strength of nanostructures. *Physics-Uspekhi*, 52(4), 315–334. <https://doi.org/10.3367/ufne.0179.200904a.0337>
- Arafa, W. M., Aboelhadid, S. M., Moawad, A., Shokeir, K. M., & Ahmed, O. (2020). Toxicity, repellency and anti-cholinesterase activities of thymol-eucalyptus combinations against phenotypically resistant *Rhipicephalus annulatus* ticks. *Experimental and Applied Acarology*, 81(2), 265–277. <https://doi.org/10.1007/s10493-020-00506-1>
- Arora, S., Rajwade, J. M., & Paknikar, K. M. (2012). Nanotoxicology and in vitro studies: The need of the hour. *Toxicology and Applied Pharmacology*, 258(2), 151–165. <https://doi.org/10.1016/j.taap.2011.11.010>
- Avellaneda, M. J., Franke, K. B., Sunderlikova, V., Bukau, B., Mogk, A., & Tans, S. J. (2020). Processive extrusion of polypeptide loops by a Hsp100 disaggregase. *Nature*, 578(7794), 317–320. <https://doi.org/10.1038/s41586-020-1964-y>
- Ayala-Orozco, C., Urban, C., Bishnoi, S., Urban, A., Charron, H., Mitchell, T., Shea, M., Nanda, S., Schiff, R., Halas, N., & Joshi, A. (2014). Sub-100nm gold nanomatryoshkas improve photo-thermal therapy efficacy in large and highly aggressive triple negative breast tumors. *Journal of Controlled Release*, 191, 90–97. <https://doi.org/10.1016/j.jconrel.2014.07.038>

- Bajaj, M., Wangoo, N., Jain, D. V. S., & Sharma, R. K. (2020). Quantification of adsorbed and dangling citrate ions on gold nanoparticle surface using thermogravimetric analysis. *Scientific Reports*, *10*(1), 1038–1049. <https://doi.org/10.1038/s41598-020-65013-0>
- Banerjee, R., Jayaraj, G. G., Peter, J. J., Kumar, V., & Mapa, K. (2016). Monitoring conformational heterogeneity of the lid of DnaK substrate-binding domain during its chaperone cycle. *The FEBS Journal*, *283*(15), 2853–2868. <https://doi.org/10.1111/febs.13769>
- Bertelsen, E. B., Chang, L., Gestwicki, J. E., & Zuiderweg, E. R. P. (2009). Solution conformation of wild-type *E. coli* Hsp70 (DnaK) chaperone complexed with ADP and substrate. *Proceedings of the National Academy of Sciences*, *106*(21), 8471–8476. <https://doi.org/10.1073/pnas.0903503106>
- Blom, R. A. M., Amacker, M., van Dijk, R. M., Moser, C., Stumbles, P. A., Blank, F., & von Garnier, C. (2017). Pulmonary Delivery of Virosome-Bound Antigen Enhances Antigen-Specific CD4+ T Cell Proliferation Compared to Liposome-Bound or Soluble Antigen. *Frontiers in Immunology*, *8*, 1–17. <https://doi.org/10.3389/fimmu.2017.00359>
- Boyles, M. S. P., Kristl, T., Andosch, A., Zimmermann, M., Tran, N., Casals, E., Himly, M., Puentes, V., Huber, C. G., Lütz-Meindl, U., & Duschl, A. (2015). Chitosan functionalisation of gold nanoparticles encourages particle uptake and induces cytotoxicity and pro-inflammatory conditions in phagocytic cells, as well as enhancing particle interactions with serum components. *Journal of Nanobiotechnology*, *13*(1), 1186. <https://doi.org/10.1186/s12951-015-0146-9>
- Bracher, A., & Verghese, J. (2015). The nucleotide exchange factors of Hsp70 molecular chaperones. *Frontiers in Molecular Biosciences*, *2*, 1010–1017. <https://doi.org/10.3389/fmolb.2015.00010>
- Bukau, B., & Walker, G. C. (1989). Cellular defects caused by deletion of the *Escherichia coli* dnaK gene indicate roles for heat shock protein in normal metabolism. *Journal of Bacteriology*, *171*(5), 2337–2346. <https://doi.org/10.1128/jb.171.5.2337-2346.1989>
- Bukau, B., & Walker, G. C. (1990). Mutations altering heat shock specific subunit of RNA polymerase suppress major cellular defects of *E. coli* mutants lacking the DnaK chaperone. *The EMBO Journal*, *9*(12), 4027–4036. <https://doi.org/10.1002/j.1460-2075.1990.tb07624.x>
- Bukau, B., Weissman, J., & Horwich, A. (2006). Molecular Chaperones and Protein Quality Control. *Cell*, *125*(3), 443–451. <https://doi.org/10.1016/j.cell.2006.04.014>
- Calloni, G., Chen, T., Schermann, S. M., Chang, H.-, Genevoux, P., Agostini, F., Tartaglia, G. G., Hayer-Hartl, M., & Hartl, F. U. (2012). DnaK Functions as a Central Hub in the *E. coli* Chaperone Network. *Cell Reports*, *1*(3), 251–264. <https://doi.org/10.1016/j.celrep.2011.12.007>
- Carlson, M. L., Stacey, R. G., Young, J. W., Wason, I. S., Zhao, Z., Rattray, D. G., Scott, N., Kerr, C. H., Babu, M., Foster, L. J., & Duong Van Hoa, F. (2019a). Profiling the *Escherichia coli* membrane protein interactome captured in Peptidisc libraries. *ELife*, *8*, 615–622. <https://doi.org/10.7554/elife.46615>

- Ceballos-Alcantarilla, E., Abad-Somovilla, A., Agulló, C., Abad-Fuentes, A., & Mercader, J. V. (2017). Protein-Free Hapten-Carbon Nanotube Constructs Induce the Secondary Immune Response. *Bioconjugate Chemistry*, 28(6), 1630–1638. <https://doi.org/10.1021/acs.bioconjchem.6b00653>
- Chahal, J. S., Khan, O. F., Cooper, C. L., McPartlan, J. S., Tsosie, J. K., Tilley, L. D., Sidik, S. M., Lourido, S., Langer, R., Bavari, S., Ploegh, H. L., & Anderson, D. G. (2016). Dendrimer-RNA nanoparticles generate protective immunity against lethal Ebola, H1N1 influenza, and *Toxoplasma gondii* challenges with a single dose. *Proceedings of the National Academy of Sciences*, 113(29), E4133–E4142. <https://doi.org/10.1073/pnas.1600299113>
- Chakraborty, A., & Biswas, A. (2020). Structure, stability and chaperone function of Mycobacterium leprae Heat Shock Protein 18 are differentially affected upon interaction with gold and silver nanoparticles. *International Journal of Biological Macromolecules*, 152, 250–260. <https://doi.org/10.1016/j.ijbiomac.2020.02.182>
- Chakraborty, A., Nandi, S. K., Panda, A. K., Mahapatra, P. P., Giri, S., & Biswas, A. (2018). Probing the structure-function relationship of Mycobacterium leprae HSP18 under different UV radiations. *International Journal of Biological Macromolecules*, 119, 604–616. <https://doi.org/10.1016/j.ijbiomac.2018.07.151>
- Chatterjee, A., Rajarshi, K., Ghosh, H., Singh, M. K., Roy, O. P., & Ray, S. (2020). Molecular chaperones in protein folding and stress management in cyanobacteria. *Advances in Cyanobacterial Biology*, 119–128. <https://doi.org/10.1016/b978-0-12-819311-2.00008-5>
- Chatterjee, S., Bandyopadhyay, A., & Sarkar, K. (2011). Effect of iron oxide and gold nanoparticles on bacterial growth leading towards biological application. *Journal of Nanobiotechnology*, 9(1), 34. <https://doi.org/10.1186/1477-3155-9-34>
- Cheng, Y. H., Riviere, J. E., Monteiro-Riviere, N. A., & Lin, Z. (2018). Probabilistic risk assessment of gold nanoparticles after intravenous administration by integrating in vitro and in vivo toxicity with physiologically based pharmacokinetic modeling. *Nanotoxicology*, 12(5), 453–469. <https://doi.org/10.1080/17435390.2018.1459922>
- Chibber, S., & Ahmad, I. (2016). Molecular docking, a tool to determine interaction of CuO and TiO₂ nanoparticles with human serum albumin. *Biochemistry and Biophysics Reports*, 6, 63–67. <https://doi.org/10.1016/j.bbrep.2016.03.004>
- Cui, W., Li, J., Zhang, Y., Rong, H., Lu, W., & Jiang, L. (2012). Effects of aggregation and the surface properties of gold nanoparticles on cytotoxicity and cell growth. *Nanomedicine: Nanotechnology, Biology and Medicine*, 8(1), 46–53. <https://doi.org/10.1016/j.nano.2011.05.005>
- Cyr, D. M. (2008). Swapping Nucleotides, Tuning Hsp70. *Cell*, 133(6), 945–947. <https://doi.org/10.1016/j.cell.2008.05.036>
- Darwish, M. S. A., Nguyen, N. H. A., Ševců, A., & Stibor, I. (2015). Functionalized Magnetic Nanoparticles and Their Effect on *Escherichia coli* and *Staphylococcus aureus*. *Journal of Nanomaterials*, 2015, 1–10. <https://doi.org/10.1155/2015/416012>

- de Jong. (2008). Drug delivery and nanoparticles: Applications and hazards. *International Journal of Nanomedicine*, 133. <https://doi.org/10.2147/ijn.s596>
- De Los Rios, P., & Barducci, A. (2014). Hsp70 chaperones are non-equilibrium machines that achieve ultra-affinity by energy consumption. *ELife*, 3, 1–10. <https://doi.org/10.7554/elife.02218>
- De, M., & Rotello, V. M. (2008). Synthetic “chaperones”: nanoparticle-mediated refolding of thermally denatured proteins. *Chemical Communications*, 30, 3504. <https://doi.org/10.1039/b805242e>
- de Marco, A. (2007). Protocol for preparing proteins with improved solubility by co-expressing with molecular chaperones in *Escherichia coli*. *Nature Protocols*, 2(10), 2632–2639. <https://doi.org/10.1038/nprot.2007.400>
- Deraedt, C., Salmon, L., Gatard, S., Ciganda, R., Hernandez, R., Ruiz, J., & Astruc, D. (2014). Sodium borohydride stabilizes very active gold nanoparticle catalysts. *Chem. Commun.*, 50(91), 14194–14196. <https://doi.org/10.1039/c4cc05946h>
- Deville, C., Carroni, M., Franke, K. B., Topf, M., Bukau, B., Mogk, A., & Saibil, H. R. (2017). Structural pathway of regulated substrate transfer and threading through an Hsp100 disaggregase. *Science Advances*, 3(8), e1701726. <https://doi.org/10.1126/sciadv.1701726>
- Dörr, J. M., Koorengel, M. C., Schäfer, M., Prokofyev, A. V., Scheidelaar, S., van der Crujisen, E. A. W., Dafforn, T. R., Baldus, M., & Killian, J. A. (2014). Detergent-free isolation, characterization, and functional reconstitution of a tetrameric K⁺ channel: The power of native nanodiscs. *Proceedings of the National Academy of Sciences*, 111(52), 18607–18612. <https://doi.org/10.1073/pnas.1416205112>
- Eftink, M. R. (1991). Fluorescence Quenching Reactions. *Biophysical and Biochemical Aspects of Fluorescence Spectroscopy*, 1–41. https://doi.org/10.1007/978-1-4757-9513-4_1
- Egea, L., Aguilera, L., Giménez, R., Sorolla, M. A., Aguilar, J., Badía, J., & Baldoma, L. (2007). Role of secreted glyceraldehyde-3-phosphate dehydrogenase in the infection mechanism of enterohemorrhagic and enteropathogenic *Escherichia coli*: Interaction of the extracellular enzyme with human plasminogen and fibrinogen. *The International Journal of Biochemistry & Cell Biology*, 39(6), 1190–1203. <https://doi.org/10.1016/j.biocel.2007.03.008>
- Espinosa, A., Silva, A. K. A., Sánchez-Iglesias, A., Grzelczak, M., Péchoux, C., Desboeufs, K., Liz-Marzán, L. M., & Wilhelm, C. (2016). Cancer Cell Internalization of Gold Nanostars Impacts Their Photothermal Efficiency In Vitro and In Vivo: Toward a Plasmonic Thermal Fingerprint in Tumoral Environment. *Advanced Healthcare Materials*, 5(9), 1040–1048. <https://doi.org/10.1002/adhm.201501035>
- Fang, R. H., Hu, C.-M. J., Chen, K. N. H., Luk, B. T., Carpenter, C. W., Gao, W., Li, S., Zhang, D.-E., Lu, W., & Zhang, L. (2013). Lipid-insertion enables targeting functionalization of erythrocyte membrane-cloaked nanoparticles. *Nanoscale*, 5(19), 8884. <https://doi.org/10.1039/c3nr03064d>

- Fei, L., & Perrett, S. (2009). Effect of Nanoparticles on Protein Folding and Fibrillogenesis. *International Journal of Molecular Sciences*, 10(2), 646–655. <https://doi.org/10.3390/ijms10020646>
- Fernández-Fernández, M. R., Sot, B., & Valpuesta, J. M. (2016). Molecular chaperones: functional mechanisms and nanotechnological applications. *Nanotechnology*, 27(32), 324004. <https://doi.org/10.1088/0957-4484/27/32/324004>
- Fratoddi, I., Venditti, I., Battocchio, C., Carlini, L., Amatori, S., Porchia, M., Tisato, F., Bondino, F., Magnano, E., Pellei, M., & Santini, C. (2019). Highly Hydrophilic Gold Nanoparticles as Carrier for Anticancer Copper(I) Complexes: Loading and Release Studies for Biomedical Applications. *Nanomaterials*, 9(5), 772. <https://doi.org/10.3390/nano9050772>
- Gagner, J. E., Qian, X., Lopez, M. M., Dordick, J. S., & Siegel, R. W. (2012). Effect of gold nanoparticle structure on the conformation and function of adsorbed proteins. *Biomaterials*, 33(33), 8503–8516. <https://doi.org/10.1016/j.biomaterials.2012.07.009>
- Gagner, J. E., Shrivastava, S., Qian, X., Dordick, J. S., & Siegel, R. W. (2012). Engineering Nanomaterials for Biomedical Applications Requires Understanding the Nano-Bio Interface: A Perspective. *The Journal of Physical Chemistry Letters*, 3(21), 3149–3158. <https://doi.org/10.1021/jz301253s>
- Genc, R., Clergeaud, G., Ortiz, M., & O'Sullivan, C. (2014). Shape directed biomineralization of gold nanoparticles using self-assembled lipid structures. *Biomater. Sci.*, 2(8), 1128–1134. <https://doi.org/10.1039/c4bm00025k>
- Georgopoulos, C. P., Lam, B., Lundquist-Heil, A., Rudolph, C. F., Yochem, J., & Feiss, M. (1979). Identification of the *E. coli* dnaK (groPC756) gene product. *Molecular and General Genetics MGG*, 172(2), 143–149. <https://doi.org/10.1007/bf00268275>
- Giri, K., Shameer, K., Zimmermann, M. T., Saha, S., Chakraborty, P. K., Sharma, A., Arviso, R. R., Madden, B. J., McCormick, D. J., Kocher, J.-P. A., Bhattacharya, R., & Mukherjee, P. (2014). Understanding Protein–Nanoparticle Interaction: A New Gateway to Disease Therapeutics. *Bioconjugate Chemistry*, 25(6), 1078–1090. <https://doi.org/10.1021/bc500084f>
- Glezer, A. M. (2011). Structural Classification of Nanomaterials. *Russian Metallurgy (Metally)*, 2011(4), 263–269. <https://doi.org/10.1134/s0036029511040057>
- Gobin, A. M., Lee, M. H., Halas, N. J., James, W. D., Drezek, R. A., & West, J. L. (2007). Near-Infrared Resonant Nanoshells for Combined Optical Imaging and Photothermal Cancer Therapy. *Nano Letters*, 7(7), 1929–1934. <https://doi.org/10.1021/nl070610y>
- Gomes, L. P., Anjo, S. I., Manadas, B., Coelho, A. V., & Paschoalin, V. M. F. (2019). Proteomic Analyses Reveal New Insights on the Antimicrobial Mechanisms of Chitosan Biopolymers and Their Nanosized Particles against *Escherichia coli*. *International Journal of Molecular Sciences*, 21(1), 225. <https://doi.org/10.3390/ijms21010225>
- Grys, D. B., de Nijs, B., Salmon, A. R., Huang, J., Wang, W., Chen, W. H., Scherman, O. A., & Baumberg, J. J. (2020). Citrate Coordination and Bridging of Gold Nanoparticles:

- The Role of Gold Adatoms in AuNP Aging. *ACS Nano*, 14(7), 8689–8696. <https://doi.org/10.1021/acsnano.0c03050>
- Hartl, F. U., Bracher, A., & Hayer-Hartl, M. (2011). Molecular chaperones in protein folding and proteostasis. *Nature*, 475(7356), 324–332. <https://doi.org/10.1038/nature10317>
- Hartl, F. U., & Hayer-Hartl, M. (2009). Converging concepts of protein folding in vitro and in vivo. *Nature Structural & Molecular Biology*, 16(6), 574–581. <https://doi.org/10.1038/nsmb.1591>
- Henderson, B., & Martin, A. C. R. (2014). Protein moonlighting: a new factor in biology and medicine. *Biochemical Society Transactions*, 42(6), 1671–1678. <https://doi.org/10.1042/bst20140273>
- Humes, J. R., Schiffrin, B., Calabrese, A. N., Higgins, A. J., Westhead, D. R., Brockwell, D. J., & Radford, S. E. (2019). The Role of SurA PPIase Domains in Preventing Aggregation of the Outer-Membrane Proteins tOmpA and OmpT. *Journal of Molecular Biology*, 431(6), 1267–1283. <https://doi.org/10.1016/j.jmb.2019.01.032>
- Jha, R. K., Jha, P. K., Chaudhury, K., Rana, S. V. S., & Guha, S. K. (2014). An emerging interface between life science and nanotechnology: present status and prospects of reproductive healthcare aided by nano-biotechnology. *Nano Reviews*, 5(1), 22762. <https://doi.org/10.3402/nano.v5.22762>
- Kampinga, H. H., Andreasson, C., Barducci, A., Cheetham, M. E., Cyr, D., Emanuelsson, C., Genevaux, P., Gestwicki, J. E., Goloubinoff, P., Huerta-Cepas, J., Kirstein, J., Liberek, K., Mayer, M. P., Nagata, K., Nillegoda, N. B., Pulido, P., Ramos, C., De los Rios, P., Rospert, S., . . . Marszalek, J. (2018). Function, evolution, and structure of J-domain proteins. *Cell Stress and Chaperones*, 24(1), 7–15. <https://doi.org/10.1007/s12192-018-0948-4>
- Kampinga, H. H., & Craig, E. A. (2010). The HSP70 chaperone machinery: J proteins as drivers of functional specificity. *Nature Reviews Molecular Cell Biology*, 11(8), 579–592. <https://doi.org/10.1038/nrm2941>
- Keller, A., Nesvizhskii, A. I., Kolker, E., & Aebersold, R. (2002). Empirical Statistical Model To Estimate the Accuracy of Peptide Identifications Made by MS/MS and Database Search. *Analytical Chemistry*, 74(20), 5383–5392. <https://doi.org/10.1021/ac025747h>
- Kelley, L. A., Mezulis, S., Yates, C. M., Wass, M. N., & Sternberg, M. J. E. (2015). The Phyre2 web portal for protein modeling, prediction and analysis. *Nature Protocols*, 10(6), 845–858. <https://doi.org/10.1038/nprot.2015.053>
- Kim, Y. E., Hipp, M. S., Bracher, A., Hayer-Hartl, M., & Ulrich Hartl, F. (2013). Molecular Chaperone Functions in Protein Folding and Proteostasis. *Annual Review of Biochemistry*, 82(1), 323–355. <https://doi.org/10.1146/annurev-biochem-060208-092442>
- Kim, Y.-P., & Lee, T. G. (2012). Secondary Ions Mass Spectrometric Signal Enhancement of Peptides on Enlarged-Gold Nanoparticle Surfaces. *Analytical Chemistry*, 84(11), 4784–4788. <https://doi.org/10.1021/ac300336h>

- Kityk, R., Kopp, J., & Mayer, M. P. (2018). Molecular Mechanism of J-Domain-Triggered ATP Hydrolysis by Hsp70 Chaperones. *Molecular Cell*, 69(2), 227–237.e4. <https://doi.org/10.1016/j.molcel.2017.12.003>
- Kityk, R., Kopp, J., Sinning, I., & Mayer, M. P. (2012). Structure and Dynamics of the ATP-Bound Open Conformation of Hsp70 Chaperones. *Molecular Cell*, 48(6), 863–874. <https://doi.org/10.1016/j.molcel.2012.09.023>
- Klaper, R., Arndt, D., Bozich, J., & Dominguez, G. (2014). Molecular interactions of nanomaterials and organisms: defining biomarkers for toxicity and high-throughput screening using traditional and next-generation sequencing approaches. *The Analyst*, 139(5), 882–895. <https://doi.org/10.1039/c3an01644g>
- Klein, G., Devineau, S., Aude, J. C., Boulard, Y., Pasquier, H., Labarre, J., Pin, S., & Renault, J. P. (2015). Interferences of Silica Nanoparticles in Green Fluorescent Protein Folding Processes. *Langmuir*, 32(1), 195–202. <https://doi.org/10.1021/acs.langmuir.5b03890>
- Kravats, A. N., Doyle, S. M., Hoskins, J. R., Genest, O., Doody, E., & Wickner, S. (2017). Interaction of *E. coli* Hsp90 with DnaK Involves the DnaJ Binding Region of DnaK. *Journal of Molecular Biology*, 429(6), 858–872. <https://doi.org/10.1016/j.jmb.2016.12.014>
- Lee, S., Sowa, M. E., Watanabe, Y., Sigler, P. B., Chiu, W., Yoshida, M., & Tsai, F. T. F. (2003). The Structure of ClpB. *Cell*, 115(2), 229–240. [https://doi.org/10.1016/s0092-8674\(03\)00807-9](https://doi.org/10.1016/s0092-8674(03)00807-9)
- Li, Z., Lopez-Ortega, A., Aranda-Ramos, A., Tajada, J. L., Sort, J., Nogues, C., Vavassori, P., Nogues, J., & Sepulveda, B. (2018). Simultaneous Local Heating/Thermometry Based on Plasmonic Magnetochromic Nanoheaters. *Small*, 14(24), 1800868. <https://doi.org/10.1002/smll.201800868>
- Link, S., & El-Sayed, M. A. (2000). Shape and size dependence of radiative, non-radiative and photothermal properties of gold nanocrystals. *International Reviews in Physical Chemistry*, 19(3), 409–453. <https://doi.org/10.1080/01442350050034180>
- Liu, X. Y., Wang, J. Q., Ashby, C. R., Zeng, L., Fan, Y. F., & Chen, Z. S. (2021). Gold nanoparticles: synthesis, physiochemical properties and therapeutic applications in cancer. *Drug Discovery Today*, 01(030), 1359. <https://doi.org/10.1016/j.drudis.2021.01.030>
- Lo, Y. C., Lin, S. C., Shaw, J. F., & Liaw, Y. C. (2003). Crystal Structure of *Escherichia coli* Thioesterase I/Protease I/Lysophospholipase L1: Consensus Sequence Blocks Constitute the Catalytic Center of SGNH-hydrolases through a Conserved Hydrogen Bond Network. *Journal of Molecular Biology*, 330(3), 539–551. [https://doi.org/10.1016/s0022-2836\(03\)00637-5](https://doi.org/10.1016/s0022-2836(03)00637-5)
- Lobley, A., Whitmore, L., & Wallace, B. A. (2002). DICHROWEB: an interactive website for the analysis of protein secondary structure from circular dichroism spectra. *Bioinformatics*, 18(1), 211–212. <https://doi.org/10.1093/bioinformatics/18.1.211>

- Lopes-Rodrigues, R., Xie, F., Porter, A. E., & Ryan, M. P. (2020). Geometry-induced protein reorientation on the spikes of plasmonic gold nanostars. *Nanoscale Advances*, 2(3), 1144–1151. <https://doi.org/10.1039/c9na00584f>
- Luo, H., Wang, J., Li, M., Luo, J., Peng, X., Wu, F.-X., & Pan, Y. (2016). Drug repositioning based on comprehensive similarity measures and Bi-Random walk algorithm. *Bioinformatics*, 32(17), 2664–2671. <https://doi.org/10.1093/bioinformatics/btw228>
- Luthuli, S. D., Chili, M. M., Revaprasadu, N., & Shonhai, A. (2013). Cysteine-capped gold nanoparticles suppress aggregation of proteins exposed to heat stress. *IUBMB Life*, 65(5), 454–461. <https://doi.org/10.1002/iub.1146>
- Njunge, M.J., H. Ludewig, M., Boshoff, A., Pesce, E.-R., & L. Blatch, G. (2013). Hsp70s and J Proteins of Plasmodium Parasites Infecting Rodents and Primates: Structure, Function, Clinical Relevance, and Drug Targets. *Current Pharmaceutical Design*, 19(3), 387–403. <https://doi.org/10.2174/138161213804143734>
- Makhoba, X. H., Burger, A., Coertzen, D., Zininga, T., Birkholtz, L..M., & Shonhai, A. (2016). Use of a Chimeric Hsp70 to Enhance the Quality of Recombinant Plasmodium falciparum S-Adenosylmethionine Decarboxylase Protein Produced in *Escherichia coli*. *PLOS ONE*, 11(3), e0152626. <https://doi.org/10.1371/journal.pone.0152626>
- Maki, J. A., Schnobrich, D. J., & Culver, G. M. (2002). The DnaK Chaperone System Facilitates 30S Ribosomal Subunit Assembly. *Molecular Cell*, 10(1), 129–138. [https://doi.org/10.1016/s1097-2765\(02\)00562-2](https://doi.org/10.1016/s1097-2765(02)00562-2)
- Makumire, S., Chakravadhanula, V. S. K., Köllisch, G., Redel, E., & Shonhai, A. (2014). Immunomodulatory activity of zinc peroxide (ZnO₂) and titanium dioxide (TiO₂) nanoparticles and their effects on DNA and protein integrity. *Toxicology Letters*, 227(1), 56–64. <https://doi.org/10.1016/j.toxlet.2014.02.027>
- Makumire, S., Revaprasadu, N., & Shonhai, A. (2015). DnaK Protein Alleviates Toxicity Induced by Citrate-Coated Gold Nanoparticles in *Escherichia coli*. *PLOS ONE*, 10(4), e0121243. <https://doi.org/10.1371/journal.pone.0121243>
- Maleki Dizaj, S., Lotfipour, F., Barzegar-Jalali, M., Zarrintan, M.-H., & Adibkia, K. (2016). Physicochemical characterization and antimicrobial evaluation of gentamicin-loaded CaCO₃ nanoparticles prepared via microemulsion method. *Journal of Drug Delivery Science and Technology*, 35, 16–23. <https://doi.org/10.1016/j.jddst.2016.05.004>
- Martín, N. (2019). The Legacy of Sir Harold W. Kroto: Fullerenes and Beyond. *Chem*, 5(4), 733–738. <https://doi.org/10.1016/j.chempr.2019.03.015>
- Matur, M., Madhyastha, H., Shruthi, T. S., Madhyastha, R., Srinivas, S. P., Navya, P. N., & Daima, H. K. (2020). Engineering bioactive surfaces on nanoparticles and their biological interactions. *Scientific Reports*, 10(1), 1038. <https://doi.org/10.1038/s41598-020-75465-z>
- Mayer, M. P., & Bukau, B. (2005). Hsp70 chaperones: Cellular functions and molecular mechanism. *Cellular and Molecular Life Sciences*, 62(6), 670–684. <https://doi.org/10.1007/s00018-004-4464-6>

- Mayer, M. P., & Gierasch, L. M. (2018). Recent advances in the structural and mechanistic aspects of Hsp70 molecular chaperones. *Journal of Biological Chemistry*, 294(6), 2085–2097. <https://doi.org/10.1074/jbc.rev118.002810>
- Mayer, M. P., Rüdiger, S., & Bukau, B. (2000). Molecular Basis for Interactions of the DnaK Chaperone with Substrates. *Biological Chemistry*, 381(9–10), 877–885. <https://doi.org/10.1515/bc.2000.109>
- Melero, R., Moro, F., Pérez-Calvo, M. Á., Perales-Calvo, J., Quintana-Gallardo, L., Llorca, O., Muga, A., & Valpuesta, J. M. (2015). Modulation of the Chaperone DnaK Allosterism by the Nucleotide Exchange Factor GrpE. *Journal of Biological Chemistry*, 290(16), 10083–10092. <https://doi.org/10.1074/jbc.m114.623371>
- Mogk, A., Bukau, B., & Kampina, H. H. (2018a). Cellular Handling of Protein Aggregates by Disaggregation Machines. *Molecular Cell*, 69(2), 214–226. <https://doi.org/10.1016/j.molcel.2018.01.004>
- Mogk, A., Bukau, B., & Kampina, H. H. (2018b). Cellular Handling of Protein Aggregates by Disaggregation Machines. *Molecular Cell*, 69(2), 214–226. <https://doi.org/10.1016/j.molcel.2018.01.004>
- Morán Luengo, T., Kityk, R., Mayer, M. P., & Rüdiger, S. G. (2018). Hsp90 Breaks the Deadlock of the Hsp70 Chaperone System. *Molecular Cell*, 70(3), 545–552.e9. <https://doi.org/10.1016/j.molcel.2018.03.028>
- Morris, G. M., Huey, R., Lindstrom, W., Sanner, M. F., Belew, R. K., Goodsell, D. S., & Olson, A. J. (2009). AutoDock4 and AutoDockTools4: Automated docking with selective receptor flexibility. *Journal of Computational Chemistry*, 30(16), 2785–2791. <https://doi.org/10.1002/jcc.21256>
- Muniba, Naz, G., Anjum, M. N., Irfan, M., Irfan, M., Arshad, M., Bajwa, S. Z., & Khan, W. S. (2020). Quats stabilized gold nanospheres for efficient ligand exchange procedure. *Results in Materials*, 5, 100065–100073. <https://doi.org/10.1016/j.rinma.2020.100065>
- Naik, S. N., & Walley, S. M. (2019). The Hall–Petch and inverse Hall–Petch relations and the hardness of nanocrystalline metals. *Journal of Materials Science*, 55(7), 2661–2681. <https://doi.org/10.1007/s10853-019-04160-w>
- Nakamura, A., Takumi, K., & Miki, K. (2010). Crystal Structure of a Thermophilic GrpE Protein: Insight into Thermosensing Function for the DnaK Chaperone System. *Journal of Molecular Biology*, 396(4), 1000–1011. <https://doi.org/10.1016/j.jmb.2009.12.028>
- Nandi, S. K., Chakraborty, A., Panda, A. K., Kar, R. K., Bhunia, A., & Biswas, A. (2018). Evidences for zinc (II) and copper (II) ion interactions with Mycobacterium leprae HSP18: Effect on its structure and chaperone function. *Journal of Inorganic Biochemistry*, 188, 62–75. <https://doi.org/10.1016/j.jinorgbio.2018.08.010>
- Nel, A. (2006). Toxic Potential of Materials at the Nanolevel. *Science*, 311(5761), 622–627. <https://doi.org/10.1126/science.1114397>

- Nemanashi, M., Noh, J. H., & Meijboom, R. (2018). Dendrimers as alternative templates and pore-directing agents for the synthesis of micro- and mesoporous materials. *Journal of Materials Science*, 53(18), 12663–12678. <https://doi.org/10.1007/s10853-018-2527-6>
- Ngweniform, P., Li, D., & Mao, C. (2009). Self-assembly of drug-loaded liposomes on genetically engineered protein nanotubes: a potential anti-cancer drug delivery vector. *Soft Matter*, 5(5), 954. <https://doi.org/10.1039/b817863a>
- Nichols, R. J., Burgess, I., Young, K. L., Zamlynny, V., & Lipkowski, J. (2004). A quantitative evaluation of the adsorption of citrate on Au(111) using SNIFTIRS. *Journal of Electroanalytical Chemistry*, 563(1), 33–39. <https://doi.org/10.1016/j.jelechem.2003.08.007>
- Nowicki, U., Leźnicki, P., Morawiec, E., Litwińczuk, N., & Liberek, K. (2011). Role of a conserved aspartic acid in nucleotide binding domain 1 (NBD1) of Hsp100 chaperones in their activities. *Cell Stress and Chaperones*, 17(3), 361–373. <https://doi.org/10.1007/s12192-011-0312-4>
- Nunes, J. M., Mayer-Hartl, M., Hartl, F. U., & Müller, D. J. (2015). Action of the Hsp70 chaperone system observed with single proteins. *Nature Communications*, 6(1), 1038. <https://doi.org/10.1038/ncomms7307>
- Ogundare, O. D., Akinribide, O. J., Adetunji, A. R., Adeoye, M. O., & Olubambi, P. A. (2019). Crystallite size determination of thermally deposited Gold Nanoparticles. *Procedia Manufacturing*, 30, 173–179. <https://doi.org/10.1016/j.promfg.2019.02.025>
- Paek, K. H., & Walker, G. C. (1987). *Escherichia coli* dnaK null mutants are inviable at high temperature. *Journal of Bacteriology*, 169(1), 283–290. <https://doi.org/10.1128/jb.169.1.283-290.1987>
- Pajerski, W., Ochonska, D., Brzychczy-Wloch, M., Indyka, P., Jarosz, M., Golda-Cepa, M., Sojka, Z., & Kotarba, A. (2019). Attachment efficiency of gold nanoparticles by Gram-positive and Gram-negative bacterial strains governed by surface charges. *Journal of Nanoparticle Research*, 21(8), 1–12. <https://doi.org/10.1007/s11051-019-4617-z>
- Park, C.J., & Seo, Y.S. (2015). Heat Shock Proteins: A Review of the Molecular Chaperones for Plant Immunity. *The Plant Pathology Journal*, 31(4), 323–333. <https://doi.org/10.5423/ppj.rw.08.2015.0150>
- Park, J. C., Choi, S. Y., Yang, M. Y., Nan, L., Na, H., Lee, H. N., Chung, H. J., Hong, C. A., & Nam, Y. S. (2019). Subnanomolar FRET-Based DNA Assay Using Thermally Stable Phosphorothioated DNA-Functionalized Quantum Dots. *ACS Applied Materials & Interfaces*, 11(37), 33525–33534. <https://doi.org/10.1021/acsami.9b07717>
- Park, J.H., Oh, S.G., & Jo, B.-W. (2004). Fabrication of silver nanotubes using functionalized silica rod as templates. *Materials Chemistry and Physics*, 87(2–3), 301–310. <https://doi.org/10.1016/j.matchemphys.2004.05.013>
- Park, J.W., & Shumaker-Parry, J. S. (2014). Structural Study of Citrate Layers on Gold Nanoparticles: Role of Intermolecular Interactions in Stabilizing Nanoparticles. *Journal of the American Chemical Society*, 136(5), 1907–1921. <https://doi.org/10.1021/ja4097384>

- Parveen, R., Shamsi, T. N., & Fatima, S. (2017). Nanoparticles-protein interaction: Role in protein aggregation and clinical implications. *International Journal of Biological Macromolecules*, *94*, 386–395. <https://doi.org/10.1016/j.ijbiomac.2016.10.024>
- Perales-Calvo, J., Muga, A., & Moro, F. (2010). Role of DnaJ G/F-rich Domain in Conformational Recognition and Binding of Protein Substrates. *Journal of Biological Chemistry*, *285*(44), 34231–34239. <https://doi.org/10.1074/jbc.m110.144642>
- Pettersen, E. F., Goddard, T. D., Huang, C. C., Couch, G. S., Greenblatt, D. M., Meng, E. C., & Ferrin, T. E. (2004). UCSF Chimera: A visualization system for exploratory research and analysis. *Journal of Computational Chemistry*, *25*(13), 1605–1612. <https://doi.org/10.1002/jcc.20084>
- Planchon, M., Léger, T., Spalla, O., Huber, G., & Ferrari, R. (2017). Metabolomic and proteomic investigations of impacts of titanium dioxide nanoparticles on *Escherichia coli*. *PLOS ONE*, *12*(6), e0178437. <https://doi.org/10.1371/journal.pone.0178437>
- Raliya, R., & Tarafdar, J. C. (2013). ZnO Nanoparticle Biosynthesis and Its Effect on Phosphorous-Mobilizing Enzyme Secretion and Gum Contents in Clusterbean (*Cyamopsis tetragonoloba* L.). *Agricultural Research*, *2*(1), 48–57. <https://doi.org/10.1007/s40003-012-0049-z>
- Rani, M., Moudgil, L., Singh, B., Kaushal, A., Mittal, A., Saini, G. S. S., Tripathi, S. K., Singh, G., & Kaura, A. (2016). Understanding the mechanism of replacement of citrate from the surface of gold nanoparticles by amino acids: a theoretical and experimental investigation and their biological application. *RSC Advances*, *6*(21), 17373–17383. <https://doi.org/10.1039/c5ra26502a>
- Regiel-Futyra, A., Kus-Liśkiewicz, M. I., Sebastian, V., Irusta, S., Arruebo, M., Stochel, G. Z., & Kyzioł, A. (2015). Development of Noncytotoxic Chitosan–Gold Nanocomposites as Efficient Antibacterial Materials. *ACS Applied Materials & Interfaces*, *7*(2), 1087–1099. <https://doi.org/10.1021/am508094e>
- Rim, K.-T., Song, S.-W., & Kim, H.-Y. (2013). Oxidative DNA Damage from Nanoparticle Exposure and Its Application to Workers' Health: A Literature Review. *Safety and Health at Work*, *4*(4), 177–186. <https://doi.org/10.1016/j.shaw.2013.07.006>
- Rodina, E., Vorobieva, N., Kurilova, S., Mikulovich, J., Vainonen, J., Aro, E.-M., & Nazarova, T. (2011). Identification of new protein complexes of *Escherichia coli* inorganic pyrophosphatase using pull-down assay. *Biochimie*, *93*(9), 1576–1583. <https://doi.org/10.1016/j.biochi.2011.05.023>
- Rodriguez, K. A., Osmulski, P. A., Pierce, A., Weintraub, S. T., Gaczynska, M., & Buffenstein, R. (2014). A cytosolic protein factor from the naked mole-rat activates proteasomes of other species and protects these from inhibition. *Biochimica et Biophysica Acta (BBA) - Molecular Basis of Disease*, *1842*(11), 2060–2072. <https://doi.org/10.1016/j.bbadis.2014.07.005>
- Rodríguez-Limas, W. A., Sekar, K., & Tyo, K. E. J. (2013). Virus-like particles: the future of microbial factories and cell-free systems as platforms for vaccine development. *Current Opinion in Biotechnology*, *24*(6), 1089–1093. <https://doi.org/10.1016/j.copbio.2013.02.008>

- Roy, D., Kumar, V., James, J., Shihabudeen, M. S., Kulshrestha, S., Goel, V., & Thirumurugan, K. (2015). Evidence that Chemical Chaperone 4-Phenylbutyric Acid Binds to Human Serum Albumin at Fatty Acid Binding Sites. *PLOS ONE*, 10(7), e0133012. <https://doi.org/10.1371/journal.pone.0133012>
- Rueden, C. T., Schindelin, J., Hiner, M. C., DeZonia, B. E., Walter, A. E., Arena, E. T., & Eliceiri, K. W. (2017). ImageJ2: ImageJ for the next generation of scientific image data. *BMC Bioinformatics*, 18(1), 112. <https://doi.org/10.1186/s12859-017-1934-z>
- Sahi, C., Kominek, J., Ziegelhoffer, T., Yu, H. Y., Baranowski, M., Marszalek, J., & Craig, E. A. (2013). Sequential Duplications of an Ancient Member of the DnaJ-Family Expanded the Functional Chaperone Network in the Eukaryotic Cytosol. *Molecular Biology and Evolution*, 30(5), 985–998. <https://doi.org/10.1093/molbev/mst008>
- Samadi-Maybodi, A., & Tirbandpay, R. (2021). Synthesis, optical properties and tuning size of CdSe quantum dots by variation capping agent. *Spectrochimica Acta Part A: Molecular and Biomolecular Spectroscopy*, 250, 119369. <https://doi.org/10.1016/j.saa.2020.119369>
- Sarbeng, E. B., Liu, Q., Tian, X., Yang, J., Li, H., Wong, J. L., Zhou, L., & Liu, Q. (2015). A Functional DnaK Dimer Is Essential for the Efficient Interaction with Hsp40 Heat Shock Protein. *Journal of Biological Chemistry*, 290(14), 8849–8862. <https://doi.org/10.1074/jbc.m114.596288>
- Sato, S., & (Iain) Wilson, R. J. M. (2004). The use of DsRED in single- and dual-color fluorescence labeling of mitochondrial and plastid organelles in *Plasmodium falciparum*. *Molecular and Biochemical Parasitology*, 134(1), 175–179. <https://doi.org/10.1016/j.molbiopara.2003.11.015>
- Sau, T. K., Urban, A. S., Dondapati, S. K., Fedoruk, M., Horton, M. R., Rogach, A. L., Stefani, F. D., Rädler, J. O., & Feldmann, J. (2009). Controlling loading and optical properties of gold nanoparticles on liposome membranes. *Colloids and Surfaces A: Physicochemical and Engineering Aspects*, 342(1–3), 92–96. <https://doi.org/10.1016/j.colsurfa.2009.04.014>
- Schubert, R., Herzog, S., Trenholm, S., Roska, B., & Müller, D. J. (2019). Magnetically guided virus stamping for the targeted infection of single cells or groups of cells. *Nature Protocols*, 14(11), 3205–3219. <https://doi.org/10.1038/s41596-019-0221-z>
- Sennuga, A., van Marwijk, J., Boshoff, A., & Whiteley, C. G. (2012). Enhanced activity of chaperonin GroEL in the presence of platinum nanoparticles. *Journal of Nanoparticle Research*, 14(5), 1007. <https://doi.org/10.1007/s11051-012-0824-6>
- Shamraiz, U., Raza, B., Hussain, H., Badshah, A., Green, I. R., Kiani, F. A., & Al-Harrasi, A. (2018). Gold nanotubes and nanorings: promising candidates for multidisciplinary fields. *International Materials Reviews*, 64(8), 478–512. <https://doi.org/10.1080/09506608.2018.1554991>
- Shannon, P. (2003). Cytoscape: A Software Environment for Integrated Models of Biomolecular Interaction Networks. *Genome Research*, 13(11), 2498–2504. <https://doi.org/10.1101/gr.1239303>

- Sharma, P., Tomar, A. K., & Kundu, B. (2018). Identification of functional interactome of a key cell division regulatory protein CedA of E.coli. *International Journal of Biological Macromolecules*, 106, 763–767. <https://doi.org/10.1016/j.ijbiomac.2017.08.073>
- Shonhai, A., Boshoff, A., & Blatch, G. L. (2005a). Plasmodium falciparum heat shock protein 70 is able to suppress the thermosensitivity of an *Escherichia coli* DnaK mutant strain. *Molecular Genetics and Genomics*, 274(1), 70–78. <https://doi.org/10.1007/s00438-005-1150-9>
- Shonhai, A., Botha, M., de Beer, T., Boshoff, A., & Blatch, G. (2008). Structure-Function Study of a Plasmodium falciparum Hsp70 Using Three Dimensional Modelling and in Vitro Analyses. *Protein & Peptide Letters*, 15(10), 1117–1125. <https://doi.org/10.2174/092986608786071067>
- Shonhai, A., G. Maier, A., M. Przyborski, J., & L. Blatch, G. (2011). Intracellular Protozoan Parasites of Humans: The Role of Molecular Chaperones in Development and Pathogenesis. *Protein & Peptide Letters*, 18(2), 143–157. <https://doi.org/10.2174/092986611794475002>
- Singh, P., Pandit, S., Mokkaapati, V., Garg, A., Ravikumar, V., & Mijakovic, I. (2018). Gold Nanoparticles in Diagnostics and Therapeutics for Human Cancer. *International Journal of Molecular Sciences*, 19(7), 1979. <https://doi.org/10.3390/ijms19071979>
- Sobczak-Kupiec, A., Tyliszczak, B., Krupa-Żuczek, K., Malina, D., Piątkowski, M., & Wzorek, Z. (2014). Gold Nanoparticles As A Modifying Agent of Ceramic-Polymer Composites. *Archives of Metallurgy and Materials*, 59(3), 1005–1009. <https://doi.org/10.2478/amm-2014-0168>
- Sperling, R. A., Rivera Gil, P., Zhang, F., Zanella, M., & Parak, W. J. (2008). Biological applications of gold nanoparticles. *Chemical Society Reviews*, 37(9), 1896. <https://doi.org/10.1039/b712170a>
- Stachelska, M. A. (2015). Inhibitory properties of lithium, sodium and potassium o-, m- and p-coumarates against *Escherichia coli* O157:H7. *Acta Scientiarum Polonorum Technologia Alimentaria*, 14(1), 77–84. <https://doi.org/10.17306/j.afs.2015.1.9>
- Stark, C. (2006). BioGRID: a general repository for interaction datasets. *Nucleic Acids Research*, 34(90001), D535–D539. <https://doi.org/10.1093/nar/gkj109>
- Suehr, Q. J., Chen, F., Anderson, N. M., & Keller, S. E. (2020). Effect of Ph On Survival of *Escherichia coli* O157, *Escherichia coli* O121, and *Salmonella enterica* During Desiccation and Short-term Storage. *Journal of Food Protection*, 83(2), 211–220. <https://doi.org/10.4315/0362-028x.jfp-19-195>
- Tarafdar, J. C., & Raliya, R. (2013). Rapid, Low-Cost, and Ecofriendly Approach for Iron Nanoparticle Synthesis Using *Aspergillus oryzae* TFR9. *Journal of Nanoparticles*, 2013, 1–4. <https://doi.org/10.1155/2013/141274>
- Teale, F. W. J., & Weber, G. (1957). Ultraviolet fluorescence of the aromatic amino acids. *Biochemical Journal*, 65(3), 476–482. <https://doi.org/10.1042/bj0650476>

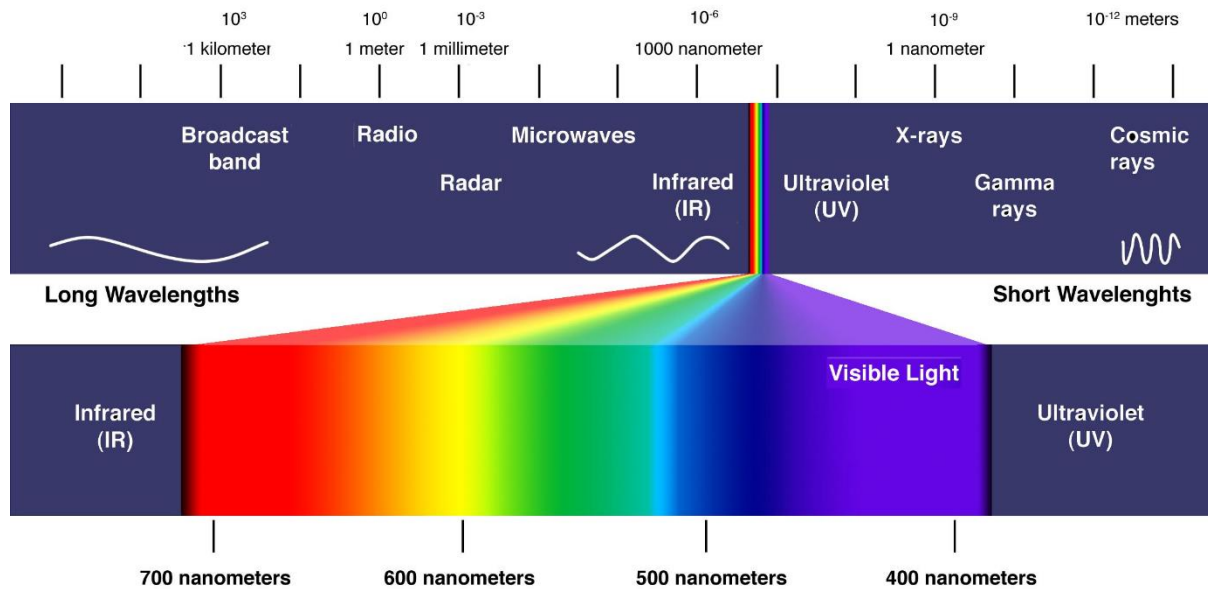
- Thomas, M., & Klivanov, A. M. (2003). Conjugation to gold nanoparticles enhances polyethylenimine's transfer of plasmid DNA into mammalian cells. *Proceedings of the National Academy of Sciences*, *100*(16), 9138–9143. <https://doi.org/10.1073/pnas.1233634100>
- Tiwari, P., Vig, K., Dennis, V., & Singh, S. (2011). Functionalized Gold Nanoparticles and Their Biomedical Applications. *Nanomaterials*, *1*(1), 31–63. <https://doi.org/10.3390/nano1010031>
- Turkevich, J., Stevenson, P. C., & Hillier, J. (1951). A study of the nucleation and growth processes in the synthesis of colloidal gold. *Discussions of the Faraday Society*, *11*, 55. <https://doi.org/10.1039/df9511100055>
- Umamaheswari, C., Lakshmanan, A., & Nagarajan, N. (2018). Green synthesis, characterization and catalytic degradation studies of gold nanoparticles against congo red and methyl orange. *Journal of Photochemistry and Photobiology B: Biology*, *178*, 33–39. <https://doi.org/10.1016/j.jphotobiol.2017.10.017>
- Vale, A. C., Pereira, P. R., Barbosa, A. M., Torrado, E., & Alves, N. M. (2019). Optimization of silver-containing bioglass nanoparticles envisaging biomedical applications. *Materials Science and Engineering: C*, *94*, 161–168. <https://doi.org/10.1016/j.msec.2018.09.027>
- van Montfort, R. L. M., Basha, E., Friedrich, K. L., Slingsby, C., & Vierling, E. (2001). Crystal structure and assembly of a eukaryotic small heat shock protein. *Nature Structural Biology*, *8*(12), 1025–1030. <https://doi.org/10.1038/nsb722>
- Wang, G., Li, Z., & Ma, N. (2017). Next-Generation DNA-Functionalized Quantum Dots as Biological Sensors. *ACS Chemical Biology*, *13*(7), 1705–1713. <https://doi.org/10.1021/acscchembio.7b00887>
- Wang, X., Sha, R., Kristiansen, M., Hernandez, C., Hao, Y., Mao, C., Canary, J. W., & Seeman, N. C. (2017a). An Organic Semiconductor Organized into 3D DNA Arrays by “Bottom-up” Rational Design. *Angewandte Chemie International Edition*, *56*(23), 6445–6448. <https://doi.org/10.1002/anie.201700462>
- Wang, X., Sha, R., Kristiansen, M., Hernandez, C., Hao, Y., Mao, C., Canary, J. W., & Seeman, N. C. (2017b). An Organic Semiconductor Organized into 3D DNA Arrays by “Bottom-up” Rational Design. *Angewandte Chemie International Edition*, *56*(23), 6445–6448. <https://doi.org/10.1002/anie.201700462>
- Wang, Z., Zhang, M., Lv, X., Fan, J., Zhang, J., Sun, J., & Shen, Y. (2018). GroEL/ES mediated the in vivo recovery of TRAIL inclusion bodies in *Escherichia coli*. *Scientific Reports*, *8*(1), 1038. <https://doi.org/10.1038/s41598-018-34090-7>
- Whitmore, L., & Wallace, B. A. (2004). Dichroweb, an online server for protein secondary structure analyses from circular dichroism spectroscopic data. *Nucleic Acids Research*, *32*(Web Server), W668–W673. <https://doi.org/10.1093/nar/gkh371>
- Wu, Y., Wu, M., He, G., Zhang, X., Li, W., Gao, Y., Li, Z., Wang, Z., & Zhang, C. (2012). Glyceraldehyde-3-phosphate dehydrogenase: A universal internal control for Western blots in prokaryotic and eukaryotic cells. *Analytical Biochemistry*, *423*(1), 15–22. <https://doi.org/10.1016/j.ab.2012.01.012>

- Xue, J., Wang, X., Jeong, J. H., & Yan, X. (2020). Fabrication, photoluminescence and applications of quantum dots embedded glass ceramics. *Chemical Engineering Journal*, 383, 123082. <https://doi.org/10.1016/j.cej.2019.123082>
- Yang, H., Huang, S., Dai, H., Gong, Y., Zheng, C., & Chang, Z. (2008). The mycobacterium tuberculosis small heat shock protein Hsp16.3 exposes hydrophobic surfaces at mild conditions: Conformational flexibility and molecular chaperone activity. *Protein Science*, 8(1), 174–179. <https://doi.org/10.1110/ps.8.1.174>
- Yang, R., Liu, Y., Gao, Y., Wang, Y., Blanchard, C., & Zhou, Z. (2017). Ferritin glycosylated by chitosan as a novel EGCG nano-carrier: Structure, stability, and absorption analysis. *International Journal of Biological Macromolecules*, 105, 252–261. <https://doi.org/10.1016/j.ijbiomac.2017.07.040>
- Yoshizaki, Y., Yuba, E., Sakaguchi, N., Koiwai, K., Harada, A., & Kono, K. (2017). pH-sensitive polymer-modified liposome-based immunity-inducing system: Effects of inclusion of cationic lipid and CpG-DNA. *Biomaterials*, 141, 272–283. <https://doi.org/10.1016/j.biomaterials.2017.07.001>
- Zabetakis, K., Ghann, W. E., Kumar, S., & Daniel, M.-C. (2012). Effect of high gold salt concentrations on the size and polydispersity of gold nanoparticles prepared by an extended Turkevich–Frens method. *Gold Bulletin*, 45(4), 203–211. <https://doi.org/10.1007/s13404-012-0069-2>
- Zhou, Y., Kong, Y., Kundu, S., Cirillo, J. D., & Liang, H. (2012). Antibacterial activities of gold and silver nanoparticles against *Escherichia coli* and bacillus Calmette-Guérin. *Journal of Nanobiotechnology*, 10(1), 19. <https://doi.org/10.1186/1477-3155-10-19>
- Zhuravleva, A., Clerico, E. M., & Gierasch, L. M. (2012). An Interdomain Energetic Tug-of-War Creates the Allosterically Active State in Hsp70 Molecular Chaperones. *Cell*, 151(6), 1296–1307. <https://doi.org/10.1016/j.cell.2012.11.002>
- Zininga, T., Achilonu, I., Hoppe, H., Prinsloo, E., Dirr, H. W., & Shonhai, A. (2015). Overexpression, Purification and Characterisation of the Plasmodium falciparum Hsp70-z (PfHsp70-z) Protein. *PLOS ONE*, 10(6), e0129445. <https://doi.org/10.1371/journal.pone.0129445>
- Zininga, T., Makumire, S., Gitau, G. W., Njunge, J. M., Pooe, O. J., Klimek, H., Scheurr, R., Raifer, H., Prinsloo, E., Przyborski, J. M., Hoppe, H., & Shonhai, A. (2015). Plasmodium falciparum Hop (PfHop) Interacts with the Hsp70 Chaperone in a Nucleotide-Dependent Fashion and Exhibits Ligand Selectivity. *PLOS ONE*, 10(8), e0135326. <https://doi.org/10.1371/journal.pone.0135326>
- Zzaman, S., Reddy, J. M., & Bastia, D. (2004). The DnaK-DnaJ-GrpE Chaperone System Activates Inert Wild Type π Initiator Protein of R6K into a Form Active in Replication Initiation. *Journal of Biological Chemistry*, 279(49), 50886–50894. <https://doi.org/10.1074/jbc.m407531200>

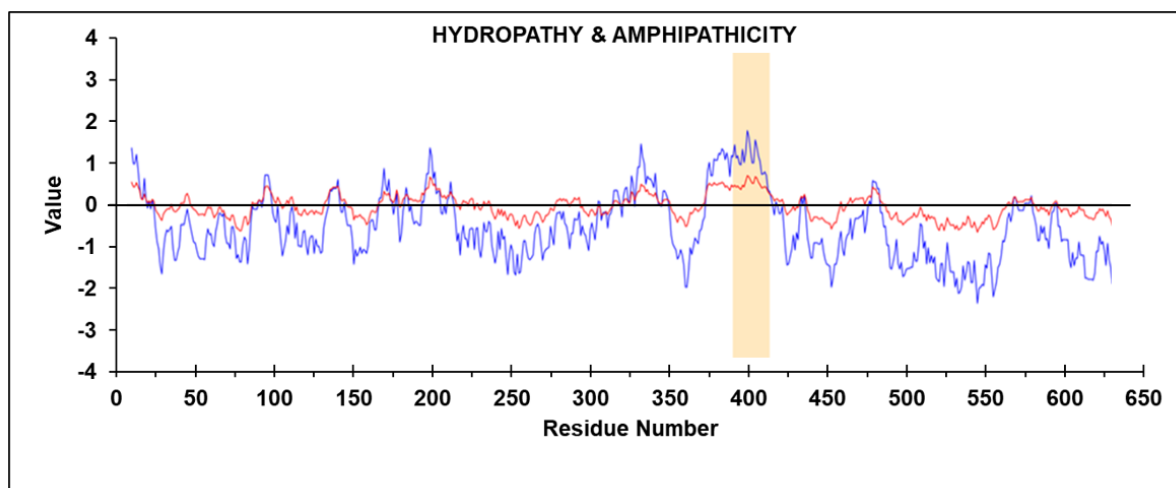
7. APPENDICES

7.1. APPENDICES A

APPENDIX A-1: The absorption spectrum indicating respective wavelength from ultraviolet, visible and infrared spectrum



Appendix A-2: Hydropathy and amphipathicity characteristic of DnaK with an indication of hydrophobic transmembrane section of the sequence



7.2. APPENDICES B

APPENDIX B-1: Preparation of aqua regia

The molar ratio between concentrated hydrochloric acid and concentrated nitric acid is HCl:HNO₃ of 3:1. HCl is about 35 %, while concentrated HNO₃ is about 65 %. The volume ratio for preparation of aqua regia is four (4) parts concentrated hydrochloric acid to one (1) part concentrated nitric acid. Care was taken to add nitric acid to hydrochloric acid and not the other way around. The resulting solution was a fuming yellow liquid smelling strongly of chlorine. Leftover of aqua regia was disposed by pouring it over a large amount of ice and neutralized with a 10 % sodium hydroxide. The neutralized solution was then safely poured down the drain. Aqua regia was kept in a cool location and used when it was fresh. Note: Aqua regia must not be stored stoppered or for an extended length of time, it becomes unstable and pressure build-up resulting in the container breaking.

7.3. APPENDICES C

APPENDIX C-1. PREPARATION AND ANALYSIS WITH SDS-PAGE

Protein samples were treated by boiling in SDS sample buffer (0.25 % Coomassie Brilliant blue [R250]; 2 % SDS; 10 % glycerol [v/v]; 100 mM Tris; 1 % β-mercaptoethanol) in a ratio of 4:1 for 10 minutes at 100 °C. The samples were analysed using SDS-PAGE by resolving through 12 % acrylamide resolving gel (Table C-1). This was done by loading the boiled samples in respective wells as well as the protein molecular marker. The electrophoresis was done at 120 volts and 100 amperes for 1 hour using the Bio-Rad Mini Protean 4 electrophoresis system (BioRad, U.S.A). The visualization was done using white light on a ChemiDoc (Bio-Rad, Germany).

Table C-1. Preparation of SDS-PAGE 12 % resolving gel and 5 % stacking gel

Running Gel	ml/Gel	Stacking Gel	ml/Gel
40 % Bis (mL)	1.5	40 % Bis (mL)	0.25
1.5 M Tris pH 8.8 (mL)	1.25	0.5 M Tris pH 6.8 (mL)	0.25
10 % APS (mL)	0.05	10 % APS (mL)	0.02
10 % SDS (mL)	0.05	10 % SDS (mL)	0.02
TEMED (mL)	0.002	TEMED (mL)	0.002
H ₂ O (mL)	2.15	H ₂ O (mL)	1.46

APPENDIX C-2. SILVER STAINING PROCEDURE

SDS-PAGE gel was washed in ultrapure water for 2 x 5 minutes and fixed in 631 fixation solvent (30 % ethanol: 10 % acetic acid in ultrapure water) for 15 minutes. After replacing the solution and fixing for another 15 minutes, the gel was washed in 10 % ethanol solution for 5 minutes twice followed by 2x washes in ultrapure water for 5 minutes each. After the gel was sensitized for exactly one minute, it was then washed with two changes of ultrapure water for a minute each. The gel was then incubated in stain working solution for 30 minutes. After two changes of ultrapure water washes for 20 seconds each, the developer working solution was added and incubated until protein bands appear. When the desired band intensity was reached, developer working solution was replaced with stop solution (5 % acetic acid) for 10 minutes before replacing with ultra-pure water and image capturing with BioRad Chemidoc ImageLab software (BioRad, USA).

APPENDIX C-3

Table C-3. Indication of respective concentrations of citrate-AuNPs used in experimental and control of the analysis of effect of citrate-AuNPs on clinical isolate *E. coli* strain.

Exp/Control	<i>E. coli</i> Strain/ Plasmid	Incubation Temperature	Treatment	Incubation Period
Control	<i>E. coli</i> O157:H7	37 °C	0 µg/ml AuNPs	5 hours
Experiment 1	<i>E. coli</i> O157:H7	37 °C	2.5 µg/ml AuNPs	5 hours
Experiment 2	<i>E. coli</i> O157:H7	37 °C	5 µg/ml AuNPs	5 hours
Experiment 3	<i>E. coli</i> O157:H7	37 °C	10 µg/ml AuNPs	5 hours
Experiment 4	<i>E. coli</i> O157:H7	37 °C	25 µg/ml AuNPs	5 hours
Experiment 5	<i>E. coli</i> O157:H7	37 °C	50 µg/ml AuNPs	5 hours

APPENDIX C-4

Confirmation and validation of vector plasmids *pQE30/dnaK* and *pQE30* were done by agarose gel electrophoresis and mapped out by snapgene™

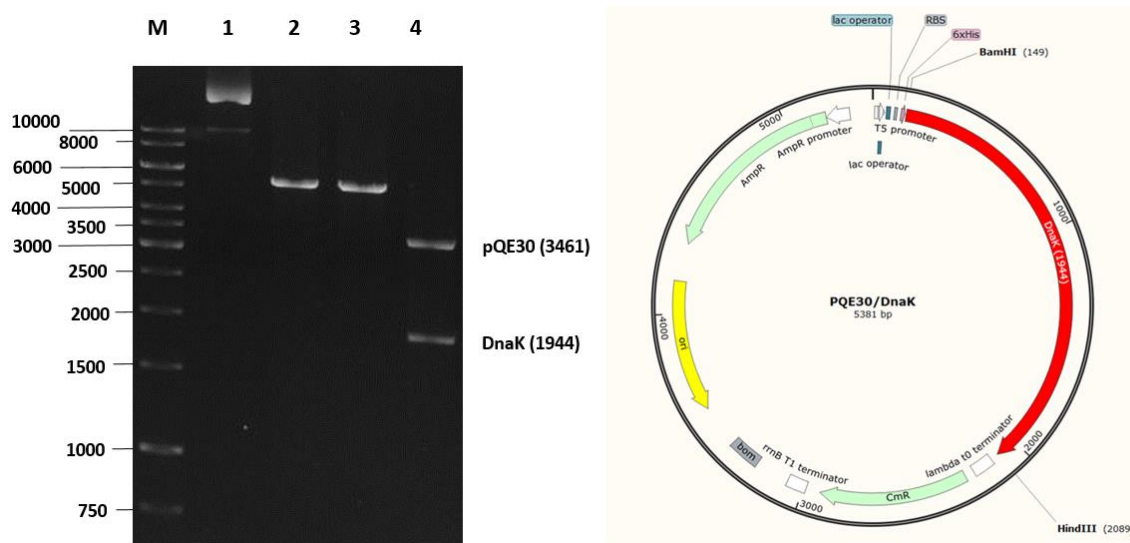


Figure C-4-1. Restriction analysis of pQE30/DnaK plasmid. (A) Agarose gel electrophoresis of pQE30/DnaK. (B) Plasmid map of pQE30/DnaK showing the *Bam*HI and *Hind*III restriction sites: Lane M, DNA molecular weight maker in bp; Lane 1 represents both linear and circular forms of undigested pQE30/DnaK plasmid; Lane 2, pQE30/DnaK digested with *Bam*HI; Lane 3, pQE30/DnaK digested with *Hind*III; Lane 4, pQE30/DnaK digested with both *Bam*HI and *Hind*III.

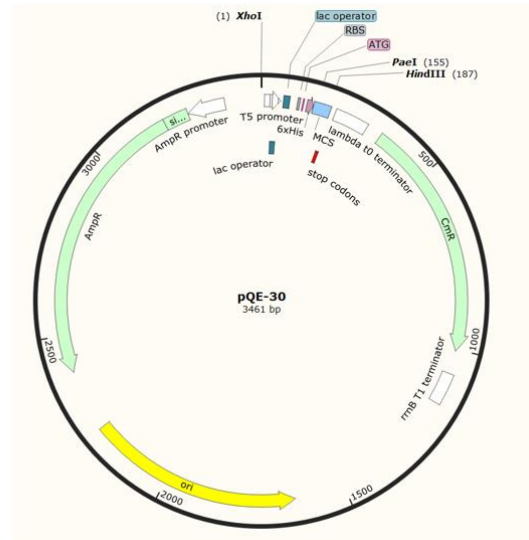
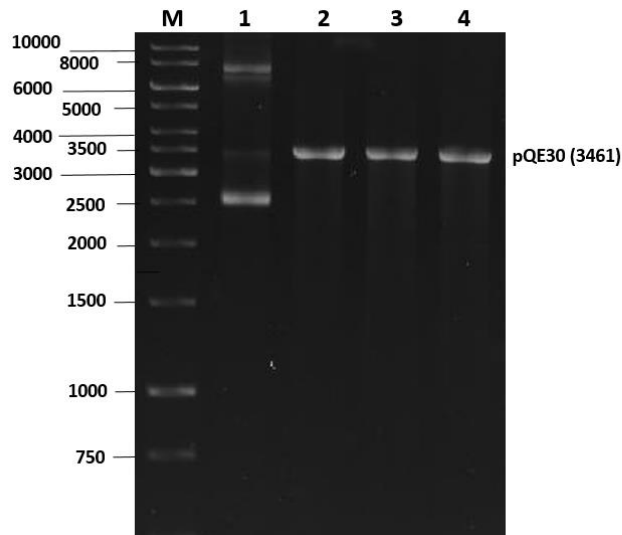


Figure C-4-2. Restriction analysis of pQE30 plasmid. (A) Agarose gel electrophoresis of pQE30. (B) Plasmid map of pQE30 showing the *XhoI*, *PaeI* and *HindIII* restriction sites: Lane M, DNA molecular weight maker in bp; Lane 1 represents both linear and circular forms of undigested pQE30 plasmid; Lane 2, pQE30 digested with *XhoI*; Lane 3, pQE30 digested with *PaeI*; Lane 4, pQE30 digested with *HindIII*.

APPENDIX C-5. REPRESENTATIVE SILVER STAINED SDS-PAGE GELS FROM BAIT AND PREY LYSATES

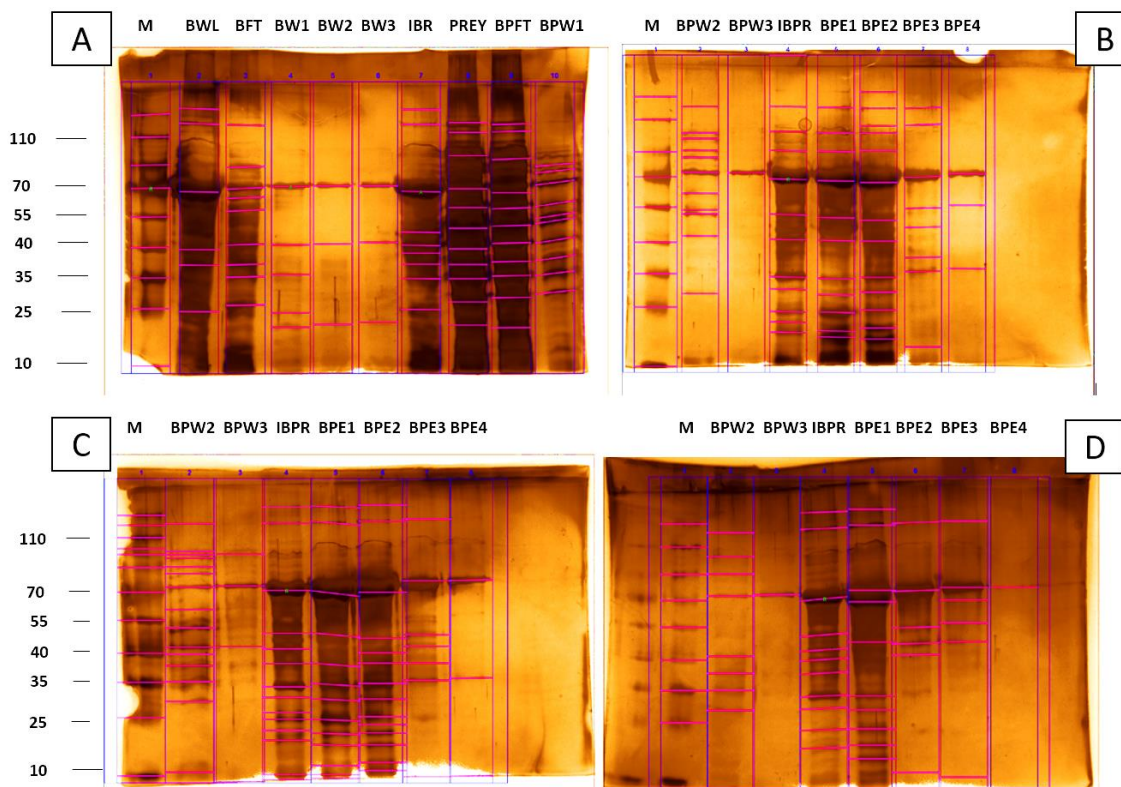


Figure C-5. Investigation of the direct interaction of recombinant DnaK and possible interaction partners in the presence of citrate-AuNPs using pull down assay. (A) A representation of the pull-down assay conducted with *E. coli* recombinant DnaK (Immobilized Bait) lysate and DnaK defective *E. coli* lysate untreated, as prey. (B) Assay was conducted with at 0 $\mu\text{g/ml}$ of citrate-AuNPs (Untreated) exposed to the prey lysate (C) Assay was conducted with at 2.5 $\mu\text{g/ml}$ of citrate-AuNPs exposed to the prey lysate (D) Assay was conducted with at 50 $\mu\text{g/ml}$ of citrate-AuNPs exposed to the prey lysate. The possible captured interactors and controls were analyzed using SDS-PAGE and subsequent silver staining. Lane M, protein marker; BWL, DnaK Bait Whole Lysate; BFT, DnaK Bait Flow Through; BW, DnaK Bait Washes; IBR, Immobilized Bait Resin; PREY, DnaK defective *E. coli* strain Lysate; BPFT, Bait with Prey Complex Flow Through; BPW, Bait with Prey Complex Washes; IBPR, Immobilized Bait with Prey Resin; BPE, Bait Prey Complex Eluent.

APPENDIX C-6. A REPRESENTATIVE DENSITOMETRIC QUANTIFICATION OF PROTEINS

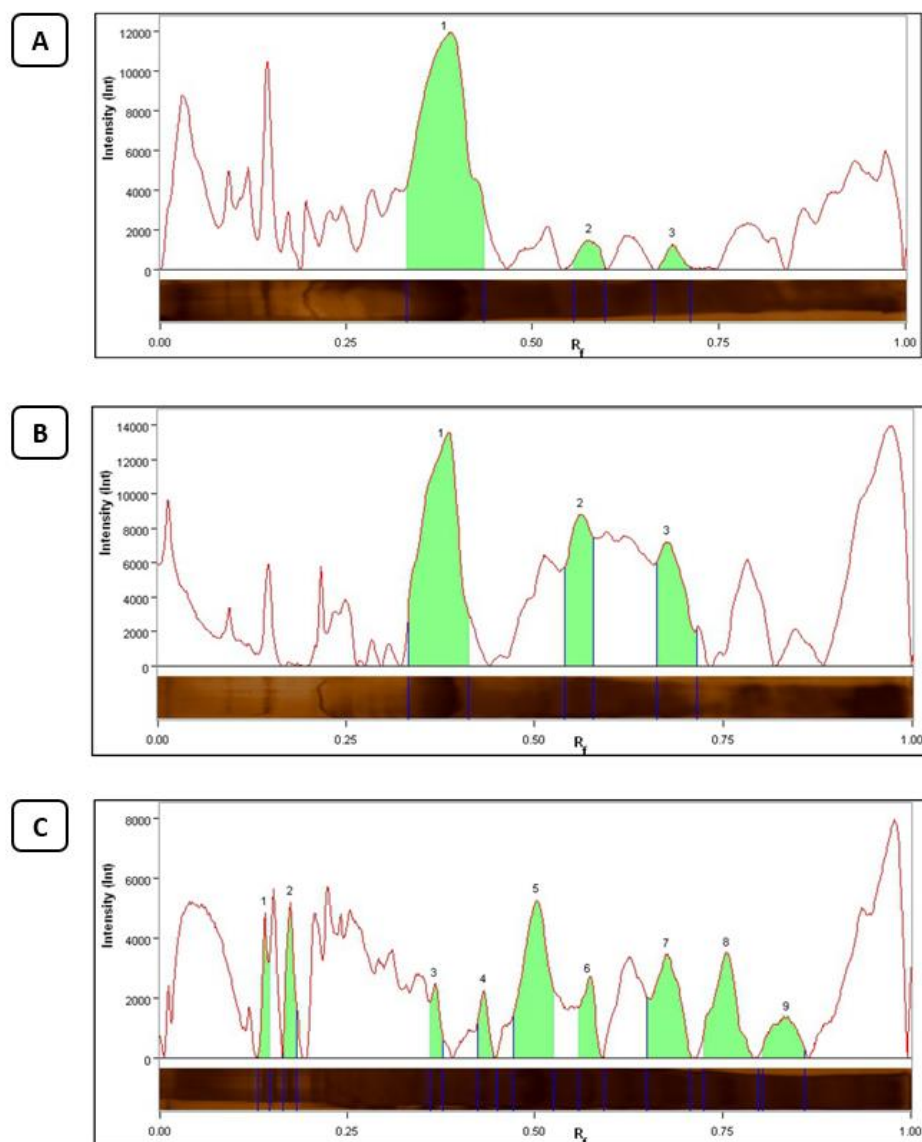


Figure C-6. A representative densitometric quantification of proteins detected by silver staining before recovery of recombinant DnaK with possible interaction partners using co-affinity assay. (A) A representative detection of recombinant DnaK bait protein lysate before immobilization of affinity resin. Band 1 between 0.25 – 0.50 R_f being of special interest (Expected recombinant DnaK) while band 2 - 3 being possible recombinant DnaK breakdowns or its endogenous interactors. **(B)** A representative detection of DnaK bait protein immobilized on affinity resin. Band 1, 2 and 3 confirms the proteins bound on resin after extensive wash procedure removing unspecifically bound proteins. **(C)** A representative detection of prey proteins from DnaK defective *E. coli* lysate. All bands considered to be possible recombinant DnaK interactors. All bands of interest will be identified by LC-MS/MS.

APPENDIX C-7. MOLECULAR CHAPERONES IDENTIFIED BY LC-MS/MS

Table C-7. Molecular chaperones identified from the co-elution fractions of lysate containing recombinant DnaK and DnaK defective *E. coli* lysates exposed to varying concentrations of citrate-AuNPs. Probability identification was done in mass spectrometry and analysed by Scaffold software.

	Protein Name	Accession Number	Mass (kDa)	Localization	Role/ Process
1	DnaK	P0A6Y9.2	69 kDa	Cytosol	Cellular response to unfolded proteins
2	GroEL	B7MSV9.1	57 kDa	Cytosol	Protein folding
3	ClpB	P63285.1	96 kDa	Cytosol/ Inner membrane	Protein refolding
4	DnaJ	B1XBE0.1	41 kDa	Cytosol/ Inner membrane	Co-factor dependent protein folding
5	SurA	Q1RGE4.1	47 kDa	Outer membrane	Outer membrane assembly

APPENDIX C-8. COMPARISON OF CO-ELUENTS OF DnaK AT DIFFERENT CONCENTRATIONS OF CITRATE-AuNPS BY LEVEL OF INTENSITY

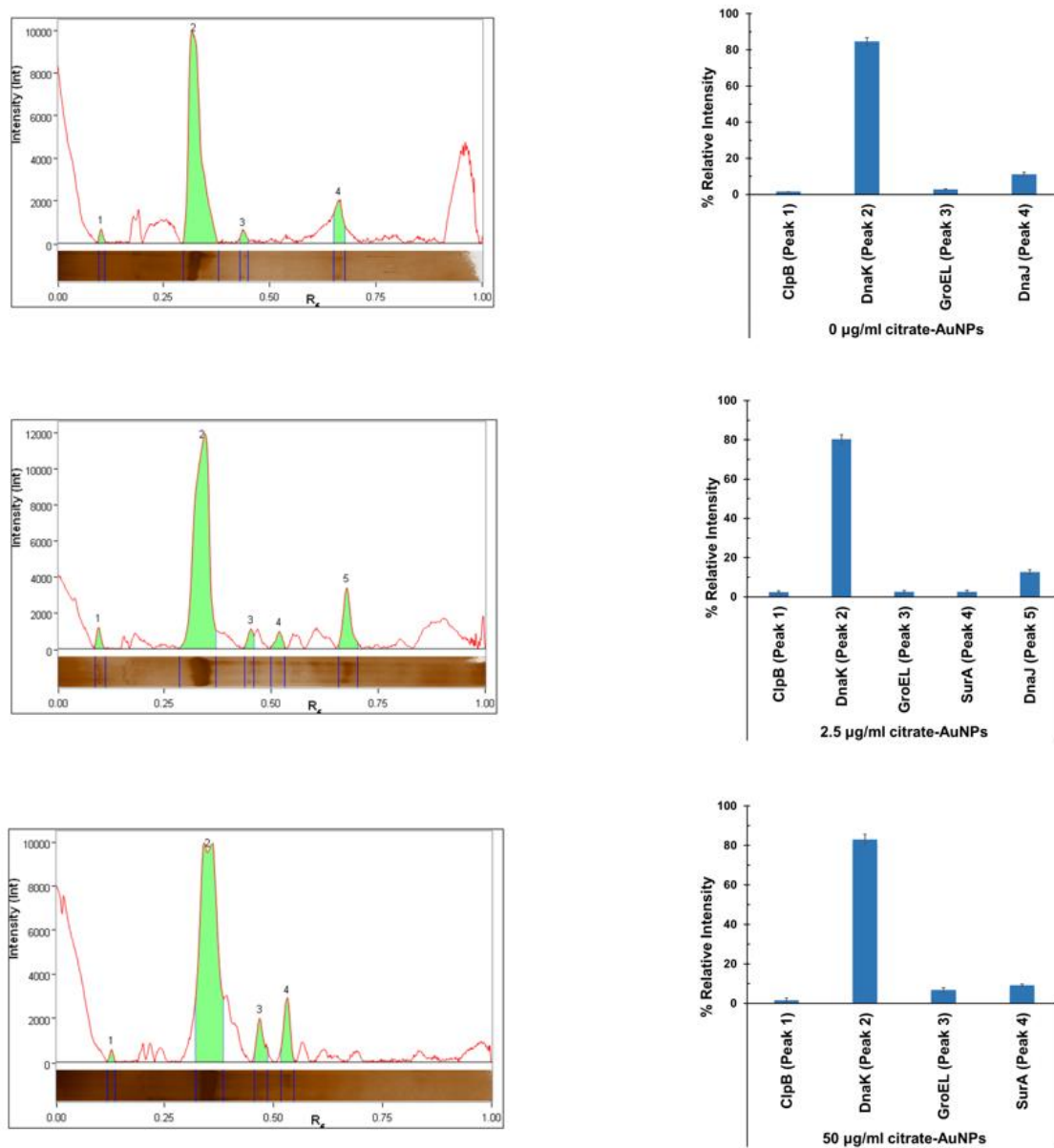


Figure C-8. Densitometric quantification of bait-prey interaction complexes recovery from co-affinity assay by ImageLab software and ChemiDoc™ imaging system. A set of prey proteins lysate was treated with varied concentration citrate-AuNPs (0 µg/ml, 2.5 µg/ml and 50 µg/ml citrate-AuNPs). Both lower order and higher order of citrate-AuNPs concentrations are observed to aid the binding of proteins herein identified only as Band 2 before identification by LC-MS/MS while only higher order of citrate-AuNPs is observed to aid the blockage of release of bait-prey interaction. All bands considered to be possible recombinant DnaK interactors are identified by LC-MS/MS.

7.4. APPENDICES D

GENERAL EXPERIMENTAL PROCEDURES

D-1. Transformation

Transformation A volume of 2 μl (equivalent to about 10 ng) of plasmid DNA was added into an aliquot of 100 μl of competent cell. The cells were then incubated on ice for 30 minutes followed by heat shock at 42 °C for 45 seconds and immediately placed on ice for 10 minutes. A volume of 900 μl of 2YT broth was added and then incubated at 37 °C for one hour with gentle agitation. The cells were transferred on 2YT plates containing the desired antibiotics followed by incubation at 37 °C overnight.

D-2. Plasmid DNA extraction

Plasmid DNA was extracted using Thermo Scientific™ Plasmid Miniprep Kit per the manufacturer's Protocol. Briefly, cells were resuspended, lysed and neutralised by adding to the pellet 250 μL resuspension solution, vortexed and followed by lysis solution and 350 μL of neutralisation solution. All solutions were added followed by inversion mixing. Supernatant was transferred into spin column and washed with 500 μL wash solution twice. With 50 μL elution solution, flow through was collected and stored as purified DNA.

D-3. Restriction digest analysis

Plasmid DNA was digested using the respective restriction enzymes (*BamHI* and *KpnI* for LS mutants, and *BamHI* and *HindIII* for wild type versions) following the method described below. The reagents were set up as follows: Sterile deionized water (16 μl), 10x restriction buffer (2 μl) and DNA (100-200 ng) 2 μl . The reaction was initiated by addition of two units (2 μl) of restriction enzymes. The restriction was allowed to proceed for 2-3 hours at 37 °C. The reaction was stopped by addition of 4 μl of 10x DNA loading buffer (0.25 % bromophenol blue and 30 % glycerol). The product was then analyzed by agarose gel electrophoresis.

D-4. Agarose gel electrophoresis

To prepare 0.8 % (w/v) agarose gel, the required amount of agarose was completely dissolved in 1x TAE buffer (40 mM, 20 mM acetic acid and 1 mM EDTA) by heating with frequent agitation. The agarose was then cooled to 55 °C prior to addition of ethidium bromide (0.5 µg/ml). The agarose gel was allowed to polymerize for 15-30 minutes at room temperature. The gel was placed in the electrophoresis chamber and covered with 1x TAE buffer. A volume of 4 µl of 10x DNA loading buffer (0.25% bromophenol blue + 30% glycerol) was added to 20 µl of the sample followed by loading of the samples into the wells. Electrophoresis was conducted at 100 volts for one hour. The gel was then visualized Chemidoc Imaging System (BioRad, Germany).

D-5. Western blot analysis

The Whatman filter paper setup and nitrocellulose were immersed in the buffer and left to equilibrate at 8 °C for 15 minutes. The transfer of the protein on the nitrocellulose membrane was performed by running at 100 volts for one hour. The membrane was removed from the sandwich and rinsed using transfer buffer. The blot was stained with Ponceau stain to determine the success of the transfer followed by visualizing the band using chemiluminescence. The membrane was blocked in 5 % non-fat milk in TBS for one hour on a rotary shaker set at 1 rpm. The membrane was washed three times in TBS-Tween for 10 minutes followed by incubation of the membrane with primary antibody for one hour. Unbound primary antibody was removed by washing of the membrane three times using TBS-Tween for 10 minutes each wash. The membrane was incubated with secondary antibody for one hour followed by washing of the membrane three times using TBS-Tween.

D-6. Chemiluminescent detection protocol

The Thermo Scientific Pierce ECL Western Blotting Substrate is a highly sensitive non-radioactive, enhanced luminol-based chemiluminescent substrate for the detection of horseradish peroxidase (HRP) on immunoblots.

Blot was removed from the transfer apparatus and blocked for 60 minutes at room temperature (RT) with shaking. Blocking Reagent was removed and primary antibody was added to working dilution before incubation for for 1 hour at RT with shaking.

Membrane was washed before incubation with HRP-conjugate working dilution for one hour at RT with shaking. Step was repeated to remove unbound HRP-conjugate. Substrate working solution was prepared and incubated with working solution for 1 minute. It was then blotted off bubbles in membrane protector before visualisation in Biorad Chemidoc.

D-7. Qubit protein quantification instructions

Qubit[®] working solution is prepared by diluting the Qubit[®] Protein Reagent 1:200 in Qubit[®] Protein Buffer. A clean plastic tube is used each time Qubit working solution (QWS) is prepared. A volume of 190 μ L of QWS was added to each of the tubes used for standards before adding 10 μ L of each Qubit[®] standard to the appropriate tube and mixing by vortex for 2–3 seconds while being careful not to create bubbles. QWS was added to individual assay tubes so that the final volume in each tube after adding sample was 200 μ L. Each sample was added to the assay tubes containing the correct volume of QWS, then mixed by vortex for 2 – 3 seconds. The final volume in each tube was 200 μ L. All tubes were allowed to incubate at room temperature for 15 minutes before pressing “Analyse”.

D-8. List of protein purification buffers

The buffers used for protein purification are listed hereunder.

Equilibration or lysis buffer: 10 mM Tris-HCl, pH 7.5, 300 mM NaCl, 10 mM Imidazole, 1X Sigmafast Protease Inhibitor, 1 mM 2- β -mercaptoethanol and 1 mg/ml lysozyme

Wash buffer I: A modification of equilibration buffer by supplementing imidazole to a final concentration of 20 mM.

Wash buffer II: A modification of equilibration buffer by supplementing imidazole to a final concentration of 50 mM.

Elution I: A modification of equilibration buffer by supplementing imidazole to a final concentration of 250 mM.

Elution II: A modification of equilibration buffer by supplementing imidazole to a final concentration of 500 Mm

D-9. Determination of CD molar residue ellipticity

The analysis of the CD spectrum is conducted by conversion of ellipticity units from the CD spectrometer to molar residue ellipticity. This was achieved using the formula below.

$$[\theta] = (100 \times \theta) / CMR \times l \dots \dots \dots \text{equation 3}$$

Where $[\theta]$ is molar residue ellipticity ($\text{deg.cm}^2.\text{dmol}^{-1}$), 100 is a constant converting path length in meters, θ is ellipticity (mdeg), l is cuvette path length, CMR being mean residue concentration ($\text{CMR} = c \times N$, eq. 4). Further, where c is Protein concentration (mol) and N is number of amino acids on the protein.

D-10. Confirmation of plasmid constructs by restriction digestion

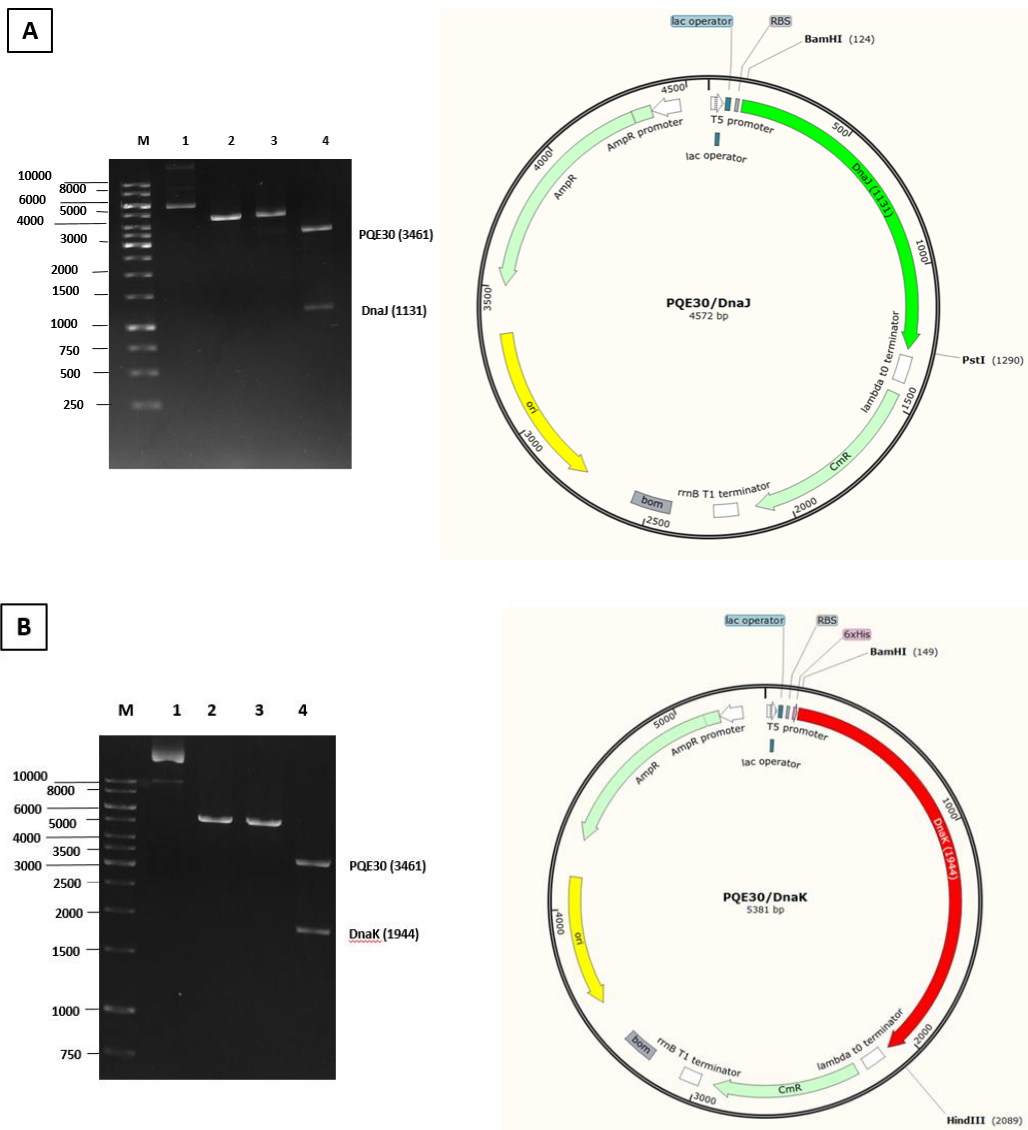


Figure D-10. Restriction digestion of pQE30/DnaK and pQE30/DnaJ. (A) pQE30/DnaJ plasmid map and restriction agarose gel showing the BamHI and PstI restriction sites. lane M, DNA molecular weight maker in bp; lane 1, undigested construct; lane 2, pQE30/DnaJ digested with BamHI; lane 3, pQE30/DnaJ digested with PstI; lane 4, pQE30/DnaK digested with both BamHI and PstI (B) pQE30/DnaK plasmid map and restriction agarose gel showing the BamHI and HindIII restriction sites. lane M, DNA molecular weight maker in bp; lane 1, undigested construct; lane 2, pQE30/DnaK digested with BamHI; lane 3, pQE30/DnaK digested with HindIII; lane 4, pQE30/DnaK digested with both BamHI and HindIII.

D-11. Protein over- expression and purification

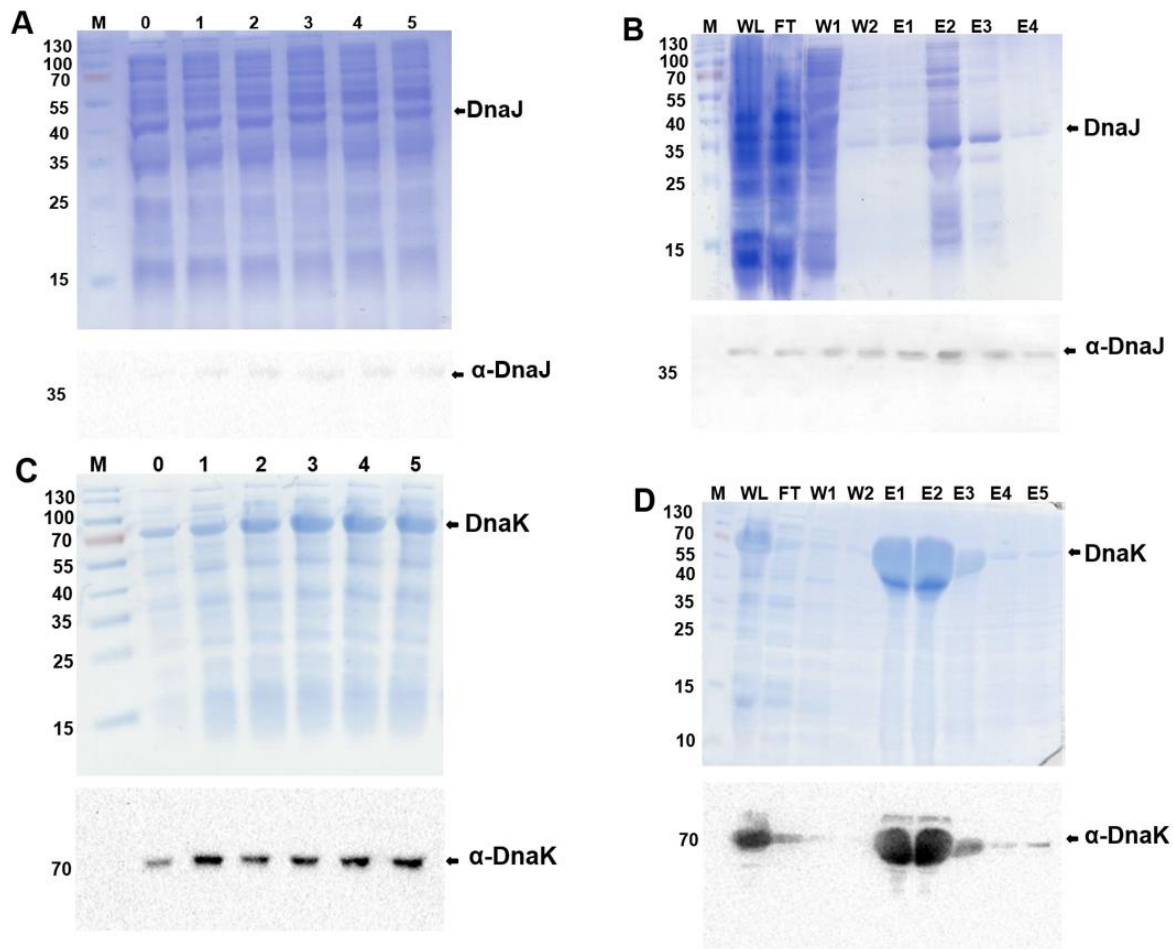


Figure D-11. Expression and purification of DnaK and DnaJ confirm the correct molecular chaperones. DnaK and DnaJ were expressed in *E. coli* XL1 Blue cells transformed with *pQE30/dnaK* and *pQE30/dnaJ*, respectively as shown in panels (A) and (C). M, Molecular weight marker (kDa), 0 – 5, hourly expression samples collected at pre-incubation and after IPTG induction. Panels (B) – (D) shows purification of DnaJ and DnaK respectively. WL, Supernatant Whole Lysate; FT, Flow through; W, Washes; E, Elutions. Lower panels represent the respective immunoblots generated using α -DnaJ and α -DnaK antibodies.

D-12. Protein (DnaK) expression and purification

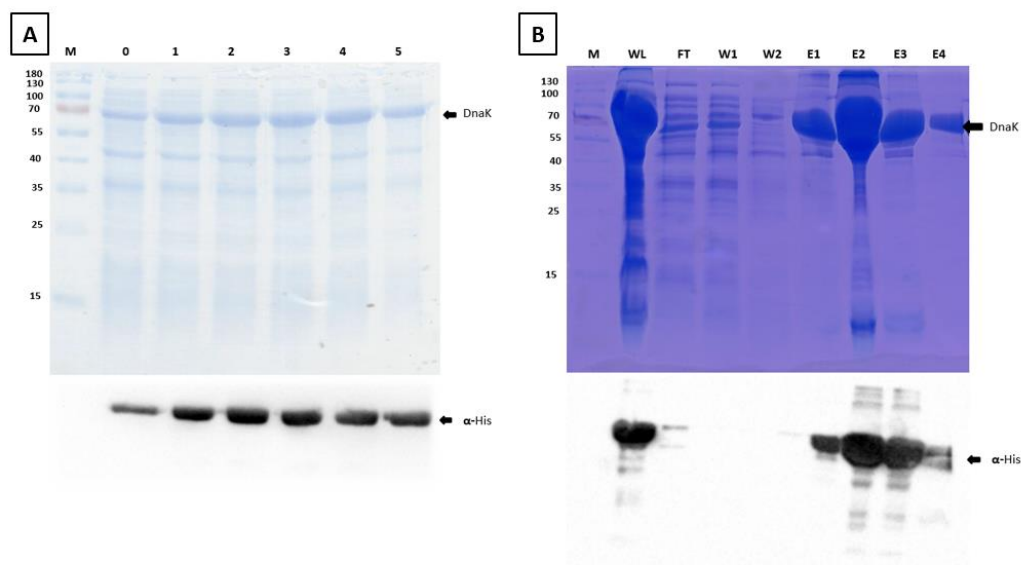


Figure D-12. Expression and purification of DnaK. DnaK was expressed in *E. coli* XL1 Blue cells transformed with pQE30/DnaK (A) SDS-PAGE analysis for the expression of DnaK where M, Molecular weight marker (kDa), 0 – 5, hourly expression samples collected at pre-incubation and after IPTG induction. Panel (B) Purification of DnaK. WL, Supernatant Whole Lysate; FT, Flow-through; W, Washes; E, Elutions. Immunoblots were generated using HRP- α -His antibody.

D-13. Effect of assay buffer composition on nanoparticles

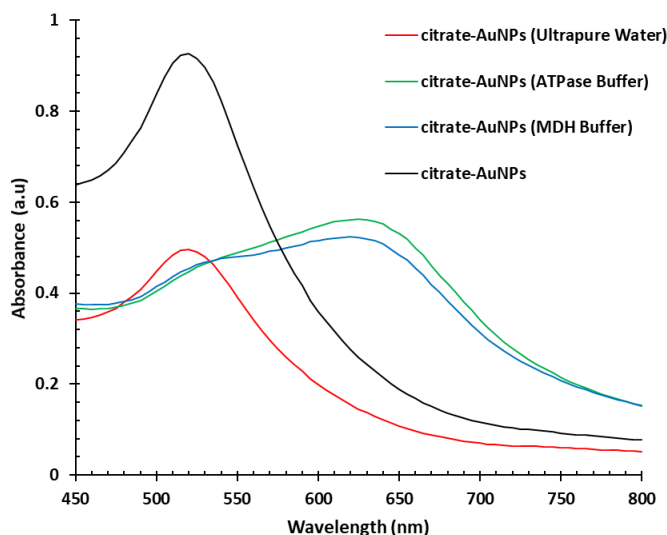


Figure D-13. Chemical composition of biochemical assay buffers was tested to determine the effect on citrate-AuNPs. Both ATPase and MDH assay buffers lowered the absorbance intensity and had a broadening effect on the nanoparticles.

D-14. ATPase activity of recombinant DnaK is aided by its co-chaperone DnaJ *in vitro*

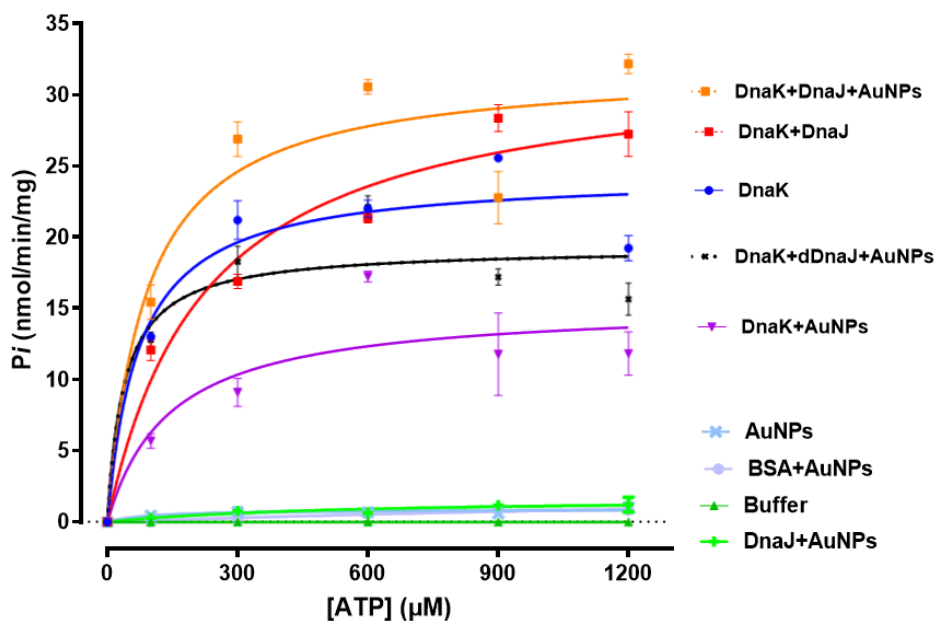


Figure D-14. The citrate-AuNPs regulate ATPase activity of the recombinant DnaK together with co-chaperone DnaJ.

D-15. Thermal stability of constituents of mdh aggregation suppression assay

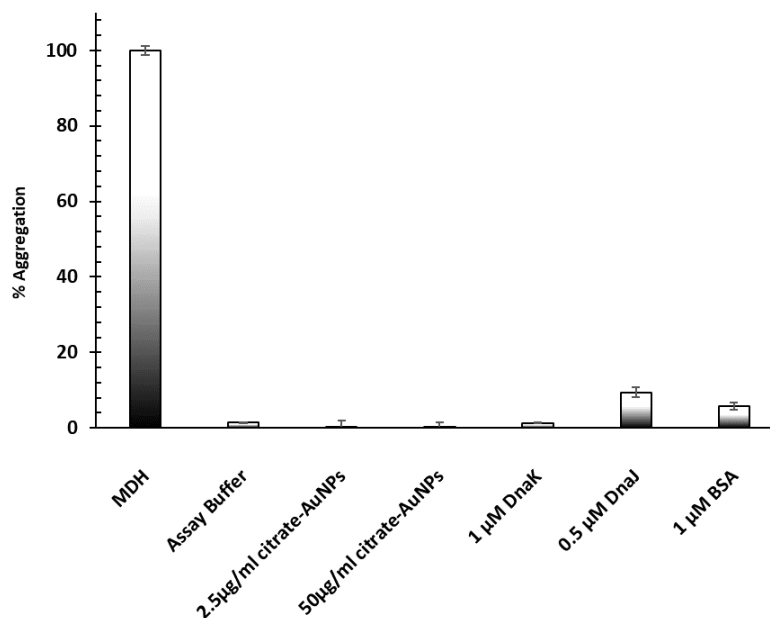


Figure D-15. Aggregation determination of components of MDH aggregation suppression assay. MDH aggregation level in percentage was regarded as the complete aggregation and used to calculate aggregation level of all other components.

D-16. List of reagents and reagent supplier

Acetic acid	Merck, Germany
Adenosine triphosphate	Sigma, U.S.A
Ammonium molybdate	Merck, Germany
Ammonium persulphate	Merck, Germany
Ampicillin	Sigma, U.S.A
Bovine serum albumin (BSA)	Sigma, U.S.A
Chloramphenicol	Sigma, U.S.A
Coomasie brilliant blue R250	Merck, Germany
Diethiothreitol	Sigma, U.S.A
Glacial acetic acid	Merck, Germany
Glycerol	Merck, Germany
Glycine	Merck, Germany
Imidazole	Sigma, U.S.A
Isopropyl-1-thio-D-galacopyranoside	Sigma, U.S.A
Lysozyme	Merck, Germany
Magnesium chloride	Merck, Germany
Methanol	Merck, Germany
Monoclonal anti-His ₆ -HRP antibodies	Sigma, U.S.A
Ni-NTA resin	Thermo Scientific, U.S.A
Nitrocellulose membrane	Pierce, U.S.A
Protein Ladder	Thermo Scientific, U.S.A
Tryptone	Merck, Germany
Phenylmethylsufonyl fluoride	Sigma, U.S.A
Polyacrylamide	Merck, Germany
Polyethylenimine	Sigma, U.S.A
Ponceau S	Sigma, U.S.A
Restriction enzymes	Thermo Scientific, U.S.A
Sodium chloride	Merck, Germany
Sodium dodecyl sulphate	Merck, Germany
Sodium hydroxide	Merck, Germany
Tris	Merck, Germany
Tryptone	Merck, Germany
Tween 20	Merck, Germany
Urea	Melford, UK
Yeast extract powder	Merck, Germany
β-mercaptoethanol	Sigma, U.S.